DISSERTATION

PHYSICAL PROCESSES CONTROLLING THE ORGANIZATION OF SHALLOW CUMULUS AS ASSESSED USING SIMPLE CLOUD MODELS

Submitted by
Michelle K. Kanipe
Department of Atmospheric Science

In partial fulfillment of the requirements
For the Degree of Doctor of Philosophy
Colorado State University
Fort Collins, Colorado
Fall 2025

Doctoral Committee:

Advisor: Peter Jan van Leeuwen

Christine Chiu
Susan van den Heever
Iuliana Oprea

ABSTRACT

PHYSICAL PROCESSES CONTROLLING THE ORGANIZATION OF SHALLOW CUMULUS AS ASSESSED USING SIMPLE CLOUD MODELS

Shallow cumulus clouds are ubiquitous throughout the maritime trade wind region and have a large and varied radiative effect that presents a problem for modeling our future climate Seinfeld and Pandis (2016); Benner and Curry (1998); Bony and Dufresne (2005). How these cloud fields will change in response to a warming planet is not fully understood and modeling the small scales of shallow cumulus explicitly with a climate model is prohibitively expensive, making these changes one of the largest sources of uncertainty in climate models Forster et al. (2021). Further complicating this problem is the manner in which shallow cumulus are seen to frequently self-organize into distinct patterns, each with their own unique impact on the Earth's radiation budget Alinaghi et al. (2024a); Kazil et al. (2024). Understanding shallow cumulus development and organization normally requires a large-eddy simulation (LES) to track the numerous forms of moisture through their dynamical and thermodynamical changes, another method with a very large computational cost. The goal of this thesis is therefore to build a simple cloud model, based on the concept of predator-prey population dynamics and uncomplicated enough to run without the aid of a supercomputer, to simulate a series of distinct shallow cumulus patterns commonly seen in the maritime trades, and to understand what are the drivers of these patterns. Additionally, the results of the simple model are compared to LES results to gain a better understanding of what drives the largest of these patterns, the so-called flowers.

This thesis is organized as follows. Chapter 1 gives an overview of the domain of interest: the maritime trades. The structure of this region will be dissected, from the synoptic scale down to the subcloud scale, and will include an in-depth discussion on the general properties and driving

processes that form shallow cumulus. The patterns of interest in this thesis are those identified by Stevens et al: sugar, gravel, flowers, and fish Stevens et al. (2019). Chapter 1 will summarize the physical properties that define these patterns as well as review the current understanding on what drives these patterns to form. Finally, a brief history of simple cloud models will be provided to show the progression in development, from the first model from Wacker up to the simple models created in this thesis Wacker (1992).

Chapter 2 describes the initial development of a 0-dimensional, vertically averaged, nonlinear dynamical system (NDS) using prognostic equations for vertical velocity, cloud water concentration, rain water concentration, and cloud drop number concentration. This model is then coupled across a grid using a series of different methods representing the manner in which clouds interact with their neighbors: through advection of condensate, to the horizontal expansion of updraft cores, to the circulations induced by cold pools. Using different sets of parameters derived from observations and LES studies, this model is able to evolve 3 distinct patterns that bear a resemblance to sugar and gravel, while aggregating condensate in the manner of flowers but without the requisite size of the real-world cloud. Sugar in this model is found to be primarily controlled by a balance between environmental instability and the gravitational drag of water drops, with very little interaction between clouds. Gravel had a similar result, with the addition of stronger latent heating in the deeper clouds as well as a cold pool-type coupling resulting in cloud arcs consistent with their real-world structure. Flowers were defined by their strong latent heating and the advection of condensate at cloud top driving the formation of clusters, but this model is not capable of simulating the vertical circulations that grow the flowers to a proper size.

In order to resolve the flower size issue, chapter 3 develops a second simple model from the first that replaces the equation for cloud drop number concentration with one for water vapor concentration. This allows for the simulation of vertical circulations despite not having a vertical coordinate, as water vapor is advected at cloud base while cloud water is advected at cloud top. By separating these processes and adjusting the parameter settings, this new model is able to simulate flowers of a realistic size while maintaining the ability to produce both sugar and gravel. An analysis of the advection terms across both flowers and gravel shows that a mesoscale circulation is indeed present through the flower, while gravel continues to be most strongly controlled by the outward expansion of the updraft simulating the leading edge of a gust front. Additional processes to distinguish cloud patterns were necessary in this second model that were not present in the first, such as the uptake of water vapor from the ocean surface and the large-scale subsidence outside of the clouds. The effects of the distance over which grid boxes are coupled were tested and found to have negligible impacts on cloud size. Finally, chapter 3 presents a comparison between both models and observed cloud fields from MODIS data, showing that the second model is accurate enough for use in testing real world problems.

Chapter 4 then applies the second model to a study conducted by Narenpitak et al on an observed sugar-to-flowers transition from the Elucidating the Role of Clouds-Circulation Coupling in Climate (EUREC^{4}A) field campaign Narenpitak et al. (2021). The simple model was able to form flowers of a proportionate size to those observed, and testing the impact of the vertical velocity resulted in a smaller flower size when the domain-mean w was reduced by 50%, comparable to the results from a more complex LES. Sensitivity tests showed that the processes necessary to flower formation were further affected by the reduction in vertical velocity, such as the gravitational drag of liquid water or the precipitation terms causing an increase in cloud size when removed as opposed to the control run's unstable growth. Once the simple model's credibility was established in this scenario, further sensitivity testing was done to measure the importance of cloud moisture concentrations to the flower size and growth rate. Both cloud water and water vapor concentrations were found to correlate most strongly with cloud size in the mid to upper levels of the cloud. When the vertical velocity was reduced, the decreased decoupling of the cloud and surface layers led to water vapor near the surface becoming a strong predictor of cloud size, whereas in the control run the two quantities remained slightly more independent between the separate layers. By comparing changes in moisture versus circulation strength, some evidence suggested that circulation was a stronger driver than cloud water of cloud size in the control run and water vapor in the weak w run, but the variances in circulation and moisture were too high to prove conclusive.

Overall, this thesis shows that simple models are indeed capable of simulating patterns of shallow cumulus seen in the real atmosphere. By virtue of dynamically coupling the different prognostic equations of the NDS, the model illustrates the manner in which individual clouds grow, advect, combine, and separate throughout their life cycle. This advances our understanding of why these patterns form, and shows that these mesoscale circulations are possible to depict with minimal computational effort, making them a feasible pursuit in climate modeling.

ACKNOWLEDGEMENTS

I would like to thank my advisor for his guidance throughout this whole process, answering my most ridiculous questions and helping me find a way forward when nothing seemed to be working. Thank you to my committee for their support and flexibility when I needed it. To the Atmospheric Science Department and the CSU Graduate School, thank you for all of the background help and the classroom instruction that helped me make progress towards my degree. To the Air Force Institute of Technology and the US Air Force Academy Meteorology Department, thank you for your empathy and understanding with my degree requirements and for keeping the Air Force bureaucracy at bay and allowing me to focus on completing my research. Thanks to my research group for keeping me on task and being a great sounding board as I worked through my methods and results. To the denizens and honorary members of ATS West, you guys were a source of light and joy in this process and kept me grounded. Thanks to my friends both at CSU and elsewhere for helping me through the stressors of life, and especially to my sister Karen for being a sympathetic ear when I needed one and encouraging me to make it through this program. And finally thank you to my cats: Libby, Pocket, Boötes, and Miranda, for all of the emotional support when I was at my lowest and giving me a reason to keep going every day.

I acknowledge the use of imagery from the NASA Worldview application (https://worldview.earthdata.nasa.gov), part of the NASA Earth Science Data and Information System (ESDIS). I would like to thank Narenpitak et al for the use of their LES output, freely available to the public (https://csl.noaa.gov/groups/csl9/datasets/data/2021-Narenpitak-etal). I also acknowledge funding for this research from the US Air Force Institute of Technology.

The views expressed in this dissertation are those of the author and do not reflect the official policy or position of the United States Air Force, Department of Defense, or of the U.S. Government.

TABLE OF CONTENTS

LIST OF TABLES

LIST OF FIGURES

Chapter 1

Introduction

This thesis focuses on the small cumulus clouds that top the oceanic tropical boundary layer. This is the lowest layer of the atmosphere that is directly modified by the Earth's surface, extending from the ground up to on average 3 km or around the 700 mb pressure level (Stull 1988; Wood and Bretherton 2006). The boundary layer generally consists of a surface layer being directly heated by the ocean surface, a mixed layer in which atmospheric constituents such as moisture and aerosols are well-mixed by turbulent eddies, and a transition layer capped by the stable trade inversion that blocks the transport of mass into the free troposphere above it (Fitzjarrald and Garstang 1981). The mixed layer can commonly become decoupled in the trade cumulus environment, that is, the layer separates into a surface mixed layer and a decoupled layer with separate vertical circulations that reduce the mass flux between them (Wood and Bretherton 2004). Temperature decreases with height in this layer while moisture is prevalent and generally well-mixed (Narenpitak et al. 2021; Wood and Bretherton 2006). The trade winds in this layer flow from the east towards the equator in the surface branch of the Hadley cell (Wallace and Hobbs 2006). Winds during the boreal winter most commonly reverse direction with height to become westerlies in the middle of the free troposphere, referred to as backward shear, which causes shallower but more extensive clouds by virtue of weakening the circulation and lowering the boundary layer inversion (Helfer and Nuijens 2021). Shallow cumulus are most often found in the central and western regions of the ocean downstream of broad areas of stable stratocumulus. Their location is believed to be caused by the marine boundary layer deepening and warming as air advects westward over higher sea surface temperatures (Krueger et al. 1995). Trade cumulus form when updrafts become more vigorous in the warmer environment that mix dry air down from the free troposphere and dissipate the stratocumulus layer, leaving the cumulus clouds behind (Wyant et al. 1997). Precipitation is also a way to break up the stratocumulus deck, as is decoupling of the cloud from the sea surface due to boundary-layer deepening and the formation of a small internal inversion above the sea surface, trapping surface water vapor (Wood and Bretherton 2004; Feingold et al. 2010).

1.1 Shallow cumulus characteristics and life cycle

What are the characteristics of shallow cumulus clouds in the tradewind boundary layer and how do they evolve over time? Various observational studies define shallow cumulus as anywhere between 100 m and 10 km in diameter, with a thickness of tens of meters up to around 1 km (Benner and Curry 1998; Jansson et al. 2023; Chen et al. 2023). Cloud thickness can vary quite dramatically for small clouds but generally increases with cloud size, while observations show an almost asymptotic limit to cloud depth for larger sizes before they begin splitting (Benner and Curry 1998). These individual clouds are then frequently observed to self-organize, with patterns reaching up to 200 km or more in diameter (Jansson et al. 2023; Stevens et al. 2019). The cloud patterns of interest in this study will be described later in this chapter. Size distributions show that the smallest clouds occur most frequently in the atmosphere, with the number of clouds falling off with size according to a double power law (Benner and Curry 1998). Larger clouds tend to have a more broken perimeter compared to the more circular small clouds (Benner and Curry 1998). Cloud lifetimes are in the range of 10-20 minutes with a peak up to 2 hrs, although they can last longer due to merging and organizing, and the longest-lived clouds typically have the longest perimeter (Chen et al. 2023; Narenpitak et al. 2021). Individual clouds are also observed to pulse during their lifetime due to a balance between buoyancy and horizontal convergence of dry air, with pulses lasting on average around 400 s and incrementally increasing the humidity and cooling the surrounding air (Heus et al. 2009). Liquid water content (LWC) is horizontally well-mixed throughout the cloud with sharp changes in LWC at the cloud boundaries (Warner 1955). Water content increases with height, peaking near the top of the cloud before rapidly decreasing (Narenpitak et al. 2021). Studies also note that the water content of the cloud is less than what it should be via adiabatic lifting of cloudy air and condensation of the excess water vapor, implying the rapid mixing of dry environmental air within the cloud (Warner 1955). Shallow cumulus fre-

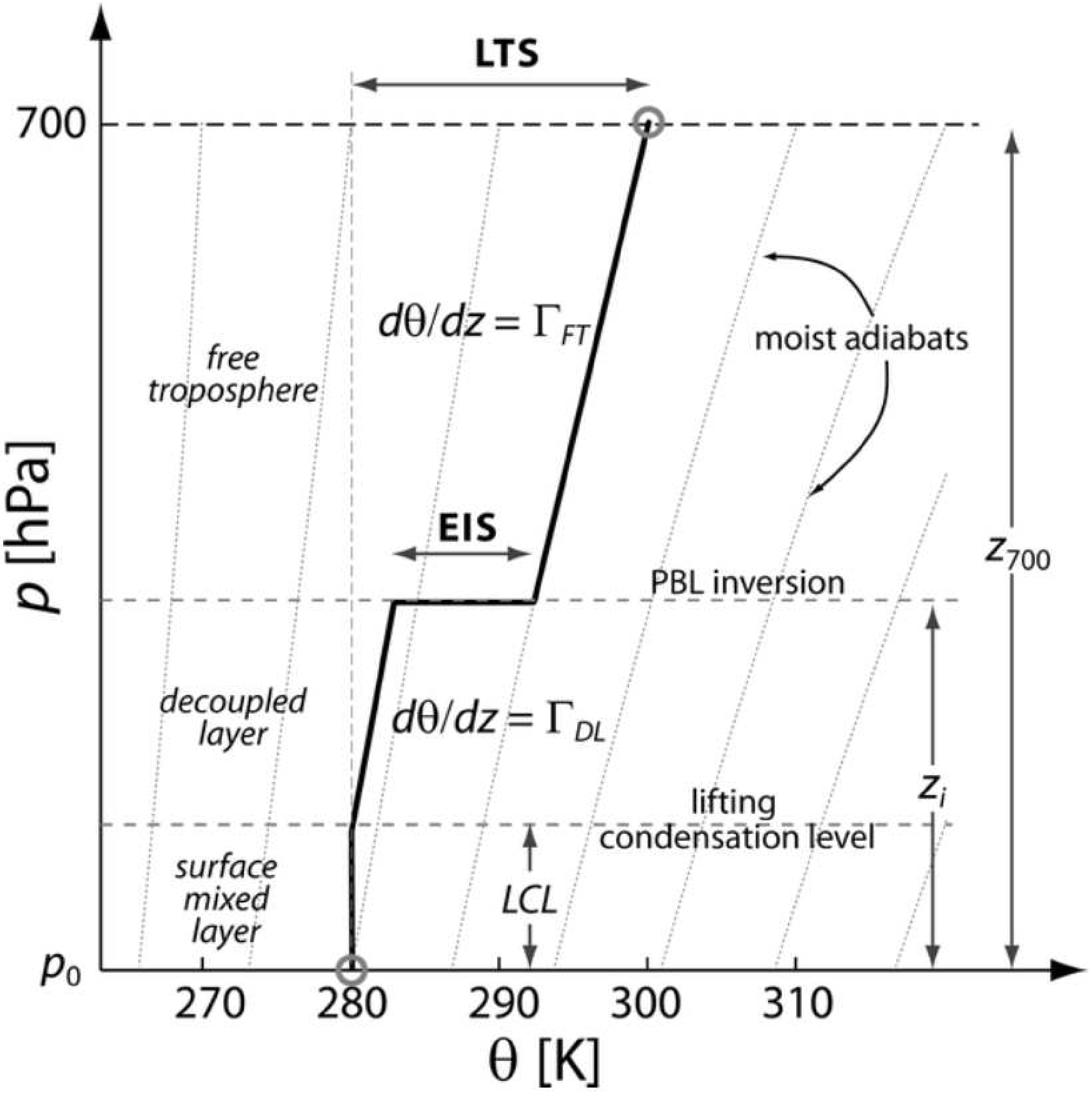

Figure 1.1: Temperature profile of the idealized boundary layer showing different sublayers. Figure rights belong to Wood et al (Wood and Bretherton 2006).

quently merge and split during their lifetime, merging most often in the middle of the cloud life cycle when their size is typically the largest, while cloud splitting occurs in the latter half of the life cycle (Chen et al. 2023).

1.1.1 Condensation

The life of a cumulus cloud can be broken down into a cycle of formation by condensation and activation of aerosols, growth via continued condensation plus collision and coalescence of droplets, and decay via sedimentation, evaporation, and mixing with dry air. The condensation rate is given by Wacker et al as:

$$\frac{dm}{dt} = 4\pi r D_1 g \frac{1}{1+H}(\rho_1 - \rho_{1,e}) \tag{1.1}$$

where r is the drop radius; D_1, g, and H are constants accounting for diffusion, ventilation, and temperature, respectively; and ρ_1 and $\rho_{1,e}$ are the partial density of water vapor for the droplet and at equilibrium, respectively (Wacker and Herbert 1998). The condensation rate is thus controlled by temperature and moisture of the drop compared to its immediate surroundings, as well as the size of the drop onto which water vapor is condensing. The dependence on moisture is straightforward, with increases in water vapor concentration resulting in faster condensation. Temperature differences are calculated from the rising of the air parcel, which cools adiabatically and decreases the saturation water vapor density, in turn increasing the condensation rate (Mason and Chien 1962). The dependence on droplet radius comes about from Kelvin's equation where the vapor pressure is much higher over a curved surface versus a flat one, making condensation onto very small, curved droplets more difficult than onto large drops with comparatively flat surfaces (Rogers and Yau 1989).

Aerosols are required for cloud droplets to form with their composition, size, and concentration all having an effect on the resulting size and number of cloud droplets. The number of aerosols activated follows the relationship of $N_d = CS^k$, where N_d is the number of aerosols activated,

S is the supersaturation, and C and k are constants relating to the distribution of aerosol sizes (Feingold et al. 1997). The Twomey effect describes the way in which aerosol concentrations affect droplet size. Increasing the number of aerosols in an environment of constant liquid water content results in water being spread out across a greater number of droplets, thus reducing the average cloud droplet size (Twomey 1959). As we discuss the parameterization of condensation in the later chapters of this thesis, these controls on the rate must all be taken into account to model a process with a solid physical basis.

1.1.2 Collision/coalescence

As cloud droplets grow from 1 micron to tens of microns, condensation becomes less of a factor in relation to the collision and coalescence of these drops as a result of gravitational, electrical, or aerodynamic forces (Rogers and Yau 1989). Collision and coalescence of droplets in cloud is generally described in three forms: self-collection, the combination of two cloud drops to form a larger cloud drop, autoconversion, the combination of two cloud drops to form a rain drop, and accretion, the combination of a cloud drop with a rain drop to form a larger rain drop (Seifert and Beheng 2001). Self-collection typically becomes an efficient mechanism for droplet growth once a sufficient number of drops grow to around 20 microns in size (Rogers and Yau 1989). The transition period from condensation to self-collection as the dominant process for droplet growth is not well-understood but is hypothesized to be the result of small-scale turbulence enhancing collisions during the condensation phase (Xue and Wang 2008; Chen et al. 2018).

The effects of gravity on collision rates are generally the most important in clouds as large droplets simply fall faster than small ones, whereas small droplets are more likely to be affected by turbulence (Rogers and Yau 1989; Xue and Wang 2008). Therefore, the differences in droplet size and velocity are the primary factors when calculating the collision kernel. A large distribution of droplet sizes is necessary for collisions to occur as a result of the differential fall speeds; the wider the distribution, the more efficient the collision rate (Xue and Wang 2008). Self-collection is one manner of droplet spectrum broadening, while turbulence is another (Seifert and Beheng

2001; Xue and Wang 2008). Interestingly, entrainment can actually increase the size distribution as well by mixing together droplets at different points in their lifetime and therefore of different sizes (Cooper et al. 2013). It should also be noted that collision does not necessarily equate to coalescence, hence why we keep referring to them in tandem, and can be jointly discussed as collection. The collection efficiency is a function of the droplet size and fall speed as a droplet falls through a field of smaller drops (Suzuki et al. 2010). As more small droplets are collected by the larger ones, the drop size distribution shifts to larger sizes and the dominant droplet growth process shifts from self-collection to autoconversion to accretion. The time it takes for autoconversion to transition into accretion governs the time for warm rain initiation, which in a cloud takes on the order of 20 minutes from condensation to collection (Rogers and Yau 1989; Xue and Wang 2008).

1.1.3 Precipitation and cold pools

While all clouds undergo condensation and collision/coalescence, not all have observable precipitation that reaches the surface. The probability of precipitation generally increases with cloud liquid water path (LWP) (Suzuki et al. 2011). Precipitation rates vary based on cloud size with rain rate increasing with cloud width and cloud fraction (Smalley and Rapp 2020; Pscheidt et al. 2019). The same relationship is not necessarily true for increasing cloud depth, although precipitating clouds are observed to be deeper than non-precipitating clouds (Liu et al. 2022; Haynes and Stephens 2007). With enhanced rain rates comes the probability of cold pools, which are ubiquitous in the wintertime trades and come with attendant impacts on the cloud of origin as well as its neighbors (Vogel et al. 2021). Cold pools, as their name suggests, lower the temperature of the air below the cloud as a result of evaporating precipitation. They are also associated with drops in humidity and increases in wind speed, pressure, and rain rate (Zuidema et al. 2012; Vogel et al. 2021). Rising motion is initiated at the edge of the cold pool as it expands horizontally, which can trigger convection more efficiently than through ambient buoyancy gradients (Hirt et al. 2020). Strong cold pools can have a myriad of impacts on their surroundings, to include deeper clouds, increased cloud cover, stronger downdrafts in cloud, stronger precipitation, and stronger updrafts at their leading edge (Zuidema et al. 2012).

1.2 Cloud patterns in the trades: sugar, gravel, flowers, and fish

Clouds in the trade wind regions have long been understood to undergo self-organization, from the open and closed cells of stratocumulus (Feingold et al. 2010), to the long cumulus cloud streets in the presence of wind shear (Kuettner 1971), to the fine arcs at the leading edges of cold pools (Vogel et al. 2021). In 2019, a group of scientists analyzed a database of 900 images spanning a period of 10 years of winters from the trade wind region east of Barbados and subjectively classified the images by their most common pattern (Stevens et al. 2019). Out of this large database four patterns stood out in their recurrence, and these patterns were colloquially termed sugar, gravel, flowers, and fish, with names based on their closest visual association. In the years since, dozens of studies have been published trying to understand their structure or their means of organization through both observational campaigns (Bony et al. 2020; Dauhut et al. 2023) or LES runs at different scales (Saffin et al. 2023; Kazil et al. 2024). Further efforts to understand their ubiquity have been pursued as well, combining crowdsourcing identification of patterns with deep learning techniques to automate the same (Rasp et al. 2020). While much insight has been gained about the formation and structure of these clouds, our understanding of this patterning is not yet complete.

1.2.1 Characteristics of the different pattern types

Sugar are defined as fine-scale, randomly distributed, non-precipitating clouds (Stevens et al. 2019). They are the smallest of the four cloud types and typically occur over less broad areas than the others with a correspondingly weaker radiative effect (Kazil et al. 2024). Using Tompkins' organizational index sugar are considered to be clustered compared to other patterns, although their shallow depth means that they are harder to distinguish on satellite imagery (Bony et al. 2020). Sugar have little to no discernible self-organization, but can be ordered into patterns such as lines or streets by the large-scale flow (Stevens et al. 2019). Vertical motions are weak and they are not associated with mesoscale circulations that typify the more organized clouds (Narenpitak et al. 2021). In the history of cloud modeling, sugar are considered to be the archetypal cloud representing tropical shallow cumulus (Stevens et al. 2019). Examples of this pattern are shown in the first row of figure 1.2.

Gravel are larger than sugar and organize into distinct lines or arcs, sometimes being compared with open cell stratocumulus. Their size is dependent upon the direction of measurement, with the arcs being upwards of 100 km long while the distance crosscutting the arc is 1-2 orders of magnitude smaller (Stevens et al. 2019). Gravel is classified around the idea of cold pools, making them heavily associated with precipitation and distinguishing them from the non-precipitating sugar (Bony et al. 2020). This is in spite of observations showing that cold pools actually occur less frequently around gravel than they do with fish and flowers, which may be a function of gravel's comparatively smaller size and thus lower moisture content (Vogel et al. 2021; Smalley and Rapp 2020). The organization of gravel is classified as regularly-spaced to random by Tompkins' metric (Bony et al. 2020). These clouds typically have strong updrafts that allow them to build to deeper heights, appearing bright on visible satellite imagery especially at the locations where gust fronts appear to converge (Vogel et al. 2021). Of the four patterns, gravel was the most frequently identified during the winter months of the study by Stevens et al and was also the most likely to dominate the field of view (Stevens et al. 2019). Examples of gravel are shown in figure 1.2 row 2.

Flowers are large irregular clusters of cloud on the order of 20-200 km in diameter that clear their immediate surroundings (Stevens et al. 2019). They are perhaps the most easily identifiable and striking of the four patterns and have received the most focus in subsequent literature into their unique dynamical structure. Flowers have been shown to be associated with shallow mesoscale circulations that aggregate moisture and deepen the boundary layer (Dauhut et al. 2023; Narenpitak et al. 2021). These circulations result in higher concentrations of moisture within the cloud and make them optically thicker, which when combined with their broad stratiform top reflect more sunlight back to space and thus have the most significant cloud radiative effect of the four (Alinaghi et al. 2024a). As the planet continues to warm, flowers are expected to be the most impacted cloud type as the shortwave cloud radiative effect weakens, making them also the largest source of uncertainty in shallow cumulus effects on climate models (Kazil et al. 2024). Flowers are often seen with precipitation and cold pools but are not reliant on them to form, with precipitation starting to fall after aggregation has already occurred (Bretherton and Wyant 1997; Narenpitak et al. 2021). That being said, the mesoscale circulation aids in ordering the internal structure of the flower by keeping the primary updraft and cold pool separated, which in turn further feeds the circulation and makes cold pools important to flower maintenance (Dauhut et al. 2023). The theorized formation process for shallow mesoscale circulations forming flowers is discussed below. Their organization index classifies them as slightly clustered owing to their larger cloud fraction over the domain, and very large flowers can sometimes be confused with closed cell stratocumulus (Bony et al. 2020). Flowers are shown in row 3 of figure 1.2.

Fish are large networks of cloud on the order of 200-2000 km that have a skeletal-like structure, often being compared to that of a fishbone (Stevens et al. 2019). They are believed to be open-cell convection organized around a gust front or other such boundary and bear a resemblance to what Garay et al termed "actinoform clouds", or convective clouds organized along a radial (Rasp et al. 2020; Garay et al. 2004). Fish are the most likely to be associated with cold pools, with these features being stronger and more long-lasting than with flowers or gravel (Vogel et al. 2021). The prominent clustering around a boundary gives these clouds a higher individual radiative effect, although fish are seen less frequently than the equally thick flowers and are thus of less importance when considering impacts on climate change (Alinaghi et al. 2024a). Their organization index is considered to be clustered at the same magnitude as sugar (Bony et al. 2020). Of the four cloud types fish have received the least amount of attention. This is possibly due to the difficultly in simulating the broader range of scales that these features span, as they are dependent on the convection scale as shallow cumulus, the mesoscale to simulate aggregating circulations, and the synoptic scale being associated with large boundaries. Fish are depicted in the bottom row of figure 1.2.

1.2.2 Pattern environments and structure

A number of studies have proposed that the four patterns of sugar, gravel, flowers, and fish preferentially form and exist in different environments. Bony et al measured the daily and interannual variability of these patterns and found that the best predictors for cloud type were the sea surface temperature (SST), the near-surface wind speed, and the estimated inversion strength (EIS), the last used as a proxy for the lower tropospheric stability (LTS) (Bony et al. 2020; Wood and Bretherton 2006). The larger flowers and fish preferred a strong inversion and a more stable layer, being deeper clouds more likely to interact with the inversion layer which forces horizontal growth. Vogel et al found a similar result in the strong correlation between decreasing inversion strength and decreasing stratiform cloudiness (Vogel et al. 2020). Meanwhile flowers and gravel, as the patterns with the strongest mesoscale circulations and regular to random organization, preferred a strong surface wind, while the highly clustered fish and sugar existed in weak winds (Bony et al. 2020). This was observed during EUREC^{4}A as clouds organized into flowers and gravel following an increase in the trade wind speeds (Savazzi et al. 2024). Bony et al also found that flowers tended to be associated with lower SSTs, although this observation may be impacted by the fact that flowers have larger and more frequent cold pools, as Narenpitak et al actually found the opposite result to be true during EUREC^{4}A when clouds advecting over warmer water transitioned from sugar to flowers (Bony et al. 2020; Narenpitak et al. 2021). The effect of cold pools may impact the correlation that Bony et al found between sugar and high SSTs as well (Bony et al. 2020). At interannual timescales the same results held true with the exception of SST, which was no longer a discriminating factor.

Self-organization of cloud fields, in particular for flowers, is heavily associated with the spontaneous formation of shallow mesoscale overturning circulations (SMOCs), which are common throughout the tradewind layer (George et al. 2023). These circulations are believed to initiate in

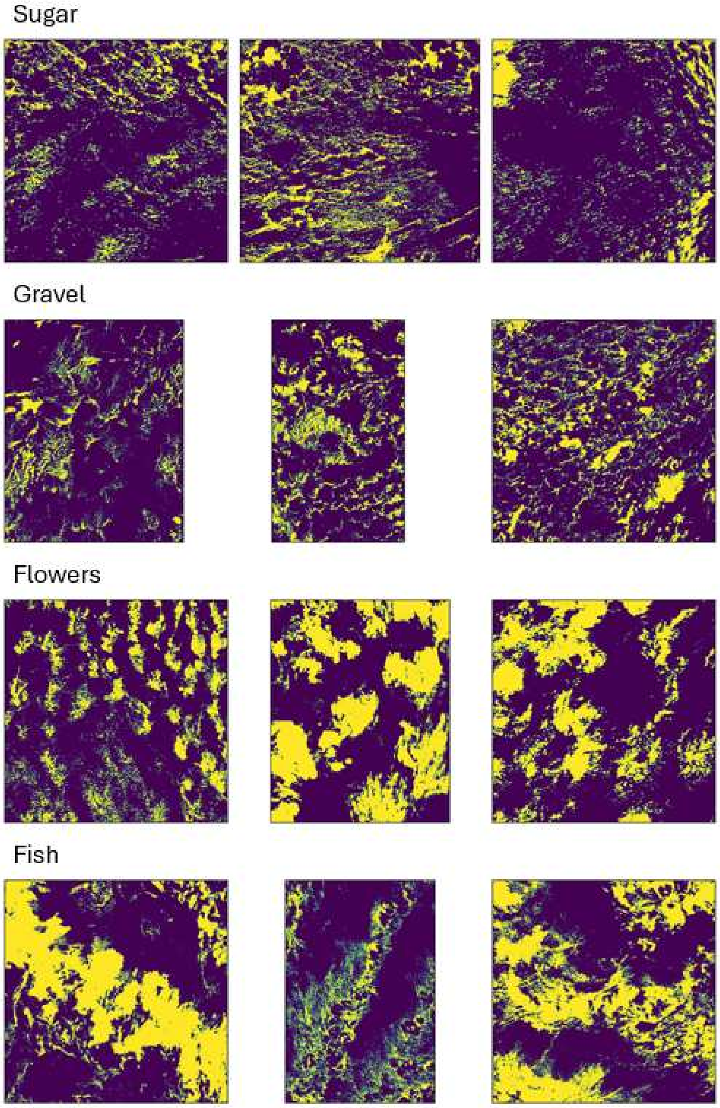

Figure 1.2: MODIS images of the four different cloud patterns classified by Stevens et al (Stevens et al. 2019). Images were taken over Jan-Mar 2017 and 2018 from the trade wind region northeast of Barbados using data from NASA Worldview (NASA 2024).

the presence of small horizontal gradients in temperature and humidity, both at the submesoscale (cloud scale) and the mesoscale (Janssens et al. 2023; Savazzi et al. 2024). LES experiments show that flowers generally develop in the location of previously-existing moist patches (Dauhut et al. 2023). The gradient induces local weak vertical motions producing small cumulus, which is enhanced by subsidence aloft converging moisture in the cloud layer (Narenpitak et al. 2021). Below the cloud the developing gradients in vertical velocity converge moisture and amplify the moisture variance, making moist areas moister and dry areas drier (George et al. 2023). As convergence below the cloud strengthens in the presence of this gross moist instability, air diverges in the cloud layer and forms the circulation (Dauhut et al. 2023; George et al. 2023). Subcloud convergence increases the moisture flux into the cloud base, reducing the drying effect of entrainment and further moistening the cloud base (Vogel et al. 2022; George et al. 2023). Cloud base mixing of moisture is also a function of the vertical velocity while entrainment varies diurnally independent of the circulation, further allowing moisture to accumulate at cloud base (Vogel and Bony 2020). The cloud continues to grow as moisture and horizontal momentum converge below cloud, while moisture is depleted in areas of subcloud divergence (George et al. 2023). Eventually the cloud grows large enough that larger-scale processes such as radiative cooling or precipitation begin to have an effect, modulating the cloud size (Janssens et al. 2023). Although large-scale vertical motions can help to deepen the cloud layer and strengthen turbulent kinetic energy (TKE) production, providing an environment more conducive to flower formation, it is the mesoscale winds that actually drive the aggregation of moisture (Narenpitak et al. 2021). Radiational cooling at cloud top does not appear to drive SMOCs as modeled flowers form even with radiation effects suppressed, and observations suggest that it actually inhibits circulations (Dauhut et al. 2023; George et al. 2023).

Cold pools have had a long history with the study of SMOCs, with early work attributing cloud aggregation to their presence (Seifert and Heus 2013), while other studies maintain that they have no influence in driving self-organization of clouds (Bretherton and Blossey 2017). Current understand is a combination of the two viewpoints in that while cold pools do not initiate aggregation, they do have an impact on the structure of the mature cloud (Smalley and Rapp 2020; Dauhut et al. 2023). Observations during EUREC^{4}A and later LES simulations captured the life cycle of a flower over a 24 hour period (Narenpitak et al. 2021; Dauhut et al. 2023). Initially precipitation was not present, only being observed after the flower had formed (Narenpitak et al. 2021). The likelihood of precipitation increases with cloud size as the environment moistens and the updraft becomes more protected from entrainment effects, and so as the cloud grew then rainfall did develop with a cold pool forming adjacent to the flower (Smalley and Rapp 2020; Narenpitak et al. 2021). The size of the cold pool increased in proportion to the size of the flower, eventually dominating the area underneath the cloud. At this point the cold pool was believed to give the flower its characteristic circular shape as updrafts supplying the flower were pushed to the leading edge of the cloud (Dauhut et al. 2023). Therefore cold pools are still believed to be influential in the structure of a flower, just not in their formation.

1.3 A history of simple cloud modeling

We now change gears here into the other focus of this project to discuss the history and evolution of simple cloud models. The fundamental idea behind cloud modeling is not complicated: at its most basic it is simply a matter of tracking sources and sinks of moisture. Inside a cloud these include thermodynamic processes such as condensation and evaporation, or dynamic processes such as advection. The degree to which these processes are then broken down and dissected controls the level of detail with which one can simulate a cloud or field of clouds. This leads to a balancing act when developing and running cloud models between the required extent of realism from which to draw robust conclusions and the computational expense of more and more complex models. While LES are powerful tools for modeling detailed cloud processes and are becoming more efficient every year, the past several decades have seen scientists also venture in the opposite direction by exploring the use of simple models that reduce clouds into their most basic mechanisms (Koren and Feingold 2011).

First we must clarify what we mean by "simple cloud model", as no formal definition has been specifically qualified by the literature on the subject. For the purposes of this research, a simple model consists of a system of ordinary differential equations that describe the evolution of a cloud at a single point. These equations describe pseudo-independent physical processes in the sense that each process can be isolated from the others. This definition distinguishes a simple model from an LES in terms of both scale and complexity, as an LES simulates cloud over a defined area as opposed to a single point and solves a set of partial differential equations that is inextricably interconnected in its driving physics.

Simple cloud models are based on the fundamental idea of the predator-prey relationship independently developed by Alfred Lotka and Vito Volterra in the early 1900s (Lotka 1925; Berryman 1992). They describe the circular relationship between two interdependent populations, whether they be foxes and rabbits, two reactive chemicals, or in our case, clouds and precipitation (Lotka 1910). The relationship is described mathematically as:

$$\begin{aligned} \frac{dN}{dt} &= aN - bNP \\ \frac{dP}{dt} &= cNP - dP \end{aligned} \tag{1.2}$$

where N is the species being preyed upon by species P (Berryman 1992). The prey species is increased through an external source while also decreasing as it is consumed by the predator species. The predators increase through this interaction until their population can no longer be sustained by the available prey, and the predator population decreases. With fewer predators reducing their size, the prey population then begins to increase and the cycle begins again. This is diagrammed in figure 1.3, showing how the predator population lags in phase with the population of prey.

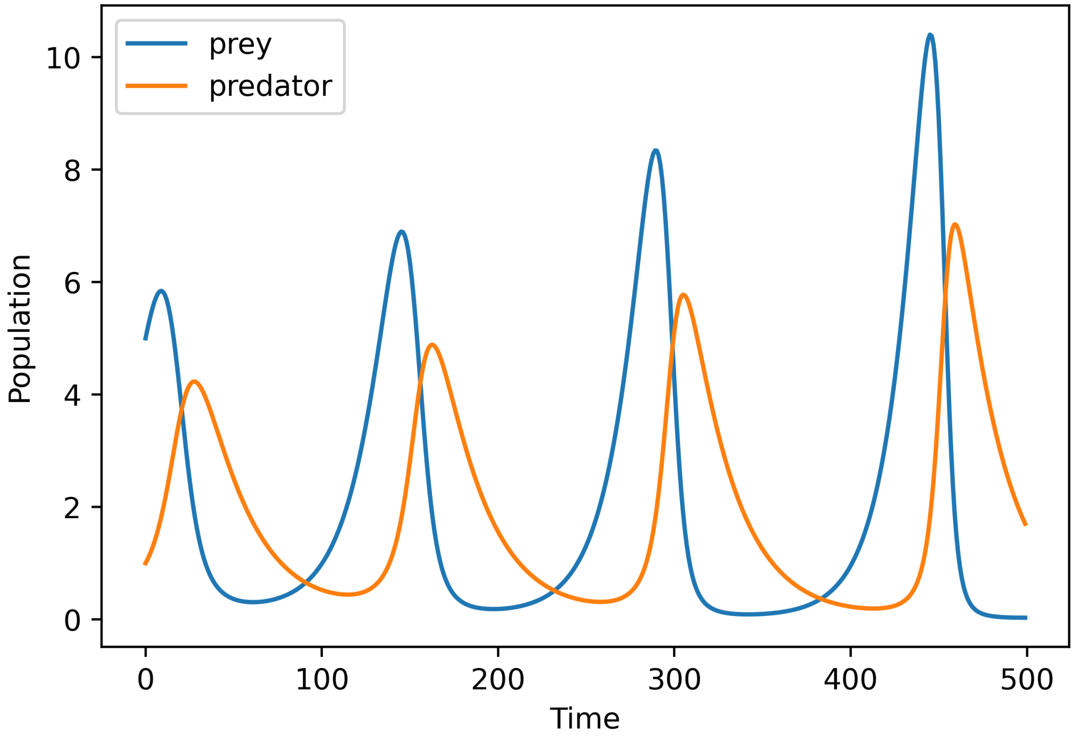

Figure 1.3: An illustration of the predator-prey relationship from equation set 1.2, with $a = 0.7$, $b = 0.4$, $c = 0.2$, and $d = 0.4$.

The Lotka-Volterra equations can be applied across multiple different aspects of the cloud system, but the central idea is the same. A cloud grows as a function of some independent source, such as condensation of water vapor. The cloud droplets are then "preyed upon" by their collision and coalescence into precipitation. The precipitation undergoes sedimentation and eventually depletes itself at a faster rate than can be formed from available cloud. As precipitation is sufficiently removed, the cloud is able grow again from available moisture (Koren and Feingold 2011). Multiple different species within a cloud system can act as prey and predator, respectively, whether that be cloud water and rain water, cloud water and ice particles, water vapor and cloud water, etc (Spassova and Nikolov 2005; Pujol and Jensen 2019). Additionally, a cloud can have more than one predator acting on an individual prey species, such as with multiple different forms of precipitation particle (e.g. rain, ice, graupel, hail, etc.) (Wacker 1995).

The goal of using a simple model is to understand the self-organization of a cloud or cloud system using only the basic processes, removing the computational complexity of an LES while allowing one to assess the individual contributions from each cloud process. Here we look at five such models based on the predator-prey relationship as they are applied to different problems of cloud structure and organization, which will later form the basis for our own model development when assessing the idea of specific cloud pattern formation.

1.3.1 Wacker model

The first explicit application of the Lotka-Volterra equations to a cloud system was by Ulrike Wacker in 1992 and 1995, with the goal of understanding the self-organizing behavior of cloud life cycles (Wacker 1992). The first study focused on the basic cloud-warm rain system (i.e. clouds $>$ 0°C with no ice particles), while the second expanded the work to include multiple precipitation types. The parameterization of the system remained close to that of the original work from Lotka and Volterra, with only 1-2 sources of each particle species and one sink each. In equation 1.3, these include the external source rate Φ, the accretion or riming rate $b_i C P_i^{\beta_i}$, and the sedimentation flux $d_i P_i^{\delta_i} - S_i$, where C and P are the mixing ratios of cloud water and precipitation particles, respectively (Wacker 1995). The subscript i represents individual precipitation species, with the coefficients and exponents being specific to each type as a function of particle mass, diameter, and fall speed.

$$\begin{aligned}\frac{dC}{dt} &= \Phi_c - \sum_{i=1}^{N} b_i C P_i^{\beta_i} \\ \frac{dP}{dt} &= \Phi_i + b_i C P_i^{\beta_i} - (d_i P_i^{\delta_i} - S_i) \end{aligned} \tag{1.3}$$

By varying the different control parameters in accordance with observations from Kessler et al and Locatelli et al, the model was able to identify steady states, limit cycles, and the selection of different precipitation types in each given regime (Kessler 1969; Locatelli and Hobbs 1974). Wacker describes three of these regimes as a function of the rate of change of accretion/riming as compared to sedimentation. In the case of equal rates of change, each steady state is found to select a single precipitation type, decaying all others. When sedimentation rate exceeds accretion/riming, as is the case with spherical particles, multiple precipitation types can exist with at least one in steady state. If an external precipitation source is present, the model will preferentially select that precipitation type. Finally when accretion/riming rate exceeds sedimentation, valid for flat ice particles, then oscillations of different precipitation types occur. If any precipitation particle falls below a critical threshold, then that particle type is suppressed.

Ultimately this work was able show how both warm and mixed phase clouds evolve over time in different regimes, either selecting a single precipitation type or allowing multiple particles to vary and exist in harmony. It also highlighted the criticality of the dynamic structure of the system and of the parameter settings: changes in accretion/riming and sedimentation rates resulted in very different cloud states. Of most importance, however, was that Wacker proved that simple models are a valid tool for studying the development of clouds in different regimes, with these results aligning with those from observations and numerical models in spite of the simple model limitations in depicting "realistic" clouds (Wacker 1995).

1.3.2 Spassova and Nikolov model

From the work of Wacker, Spassova and Nikolov expanded her model into a nonlinear dynamical system describing the dynamic and thermodynamic properties of the 1-dimensional column (Wacker 1992; Spassova and Nikolov 2005). In addition to the cloud and rain water, this model also included equations for the vertical velocity w, water vapor mixing ratio Q_v, and cloud temperature T_c in equation 1.4. The addition of a third or more equation is necessary for producing chaotic solutions, one of the goals of this study (Lorenz 1963). The w equation is adapted from the equation of convective motion, Q_v is another type of predator-prey relationship, and T_c comes from the first law of thermodynamics. Here we start to see the expansion of the simple sources and sinks of Lotka-Volterra and Wacker into processes with more direct applicability to real-world clouds (Lotka 1910; Wacker 1995). These include the autoconversion b_1Q_c, representing the combination of two cloud drops to form a rain drop, and accretion $b_2Q_cQ_p$, representing the combination of a cloud drop and rain drop. The constant source Ψ becomes analogous to the rate of nucleation or condensation, while sedimentation is a flux of precipitation through the layer.

$$
\begin{aligned}
\frac{\partial Q_c}{\partial t} &= -w\frac{\partial Q_c}{\partial z} - b_1Q_c - b_2Q_cQ_p + \Psi_c \\
\frac{\partial Q_p}{\partial t} &= -w\frac{\partial Q_p}{\partial z} + b_1Q_c + b_2Q_cQ_p + P - b_3Q_p \\
\frac{\partial w}{\partial t} &= -w\frac{\partial w}{\partial z} - g(Q_c + Q_p) + F_w \\
\frac{\partial Q_v}{\partial t} &= -w\frac{\partial Q_v}{\partial z} + K_v\frac{\partial^2 Q_v}{\partial z^2} + F_v \\
\frac{\partial T_c}{\partial t} &= -w\frac{\partial T_c}{\partial z} + K_T\frac{\partial^2 T_c}{\partial z^2} - \gamma_a w - \frac{L}{c_p}F_v
\end{aligned}
\tag{1.4}
$$

Like the Wacker model, the Spassova and Nikolov model is able to produce steady state and regular oscillatory behavior as a function of the parameter settings taken from the former (Wacker

1992; Spassova and Nikolov 2005). The controlling parameter in this model represents the condensation rate; variations in this parameter was the only means of significantly changing the character of the solutions. Chaotic behavior was also possible with at least the inclusion of the vertical velocity. The critical parameters in the chaotic regime included the condensation rate as well as buoyancy f_w, autoconversion $b_1 Q_c$, and precipitation influx at cloud top P. While the former two processes are expected to have a significant impact, as we will show later in this work, the latter two were surprising in their level of importance as the precipitation influx is quite small and the autoconversion is not a factor compared to accretion. However the authors note that the chaotic regime pushed the boundaries of realism in terms of the parameter settings, so this result is more of a thought experiment than one from which to draw real-world conclusions.

The value in the work of Spassova and Nikolov comes from the continued development of parameterizing these simple cloud models (Spassova and Nikolov 2005). With this model, we have the first instance of expanding the predator-prey relationships into multiple physical sources and sinks, showing that individual cloud processes can be modeled separately within the framework of the Lotka-Volterra equations and still produce stable, regular, and chaotic results. In addition, the inclusion of vertical velocity tendency was a critical step into broadening the applicability of such simple models, providing a means for clouds to have a dynamical impact on their surroundings and paving the way for future coupling efforts.

1.3.3 Koren and Feingold model

Koren and Feingold published the next simple model of note in order to simulate different output regimes as a result of self-organization (Koren and Feingold 2011). The model uses cloud depth H as a proxy for cloud water and relates this variable to an algebraic equation for rain rate R. The authors introduce changes in the aerosol concentration N_d as a modulating factor between H and R, as clouds cannot exist without the presence of aerosol (Rogers and Yau 1989). H and N_d are modeled as a combination of what is termed "dynamical forcing", i.e. impacts from processes such as instability or entrainment, that result in an asymptotic approach of H and N_d to their environmental carrying capacity, and a loss term as a result of rainfall (Koren and Feingold 2011). The equations also include a delay time τ to account for the fact that transitions between cloud states do not occur instantaneously, which is a common feature of mathematical depictions of population dynamics (Anshu and Dubey 2023).

$$\begin{aligned} \frac{dH}{dt} &= \frac{H_0 - H}{\tau_1} - \frac{\alpha H^2}{c_1 N_d} \\ \frac{dN_d}{dt} &= \frac{N_0 - N_d}{\tau_2} - c_2 N_d R \\ R &= \alpha H^3 N_d^{-1} \end{aligned} \tag{1.5}$$

This model gives solutions of the same four characteristics as Spassova and Nikolov, namely steady state, regular oscillations, chaotic behavior, and unstable growth (Spassova and Nikolov 2005). In the steady state case, the cloud depth is controlled primarily by the dynamical forcing at large N_d, with N_d becoming more of a controlling factor as it itself decreases. Weak precipitation causes the time-dependent oscillations in cloud depth to be dampened back towards a steady state, smoothing out any perturbations, while higher rainfall rates are more likely to reach a regular oscillation. The time-varying values of cloud depth and rain rate exhibit a pronounced correlation over time as the rain rate lags the cloud depth, indicating that it takes time for the cloud to move through its life cycle and produce precipitation.

Koren and Feingold later expanded on this study to introduce coupling of the model across a grid to investigate whether clouds would self-organize and synchronize (Feingold and Koren 2013). Coupling is done via changes in the cloud depth, which equate to changes in the vertical velocity and therefore the circulation strength. Clouds that initially oscillated in sync with each other eventually grew to be out of phase with their neighbors, indicating a growing cloud interfering with those next to it. This was the case for both a one-dimensional and two-dimensional grid as the assumed circulations interfered with their neighbors. The authors also found that the presence

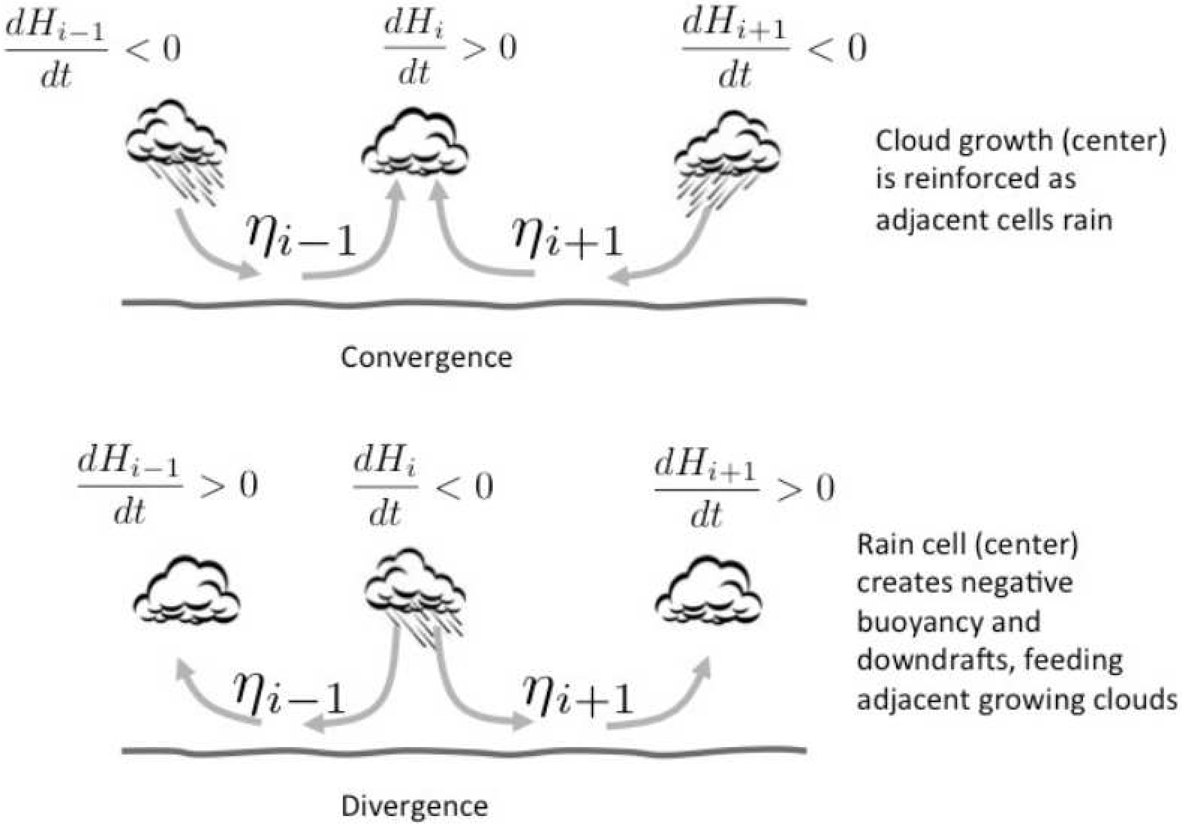

Figure 1.4: An illustration of the coupling process through changes in cloud depth driving the Koren and Feingold model. Figure rights belong to Feingold and Koren (Feingold and Koren 2013).

of coupling can produce a stable oscillation in cloud depth for a precipitating cloud that might otherwise be unstable. The damping effect that coupling has on its neighbors suppresses runaway cloud growth to some extent.

Most importantly, the Koren and Feingold model introduced the concept of dynamic coupling to simple cloud models, showing that such a relationship has a pronounced effect in ordering the domain. Mesoscale circulations are omnipresent throughout trade wind cumulus (George et al. 2023), and thus being able to relate cloud size changes to circulation strength is of vital importance in arguing the applicability of simple models to this domain. This method also showed how a very few number of variables can be adapted to approximate other processes, in this case relating cloud depth changes to circulation strength.

1.3.4 Pujol and Jensen model

Pujol and Jensen published a mathematical analysis of the Koren and Feingold model (Pujol and Jensen 2019). While some of this analysis ultimately turned out to be incorrect (Chekroun et al. 2020), the authors also used this opportunity to develop a new set of equations that incorporated water vapor concentrations into a cloud-rain-aerosol simple model. The model combines aspects from both Koren and Feingold and Spassova and Nikolov to simulate clouds based on the cloud water L_c, rain water L_r, and cloud drop number concentration N_d modulating the two, with water vapor L_v as an independent tuneable parameter (Koren and Feingold 2011; Spassova and Nikolov 2005). This model showed similar results to that from Koren and Feingold, exhibiting both damped and chaotic oscillations in equivalent parameter spaces (Koren and Feingold 2011). The model forms clouds after roughly 300 minutes and has a cloud life cycle of around 200 minutes, with peak rain water occurring 20-30 minutes after the peak in cloud water.

$$\begin{aligned}
\frac{dL_c}{dt} &= \alpha A_c(L_v - L_c) - K N_d^{-2} L_c^4 - k_r L_c L_r \\
\frac{dL_r}{dt} &= -A_r L_r + K N_d^{-2} L_c^4 + k_r L_c L_r \\
\frac{dN_d}{dt} &= A_c'(L_v - L_c)(N_0 - N_d) - k_c L_c^2 - k_r L_r N_d
\end{aligned} \tag{1.6}$$

This model was then applied to real world cloud organization by ingesting observational data from tropical Reunion Island in the Indian Ocean and urban Lille in France (Mascaut et al. 2022). By providing the model with time-varying measurements of N_0, L_v, and RH and optimizing the kinetic constants within physically possible ranges, the authors were able to simulate the real cloud fields with some degree of accuracy, albeit with very coarse resolution. Both satellite observations and ERA5 data verified that the simple model correctly identified both formation/dissipation locations and times as well as the proper orders of magnitude of cloud water concentrations. In addition, the model was accurate enough to make estimates of the radiative effect of the cloud fields. While such simple models are not suitable for being detailed forecasting tools, and the authors clarify as such, the results of this model show that there is sufficient evidence of their capability to produce real world patterns and from there to gain insight into what drives these patterns to form (Pujol and Jensen 2019).

1.4 Structure of this work

This dissertation is structured to answer and assess three research questions:

1. Can different patterns of shallow cumulus be represented by a simple cloud model?
2. What are the critical physics driving sugar to evolve into gravel and flowers?
3. To what extent is a simple model useful for analysis as compared to an LES?

Both chapters 2 and 3 will evaluate questions 1 and 2 separately by developing two different simple models. We hypothesize that such a model does indeed exist and is capable of producing at minimum the patterns of sugar, flowers, and gravel by virtue of coupling the model in a physical manner and adjusting the environmental conditions. We believe that an environment containing a strong boundary layer inversion and pronounced vertical velocity gradients representing circulations is necessary to produce flowers, while gravel requires an environment of frequent precipitation and cold pool effects. This will be measured by assessing the relative influence of each model term to produce each pattern.

Question 3 will be evaluated in chapter 4 by comparing our simple model results to that of an LES case study. We will assess which of the LES results are reproducible using the simple model and continue the analysis using both models to answer whether circulation strength or moisture content is of higher importance in determining flower size, and compare those results.

Chapter 2 has been submitted to the Journal of Geophysical Research and is currently under review. Data for this chapter is available at https://doi.org/10.5281/zenodo.16856475. Chapter

3 is presently being edited with intent for publication at the same journal, with data available at https://doi.org/10.5281/zenodo.17503919.

Chapter 2

A Simple Cloud Model Using Four Prognostic Equations for Cloud Water, Rain Water, Cloud Drop Number, and Vertical Velocity

2.1 Introduction

Radiation feedbacks from marine shallow cumulus represent a significant source of uncertainty in climate models (Forster et al. 2021). With a warming planet expected to change environmental conditions in the tropics, this will lead to shifts in the way that clouds preferentially organize, possibly influencing cloud-radiation feedbacks and introducing further uncertainty (Bony et al. 2020). Thus, cloud organization and the processes behind it are an important area of study to resolve these uncertainties.

Of the past efforts in classifying cloud patterns, the study by Stevens et al stands out as one with a significant amount of follow-on research into why these patterns form (Stevens et al. 2019; Bony et al. 2020; Narenpitak et al. 2021; Dauhut et al. 2023). Here a group of scientists divided commonly seen shallow cumulus patterns into four subjective categories colloquially termed sugar, gravel, flowers, and fish, based on their size and structure (Stevens et al. 2019). Sugar clouds are small, randomly dispersed clouds with little vertical extent or precipitation; gravel clouds are deeper cumulus with frequent precipitation and organized into lines or arcs; flowers are even larger aggregations of cloud that clear out the surrounding air; fish are skeletal lines of cloud separated by clear air that most resemble a fishbone structure, cover larger areas (order 1000 km), and are associated with frontal passages (Stevens et al. 2019). Field studies such as the EUREC^{4}A campaign show that these patterns exist in different environmental conditions, possibly making them sensitive to changing climate (Kazil et al. 2024; Narenpitak et al. 2021).

Bony et al showed that the two most highly organized patterns, gravel and flowers, exist in environments of stronger surface wind, while the two deepest clouds, flowers and fish, occur in the presence of a stronger boundary layer inversion (Bony et al. 2020). Flower-type clouds in particular have been a focus of study in the past decade, with LES used to investigate the mesoscale circulations that drive moisture to aggregate (Bretherton and Blossey 2017; Dauhut et al. 2023). Indeed, mesoscale circulations are a key feature of many trade-wind environments and play a significant role in the interactions between clouds and the resulting patterns (George et al. 2023; Chen et al. 2023).

While LES are highly useful tools for studying microphysical processes within these cloud patterns, they are also computationally expensive and complex. Simple cloud models are a way to represent cloud growth and decay while being able to separate and isolate individual processes at low computational cost (Spassova and Nikolov 2005; Koren and Feingold 2011). These models are best exemplified by the predator-prey relationship of Lotka and Volterra, which illustrates feedbacks between two interrelated populations (Lotka 1910; Berryman 1992). As applied to cloud systems, cloud water is the prey in this scenario while rain water is the predator (Koren and Feingold 2011). Several studies have applied this concept in theoretical models. Wacker developed a predator-prey model to investigate the competition between different cloud and precipitation species, showing how one or more hydrometeor types can dominate or stably coexist in different environments (Wacker 1995). Spassova et al adapted the Wacker model into a nonlinear chaotic system by including equations for vertical velocity and water vapor concentration, demonstrating the various dynamical solutions of such a system based only on the internal physics, albeit in a less relevant physical regime (Spassova and Nikolov 2005). Koren et al derived a model of cloud depth (as a proxy for cloud water concentration) and rain rate, mediated by the aerosol, to reproduce some aspects of non-precipitating and precipitating warm shallow cumulus cloud systems, later coupling the model through inferred horizontal motions to show the synchronization of cloud life cycles within a cloud system ((Koren and Feingold 2011; Feingold and Koren 2013)). The viability of this model was verified by Chekroun et al (Chekroun et al. 2020). Pujol et al presented another

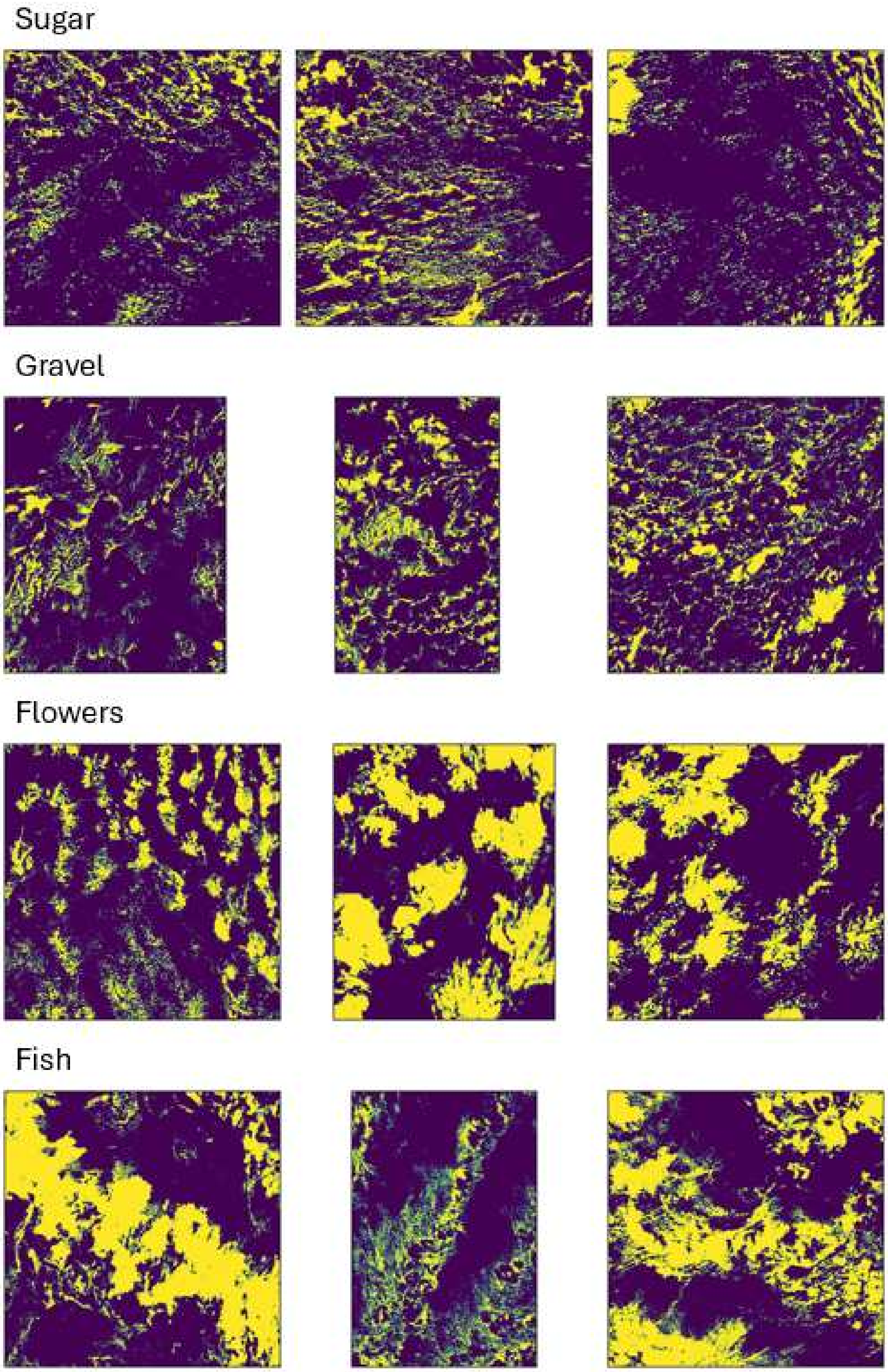

Figure 2.1: Diagram of the four cloud patterns: sugar, gravel, fish, and flowers, identified by Stevens et al (Stevens et al. 2019). Images are collected by Terra/MODIS and available from NASA Worldview (NASA 2024).

simple model focused instead on water vapor-aerosol interactions, using observations to then simulate the evolution of real-world cloud fields ((Pujol and Jensen 2019; Mascaut et al. 2022)).

We thus know that simple models can produce some characteristics of real cloud fields, and that the realism depends on both their environment and interactions to self-organize. The focus of this study is to combine these two ideas and ask: can a simple cloud model coupled physically across a two-dimensional grid be used to recreate common patterns seen in tropical shallow cumulus? If so, what does this model then say about the dominant processes for both forming cloud patterns and aggregating condensate, and how realistic is our model compared to existing observational studies? The next section describes our model, followed in section 3 by a detailed analysis of model output, answering the two main questions above. The paper is closed by a summary and conclusions.

2.2 Methodology

2.2.1 Model Development

The primary variables with which we define our system are the cloud water concentration q_c, the rain water concentration q_r, and the cloud drop number concentration n_c. Our focus is on warm-cloud processes, so all condensed water is present in the liquid phase. In order to represent the circulations, we also include an equation for vertical velocity w. Our basic cloud box model is 0-dimensional, making these quantities vertical averages. The evolution is described by the following nonlinear ordinary differential equations:

$$\frac{\partial q_c}{\partial t} = d_5 w q_c - d_6 \frac{q_c^3}{n_c^2} - d_7 q_c q_r - E + c_{precip,q_c} + c_{top,q_c} \tag{2.1}$$

$$\frac{\partial q_r}{\partial t} = d_6 \frac{q_c^3}{n_c^2} + d_7 q_c q_r - d_8 q_r + P - E \tag{2.2}$$

$$\frac{\partial n_c}{\partial t} = d_9(n_a - n_c) - d_{10}q_c^2 - d_7 n_c q_r + c_{precip,n_c} + c_{top,n_c} \tag{2.3}$$

$$\frac{\partial w}{\partial t} = -\epsilon_w \frac{w^2}{H} - \frac{g}{\rho}(q_c + 0.1q_r) + f_w + \frac{d_3 d_5}{\rho} w|w|q_c - \frac{d_4}{\rho} q_r - d_p w^3 + c_{diff} \tag{2.4}$$

This model builds on previous work presented by Spassova et al, Feingold et al, and Pujol et al (Spassova and Nikolov 2005; Feingold and Koren 2013; Pujol and Jensen 2019). Effects of heating on the vertical motions as well as cloud-cloud interactions have been added to couple individual cloud-box models in a 2-dimensional array to form patterns commonly seen in the real world.

The basic physics described by the equations is as follows and is summarized in table 2.1. In equation 2.1, the condensation and diffusional growth of cloud water is combined into a single term $d_5 w q_c$, representing that both these processes are enhanced by updrafts, i.e. adiabatic cooling, and by the cloud-water concentration itself. We make the assumption that a sufficient source of water vapor is present in the tropical environment to allow for supersaturation and subsequent droplet growth in rising air. Equation 2.3 contains a corresponding relaxation term to a background aerosol concentration, written as $d_9(n_a - n_c)$ in alignment with Mascaut et al (Mascaut et al. 2022). This is a very crude parameterization of the complicated aerosol-cloud interactions and most closely represents the nucleation of cloud drops.

Collision-coalescence processes describe the transition from cloud to rain water in the form of autoconversion ($d_6 \frac{q_c^3}{n_c^2}$) and accretion ($d_7 q_c q_r$) in equations 2.1 and 2.2. These processes are parameterized following the work of Khairoutdinov et al using a simple nonlinear combination of the interacting terms (Khairoutdinov and Kogan 2000). Seifert et al later derived the autoconversion and accretion terms for n_c in equation 2.3 as $d_{10}q_c^2$ and $d_7 n_c q_r$, respectively (Seifert and Beheng 2001). Once tracked water has been transitioned into rain, precipitation depletion then removes this water from the system in equation 2.2 as $d_8 q_r$. This process is simply a function of the amount of rain water present: the more rain water in the cloud, the faster the precipitation rate.

Processes based on controls external to the cloud are included as constants. Entrainment E in equations 2.1 and 2.2 is considered to be a function of the environmental wind inducing turbulence along the cloud boundaries, mixing dry air into the cloud and evaporating both cloud and rain water. We also include a constant P in equation 2.2 representing the auto-seeding of large droplets at cloud-top and the divergence of precipitation through the cloud layer, which forces a constant small concentration of rain water as adapted from Wacker and Spassova et al (Wacker 1995; Spassova and Nikolov 2005).

The equation for vertical velocity in equation 2.4 derives from the vertical velocity tendency equation (Tao and Li 2016), defined as

$$\frac{\partial w}{\partial t} = -\frac{\partial}{\partial x}uw - \frac{1}{\overline{\rho}}\frac{\partial}{\partial z}\overline{\rho}ww + g(\frac{\theta^{'}}{\overline{\theta}} + 0.61q_v^{'} - q_l) - C_p\overline{\theta}\frac{\partial \pi^{'}}{\partial z} + D_w \tag{2.5}$$

The horizontal advection in equation 2.5 is included via the coupling term, described in the next section, whereas the vertical advection in equation 2.5 is included in equation 2.4 as $-\epsilon_w \frac{w^2}{H}$ and is a form of Burgers' conservation equation for convective motion (Burgers 1948). This term is an approximation of vertical advection over the depth of the cloud according to the relationship

$$w\frac{\partial w}{\partial z} \approx \epsilon_w w \frac{w}{H} \tag{2.6}$$

where H is the representative cloud depth and ϵ_w is a function of the vertical density gradient (Spassova and Nikolov 2005). Latent heat release in equation 2.5 ($g\frac{\theta^{'}}{\overline{\theta}}$) is split into two terms in equation 2.4 to represent both condensational heating and cold pool effects. Condensational heating ($\frac{d_3 d_5}{\rho} w|w|q_c$) is a direct function of the condensation term in equation 2.1, which describes the amount of cloud water formed, multiplied by the absolute value of w to increase the effect of vertical motion. Cold pools are assumed to exist in the presence of precipitation and are thus included as $\frac{d_4}{\rho} q_r$. Buoyancy in equation 2.5 ($0.61 g q_v^{'}$) is parameterized in equation 2.4 as the constant f_w as we do not include water vapor concentrations in our model, again assuming a sufficient source to induce vertical motion. The gravitational drag of liquid water is a very straightforward transition into equation 2.4 as $-\frac{g}{\rho}(q_c + 0.1 q_r)$, also allowing the effects of cloud water to dominate.

The vertical pressure gradient force ($PGF = C_p \theta \frac{\partial \pi^{'}}{\partial z}$) is tricky to adapt to our model as we have neither pressure nor a vertical coordinate. We thus argue that this term is included with the latent heating effect as condensational heating leads to an upward-directed pressure gradient and evaporation to a downward pressure gradient. Aligning this process to changes in q_c gives an equivalent term to our parameterization for latent heating. Finally, we include a turbulent dissipation term $d_p w^3$ as a function of the vertical velocity, with stronger vertical motions producing stronger turbulent eddies.

This model uses 11 different internal parameters and 3 external parameters to define the cloud environment. These parameters are defined using a combination of environmental observations, unit analysis, and model tuning to balance the terms in the equations, resulting in a model that produces stable solutions. The parameters and their associated model terms are summarized in table 2.1. The model is then converted into a non-dimensionalized form as described in Appendix A.

2.2.2 Model Coupling

The terms discussed thus far in equations 2.1-2.4 describe the growth and decay of single cloud elements. These four equations also include coupling terms across a 2-dimensional array to advect condensate and momentum around the grid to create the different cloud patterns. Cloud elements are coupled through three different processes, depicted in figure 2.2 and described below.

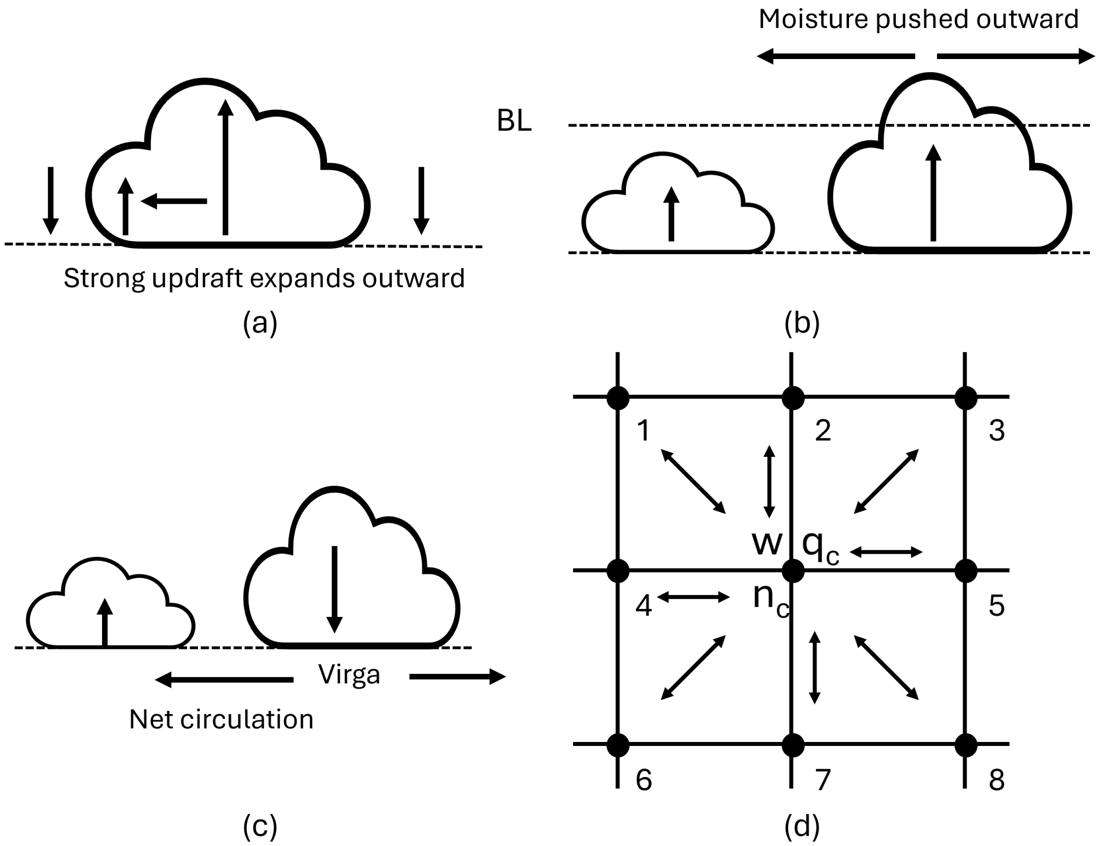

Figure 2.2: The three coupling methods used in the model are the (a) w diffusion, (b) cloud-top coupling, and (c) virga coupling. Each coupling process is a function of the circulation. (d) illustrates the grid over which these interactions occur, with each central point exchanging w, q_c, and n_c with its eight neighbors indicated by the arrows.

Table 2.1: Summary of model terms and tuneable parameters in equations 2.1-2.4.

Model Term	Physical Meaning	Associated Parameter	Units
$d_5 w q_c$	Condensation	d_5: condensation length scale	$1/m$
$d_6 \frac{q_c^3}{n_c^2}$	q_c autoconversion	d_6: autoconversion rate	$1/kg^2\ s$
$d_7 q_c q_r$	q_c accretion	d_7: accretion rate	$m^3/kg\ s$
$d_8 q_r$	Precipitation depletion	d_8: precipitation rate	$1/s$
E	Entrainment	-	$kg/m^3\ s$
P	Precipitation influx	-	$kg/m^3\ s$
$d_9(n_a - n_c)$	n_c activation	d_9: activation rate	$1/s$
$d_{10} q_c^2$	n_c autoconversion	d_{10}: autoconversion rate	$m^3/kg^2\ s$
$-\epsilon_w \frac{w^2}{H}$	Vertical w advection	H: average cloud depth	m
$\frac{g}{\rho}(q_c + 0.1 q_r)$	Gravity drag	ρ: average air density	kg/m^3
f_w	Instability	-	m/s^2
$\frac{d_3 d_5}{\rho} w\|w\| q_c$	Latent heating	d_3: latent heating strength	$unitless$
$\frac{d_4}{\rho} q_r$	Cold pools	d_4: cold pool negative buoyancy	m/s^2
$d_p w^3$	Damping	d_p: turbulent diffusion rate	s/m^2
c_{diff}	w diffusion	γ_1: turbulent mixing strength	$1/s$
c_{top}	Cloud-top coupling	γ_2: inversion strength	$1/m$
c_{precip}	Virga coupling	γ_3, γ_4: subcloud mixing strength	$1/m$, $1/m\ kg$

Vertical Velocity Diffusion

The first process of coupling is the horizontal diffusional growth of vertical motions through subgrid-scale turbulent motions. As updrafts and downdrafts grow stronger, they expand horizontally with the strongest motions dominating. This is described mathematically as

$$c_{diff} = \frac{1}{8}\gamma_1 \sum_{i=1}^{8} h_i (f_i w_i - f w) \tag{2.7}$$

where $f = \frac{|w|}{|w_{max}|}$ at each grid point with w_{max} being taken across the whole domain. The subscript i points to each of the eight grid points surrounding the point of interest between which the coupling is calculated. $f_i w_i - f w$ thus represents the w flux between a neighboring cloud and the cloud of interest, respectively. The weighting factor f enhances the effect of the larger vertical motions dominating over the smaller ones. Additionally, coupling is weighted by the inverse of the distance to its direct neighbors, h_i, where clouds on the diagonal are further away and thus have a smaller impact. Finally, the coupling weight γ_1 defines the strength of this coupling and has units of s^{-1}.

Cloud-Top Advection

The second coupling process is through cloud-top advection of q_c and n_c. Here, clouds reaching the boundary layer inversion will be forced to grow horizontally, transporting condensate at cloud top in the direction of the circulation by the equation

$$\begin{aligned} c_{top,q_c} = \frac{1}{8}\gamma_2 \sum_{i=1}^{8} & -h_i max(w - w_i, 0) max(A - 1, 0) q_c \\ & + h_i max(w_i - w, 0) max(A_i - 1, 0) q_{c,i} \end{aligned} \tag{2.8}$$

with an equivalent equation for n_c. The amount of q_c and n_c being transported depends on the direction of the circulation. This is defined using max functions, such that motion from cloud 1 to cloud 2 will advect a portion of cloud 1's condensate, while motion from cloud 2 to cloud 1 will advect a portion of cloud 2's condensate. The advection is further defined as a function of the inversion height, represented by the parameter A, where

$$A_i = \frac{q_{c,i}}{q_{c,max}} \tag{2.9}$$

We make the assumption that q_c increases linearly with height such that we can define a domain-wide value of $q_{c,max}$ to represent the inversion height of the environment (Nicholls 1989). Cloud-top advection will occur when q_c reaches $q_{c,max}$, i.e., when the cloud top reaches the inversion level. Clouds below this height will simply grow vertically instead of horizontally. For n_c this advection process is the same, simply substituting q_c for n_c as the advected quantity. The strength of this coupling term is defined by γ_2 and has units of m^{-1}.

Virga Advection

The final coupling process is via the advection of q_c and n_c in the presence of precipitation. When a cloud precipitates, virga forms beneath the cloud. This condensate is then circulated to provide an external source of cloud water and cloud drops to neighboring cloud elements. The process is defined as the following:

$$\begin{aligned} c_{precip,q_c} &= \frac{1}{8}\gamma_3 \sum h_i(w - w_i)q_{r,i} > 0 \\ c_{precip,n_c} &= \frac{1}{8}\gamma_4 \sum h_i(w - w_i)q_{r,i} > 0 \end{aligned} \tag{2.10}$$

in which the > 0 denotes that the term is only active when it is positive. Again, the direction of the circulation determines whether virga is advected into its neighbors, with the concentration of virga being a function of the amount of rain water. We only take the positive values of advection here, as any motion directed away from the cloud is assumed to circulate condensate into the below-cloud space as opposed to ingesting it into the cloud. γ_3 and γ_4 control the strength of the coupling for q_c and n_c and have units of m^{-1} and $m^{-1}kg^{-1}$, respectively.

2.2.3 Classification of Cloud Patterns Using Satellite Data

In order to analyze how the model compares to observed cloud fields as well as the difference between the patterns, we will use several metrics of comparison. First, we look at the average size of clusters and intervening clear areas over time, as well as the number distribution of cloud sizes. A cluster is defined as all immediately adjacent grid points exceeding a certain threshold of q_c surrounded by clear air. Sugar and gravel have smaller cloud elements compared to flowers, while gravel and flowers are more effective at clearing out their surroundings compared to sugar, so comparative values in these metrics with observations of the different cloud patterns will be used to differentiate between the model patterns. Fish, which are associated with frontal passage and thus tied to the large-scale environment, will not be simulated using this simple model.

We also use the organization index I_{org} as defined by Tompkins et al (Tompkins and Semie 2017). This metric calculates the cumulative distribution function (CDF) of the nearest neighbor distances between each cluster centroid, then compares it to the control CDF of a purely random distribution. A field that develops randomly will lie along the control line and have $I_{org} = 0.5$. If the model CDF lies well above the random CDF, then the pattern is dominated by small distances between centroids and is classified as “clustered" with $I_{org} > 0.5$. A model CDF below the random CDF is dominated by large distances between centroids and is classified as “regular" with $I_{org} < 0.5$. We calculate the average resulting I_{org} using a series of different initial conditions with error bars of one standard error.

2.3 Results

MODIS imagery at 1 km resolution from 9 Feb 2017 in the tropical central Atlantic is used to initialize the cloud field in the model by taking a portion of the image and converting it to a binary “cloud/no-cloud" field. This initial cloud field is then used to set the values for q_c by defining a maximum q_c in cloud as a function of cloud size following the relation $q_c \approx \alpha A_r^{\beta}$ where A_r is the cloud area, $\beta = 0.3$, and $\alpha = 60 \times 10^{-6}$ scaled to produce a realistic range of q_c (Feingold et al. 2017; Koren and Feingold 2011). q_c varies in cloud between a threshold value of $0.05\ g/m^3$ estimated from Chiu et al and this size-dependent max q_c (Chiu et al. 2021). Points outside of the cloud have a randomly varied q_c between 0.001-0.02 g/m^3, below the threshold of visible cloud. The remaining three variables are initialized using a Gaussian random field with no spatial correlation. This randomization results in clouds at different points in their life cycle. The initial field was placed into three different environments as represented by changing the environmental parameters in table 2.2 and allowed to evolve over time into the patterns shown in figure 2.4. Five runs using different cloud scenes from this day have been used to initialize the model for each set of environmental parameters for statistical purposes, with one set of representative results being shown here. All initial conditions with their associated outputs are shown in appendix A. The initial conditions were kept consistent between model runs of the different patterns (as opposed to initializing sugar with sugar, flowers with flowers, etc) to verify that the resulting pattern is the product of changing the environmental parameters given in table 2.2 and not the initial conditions. The model domain size is 100 km × 100 km (with resolution determined by the initial conditions)

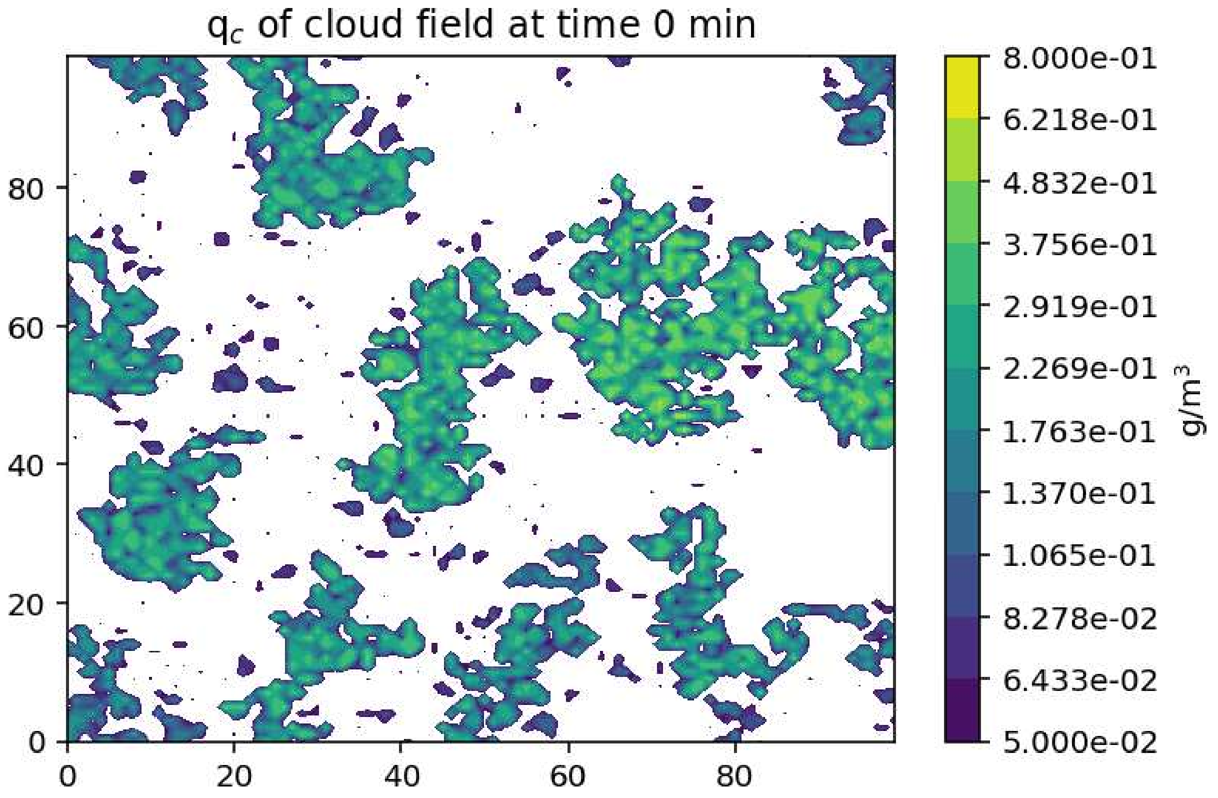

Figure 2.3: Initial cloud field using MODIS imagery with 1km resolution from 9 Feb 2017 at 1518UTC. Maximum q_c in cloud follows a power law distribution as a function of cloud area.

and the boundaries are periodic. Output is calculated every 0.1 minutes over a total span of 500 minutes.

Table 2.1 lists the tunable parameters within the model for an individual cloud as well as their coupling strength. Values of these parameters are based on a combination of observations, modeling studies, and unit/scale analysis, then varied incrementally with the final pattern in mind. Of this list, varying seven key parameters, shown in table 2.2, results in different terms in the equations dominating and producing the different patterns that emerge. For our model, these key parameters include the environmental instability (called 'buoyancy'), the latent heating strength, the turbulent diffusion rate, the condensation rate, the inversion depth, the w diffusion rate, and the cloud-top coupling strength. The parameters themselves are fairly sensitive as most fall within the same order of magnitude between the three patterns, with the exception of the coupling strengths and the latent heating.

These parameter values and variations have different meanings for the environments necessary to produce these patterns. The environmental instability primarily balances the gravitational drag in our model and so is of a similar magnitude. For q_c values on the order of $1e^{-5} - 1e^{-4}\ kg/m^3$, we thus parameterize the constant f_w in the range of $1e^{-4} - 1e^{-3}\ m/s^2$. This parameter is related to the variation in temperature between the cloud and the environment, but also can be tied to the sea surface temperature impacting the atmospheric profile in the tradewind inversion layer. A stronger latent heating rate equates to a larger temperature gradient between the cloud and its surroundings, enhancing both the temperature and pressure perturbations and inducing stronger vertical motions. For our model, this is a unitless parameter that scales the term to balance others in equation 2.4, which for the dominant buoyancy and gravitational drag places d_3 in the range of $1e^3$. The turbulent diffusion rate is fairly straightforward, being a measure of the turbulent dynamics within a cumulus cloud, and is large enough to counteract typical vertical motions in shallow cumulus on the order of $1\ m/s$ ((Heiblum et al. 2016b)).

Variations in the condensation efficiency parameter fall around $4.45e^{-3}\ s^{-1}$ using the study from Spassova et al (Spassova and Nikolov 2005). The inclusion of vertical velocity in our parameterization of q_c condensation allows us to adapt this value to our model by dividing by typical values of w at around $1\ m/s$. This parameter can be thought of as directly proportional to supersaturation and thus inversely proportional to temperature, where a higher in-cloud supersaturation (which for constant moisture means a lower saturation vapor pressure or lower temperature) allows for condensation to occur more quickly. The inversion depth is a property of the large-scale atmospheric environment, whereby assuming a range of cloud depths for typical shallow cumulus we can thus define a peak q_c. For cloud depths of $100 - 1000\ m$ (Spassova and Nikolov 2005) and a scaling factor of $2e^{-6}\ kg/m^4$ as a function of cloud-base temperature and pressure (Koren and Feingold 2011), a linear change in liquid water content gives a range of peak q_c of $0.1 - 1\ g/m^3$.

Table 2.2: Parameters varied within the model to produce sugar, flowers, and gravel.

Parameter Name	Sugar	Flowers	Gravel
Buoyancy f_w (m/s^2)	$3.5e^{-4}$	$1e^{-4}$	$1e^{-4}$
Latent heating d_3 $(unitless)$	$4e^2$	$5e^3$	$6e^3$
Turbulent diffusion d_p (s/m^2)	0	$2e^{-2}$	$2e^{-2}$
Condensation d_5 $(1/m)$	$1e^{-3}$	$3.5e^{-3}$	$6e^{-3}$
Peak q_c at inversion (g/m^3)	0.4	0.5	0.7
w diffusion γ_1 $(1/s)$	$5e^{-6}$	$2e^{-3}$	$5e^{-1}$
Cloud-top advection γ_2 $(1/m)$	$1e^{-5}$	$4e^{-2}$	$1e^{-5}$

The coupling strength relates to the strength of horizontal mixing. For vertical velocity diffusion, this is horizontal mixing due to turbulence, which is enhanced by cold pool dynamics. Turbulence reduces the time scale for mixing, which aligns with parameter units of $1/s$. Cloud top advection is a function of inversion strength, as a stronger inversion precludes moisture from penetrating as deep, given parameter units of $1/m$, and thus forcing a larger percentage of condensate horizontally.

In order for the model to form clouds at all, the minimum required terms are the gravitational drag, condensation, and precipitation. Without these processes, the initial cloud field either experiences unrestrained growth in the absence of the primary sinks of w/q_r or completely dissipates from a lack of new q_c. The weaker sugar pattern is also found to need sufficient environmental instability to counteract the decay to produce a persistent cloud field. Flowers in this model need both increased latent heating and decreased environmental instability to produce a significant amount of cloud water, then strong advection at cloud top to redistribute this water resulting in aggregation. Here, the lower instability prevents all but the deepest clouds, the flowers, from reforming in the intervening clear space. Gravel needs a strong rate of condensation as well as very strong vertical velocity diffusion coupling to redistribute the cloud from a clustered to an arc-like pattern. In this model both flowers and gravel require turbulent damping to counteract the larger vertical motions, whereas sugar does not.

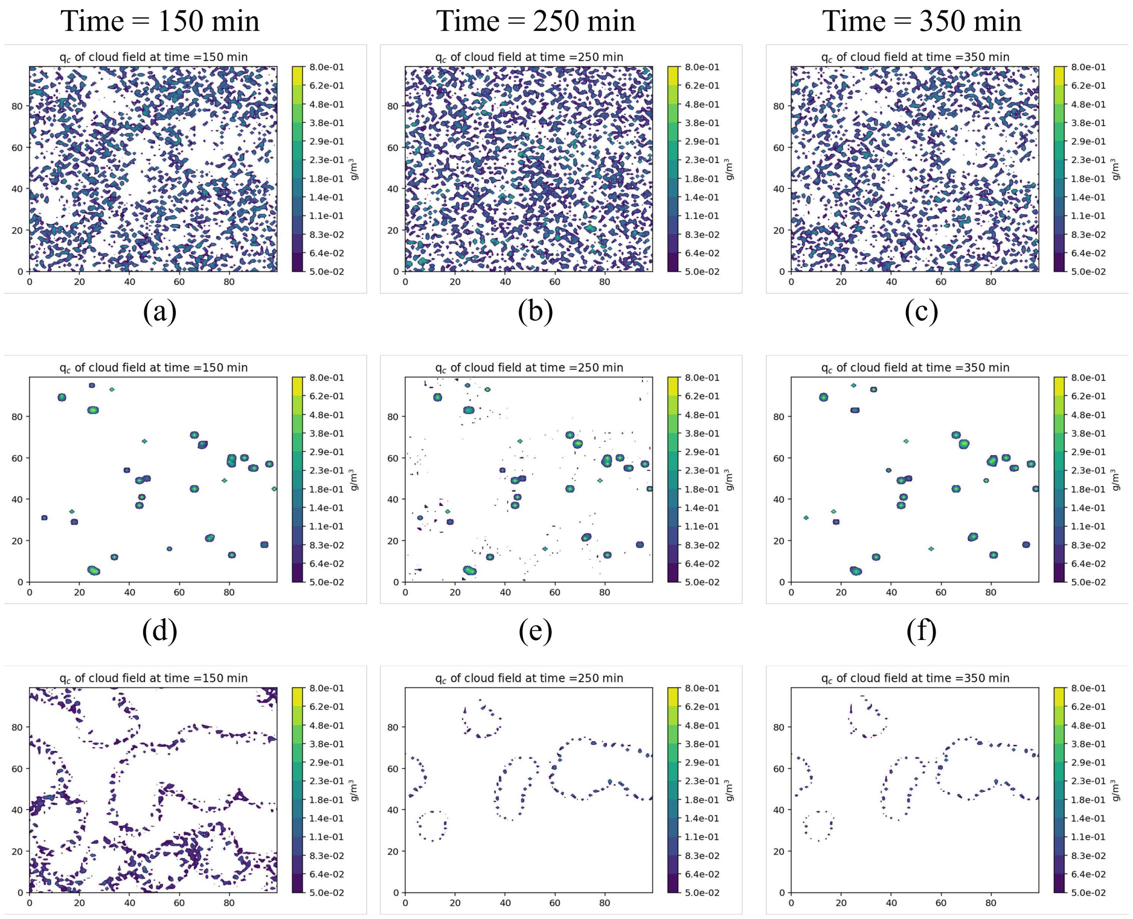

(a) (b) (c)

(d) (e) (f)

(g) (h) (i)

Figure 2.4: Evolution of q_c from the initial field in figure 2.3 at t = 150 min (a,d,g), t = 250 min (b,e,h), and t = 350 min (c,f,i) into the three different patterns of sugar (row 1), flowers (row 2), and gravel (row 3). The domain size is given in km based on the resolution of the initial conditions.

2.3.1 Sugar

Sugar forms in this model in an environment of higher instability, lower available moisture, a shallower boundary layer, weak turbulence, and very weak coupling. These results align with observations reported by Bony et al with sugar appearing in the presence of weak surface winds, high SSTs, and a weak inversion indicative of an unstable atmosphere with little to no mesoscale circulations (Bony et al. 2020). The field weakens considerably from the initial conditions over the first 20 minutes as the large clouds break up before reaching a periodic oscillation with q_c ranging from 0.01-0.3 g/m^3, matching with both observations and LES simulations (Chiu et al. 2021; Xue and Feingold 2006). Individual clouds have a lifetime of 7-65 minutes with a mean of 51 minutes, which falls within the range of values for modeled shallow cumulus (Heiblum et al. 2016a). Clouds also combine and advect about the domain as illustrated in Fig 2.4. The presence of the coupling results in some synchronization of the cloud cycles over time with a period of around 3 hrs, despite the initial randomization of variables other than q_c and the low overall coupling strength. This may be a physical artifact of the model itself as all patterns exhibited this synchronization to some degree. Vertical velocity across the domain is around ± 2 m/s and there is little to no precipitation.

The average modeled cloud element size is about half that of the average void size. Cloud size has more variation as observed in nature compared to our model, but a histogram of cloud sizes in fig 2.5 shows that the smallest cloud elements make up around 70$\%$ of the field with the number of clouds in each size bin dropping off exponentially with cloud diameter at a similar rate to that observed in nature. The I_{org} index for the model run is calculated at 0.75$\pm$0.11, indicating a clustered distribution by the above definition with a preference for small inter-cloud distances and falling around the typical I_{org} values reported by Bony et al of 0.6-0.8 (Bony et al. 2020).

The relative strength of the different terms, shown in figure 2.6, highlights which processes are dominant in the development and maintenance of sugar (blue bars). These include the buoyancy and gravitational drag of liquid water for w, condensation for q_c, precipitation depletion, precipitation influx, and entrainment for q_r, and activation for n_c. The high instability in our model

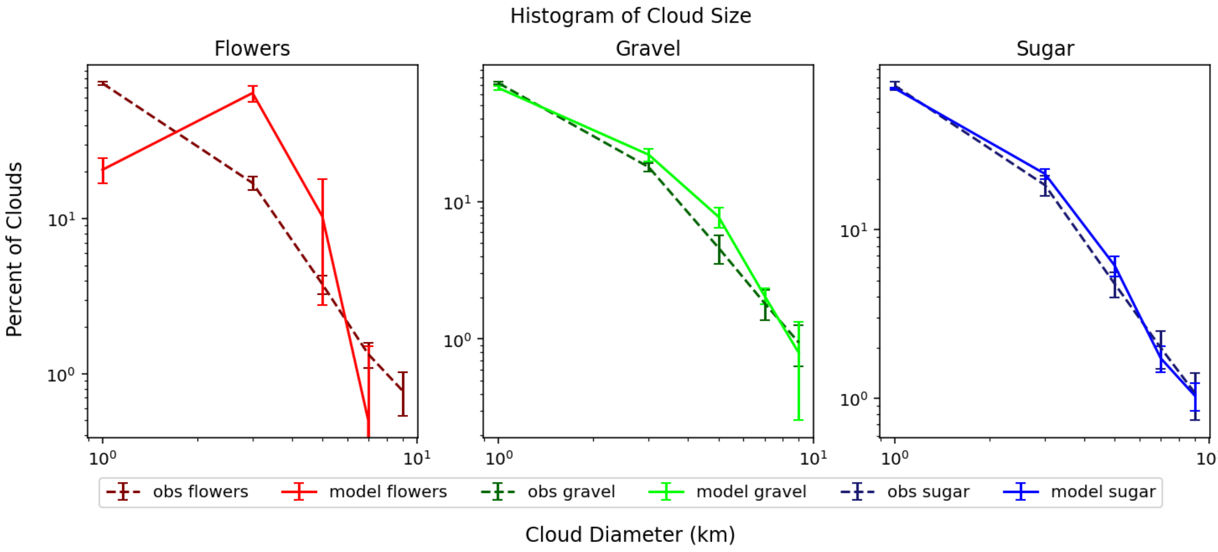

Figure 2.5: Histogram of cloud sizes for model output (solid lines) vs observed cloud fields (dashed lines) for flowers (left), gravel (center), and sugar (right). Observed cloud distributions are calculated using MODIS 1km data from Apr 2017 and visually classified into patterns. Model distributions are calculated following pattern formation using five different sets of initial conditions. The error bars show one standard deviation from the mean. Each point represents a bin width of 2km.

allows these small cloud elements to grow, whereas all but the strongest clouds are suppressed when the instability is decreased. As we know that latent heating is linked to the strength of vertical motions as well as precipitation formation, the low importance of latent heating in these small, non-precipitating clouds means that another source of instability must be present to produce updrafts (Tao and Li 2016). The higher instability also compensates for the lower available moisture, represented by the lower condensation rate and seen in the low values of q_c. Gravitational drag of water drops serves as the dominant sink regulating w, as the other possible sinks are functions of a small w or q_r. Condensation and activation are the dominant processes in forming clouds as they are the only source of q_c/n_c in the absence of any significant mesoscale circulations that might otherwise aggregate condensate (Narenpitak et al. 2021).

It is important to note that values of q_r for sugar are around $1e^{-6}\ g/m^3$, which are far less than what we observe for a precipitating cloud (Chiu et al. 2021). Therefore, the processes that dominate this equation are not actually of physical importance if none of them produce precipitation. As

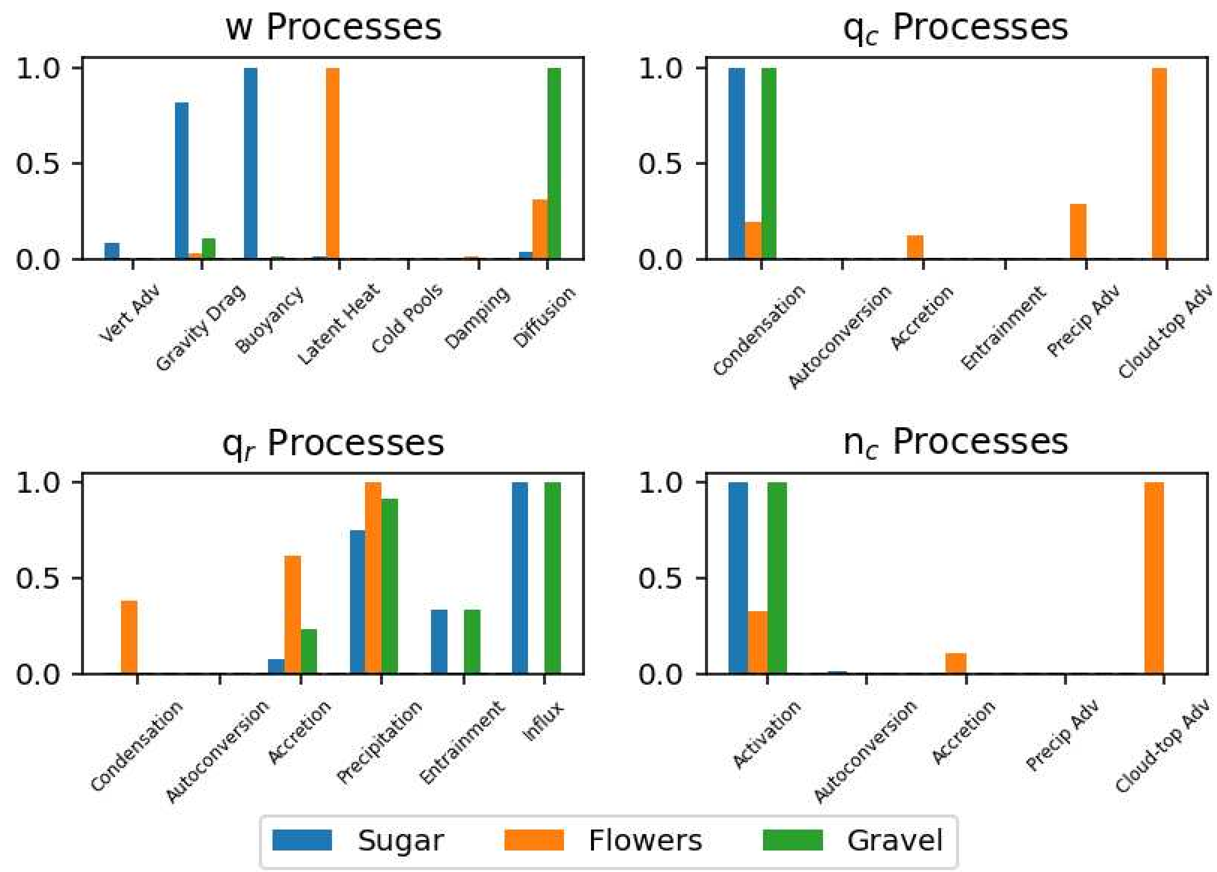

Figure 2.6: Normalized mean term strength for sugar (blue), flowers (orange), and gravel (green) for a point in-cloud following pattern formation. Processes are time-averaged once the defining pattern has formed and stabilized, then normalized for each variable and pattern. For example, in the vertical velocity processes panel, for flowers (orange), the mean latent heating effect dominates the vertical velocity as compared to the mean magnitude of the other terms controlling w for that pattern.

noted previously, precipitation depletion is important for maintaining overarching model stability by preventing q_r from growing out of control and is thus expected to influence q_r for any cloud field. The other terms in the q_r equation are so small that it allows the constant entrainment and influx terms to appear important. However, all terms controlling q_r for sugar are minuscule compared to those in flowers and gravel and so we will not draw conclusions from them about their relative importance.

The I_{org} index is used to measure the impact of different individual processes independently affecting pattern organization by systematically removing one process at a time and recalculating the index. The change in the index compared to the control run with all processes present shows whether each pattern is still capable of forming in the absence of one process and is presented in figure 2.7. For sugar, these critical processes are q_c condensation, precipitation depletion, and gravitational drag, which are critical for all patterns, as well as the vertical advection of w, environmental buoyancy, and entrainment. As mentioned previously, strong buoyancy appears to drive updrafts for the small sugar clouds without impacts from latent heating. Individual sugar clouds also grow to become interconnected in the absence of entrainment, showing that this term is small compared to condensation but significant enough to help break up the clouds into smaller individual elements.

2.3.2 Flowers

The initial conditions produce flowers in figure 2.4 in an environment of lower instability, higher available moisture, a deeper boundary layer, and moderate cloud-cloud interactions, generally aligning with observed windier and more stable environments with a strong inversion (Bony et al. 2020). Aggregation of condensate occurs in the first 20 minutes and clears the regions between clouds by minute 50. Flowers continue to increase and decrease in strength over their life cycle but do not dissipate, with q_c values of 0.1-0.6 g/m^3. Vertical velocity is strongly positive inside the flower at $2-6\ m/s$ with frequent precipitation, while outside the flower both updrafts and downdrafts are small. Around minute 200, conditions in the intervening space are able to initiate a

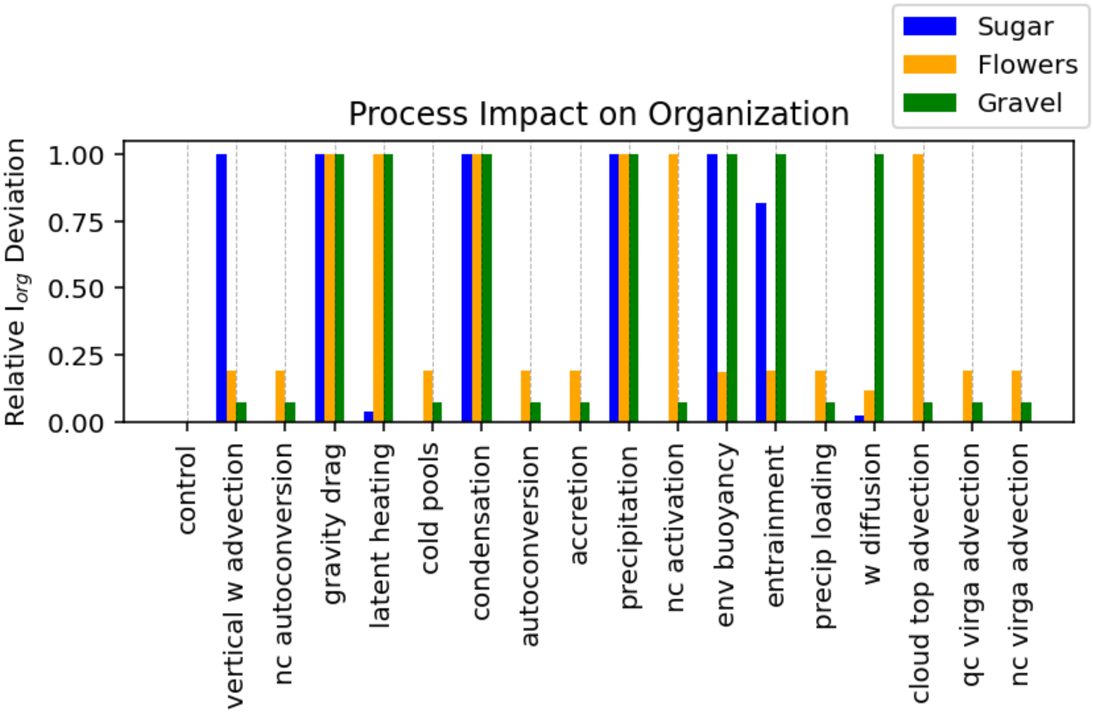

Figure 2.7: Changes in organization by term as shown by the I_{org} anomaly compared to the control run. Each anomaly is calculated as the absolute change in I_{org} after removing one process from the model.

number of smaller clouds but these are again absorbed by the dominant flowers. Our flowers form from initial conditions of both flowers as shown here as well as initializing with sugar.

The flowers in our model are generally circular and uniform in size with intervening clear spaces around 25x larger than the clouds. While the modeled clouds show clear signs of aggregation, the size of these flowers is much smaller than those observed in nature, especially evident from using flowers as the initial conditions. Real world flowers vary in size from around 20 km up to 200 km (Stevens et al. 2019) and show an approximate power law size distribution as seen in fig 2.5. This shows that while our model is capable of aggregating condensate in the domain into distinct small regions, it does not advect enough condensate outward from those small regions to produce a realistically sized flower. The resulting cloud size also appears to be independent of the initial conditions, as multiple different initializations using real-world cloud fields resulted in clouds of similar size. This limits our analysis to discussing the aggregation of condensate, rather than the expansion. The I_{org} index for this pattern is calculated at 0.55±0.02, similar to observed values of 0.5-0.55 and quantifying the clustering that we see.

On the strength of the terms shown in figure 2.6, in addition to the terms required for cloud development, we see that the upward pressure gradient related to latent heating stands out as the dominant process controlling the vertical velocity for flowers. Latent heating enhances the upward motions in the clouds in response to the increased condensation, strengthening the circulations, which aid in aggregation (Tao and Li 2016). The cloud-top advection, both for q_c and n_c, also stands out as dominant terms in forcing condensate to aggregate in the presence of mesoscale circulations (Bretherton and Blossey 2017; Narenpitak et al. 2021). The strength of this advection combined with the larger values of q_c also identifies these clouds as being much deeper in comparison to the sugar and gravel clouds which do not reach the boundary layer inversion. The role of the different coupling processes in the different patterns will be discussed in a subsequent section.

The I_{org} deviation (figure 2.7) tells a similar story regarding which terms are necessary for condensate aggregation. These are the condensation/activation, precipitation depletion, gravity drag, latent heating, and cloud-top advection terms. The first four provide model stability and basic cloud formation, while the latent heating and cloud-top advection are specific to flowers. Interestingly, the environmental instability did not affect the formation of flowers, likely because the latent heating is sufficient to provide buoyancy internally (Tao and Li 2016).

2.3.3 Gravel

The model forms gravel in figure 2.4 after a spin-up time of about 130 minutes, developing along the boundaries of the clouds in the initial conditions and propagating inward before finding a steady state position. The final cloud arcs generally align with the boundaries of the largest initial flowers, suggesting that clouds preferentially form in areas of large q_c gradient. Gravel in this model formed under conditions of stronger condensation, stronger vertical velocity diffusion, and a deeper boundary layer compared to flowers. This generally aligns with the conditions identified by Bony et al, with gravel being present in the presence of stronger winds and a weaker inversion (Bony et al. 2020). Updraft speeds average around 0.4 m/s with locally strong vertical motions up to 10 m/s, with q_c around $0.2\ g/m^3$ and measurable precipitation. The model is able to form gravel from initial conditions of flowers, but not from sugar due to insufficient q_c as the pattern tries to organize.

Gravel in observations has more variation in individual cloud size than does our model output, although the model does still produce fields with cloud number dropping off exponentially with cloud size as seen in figure 2.5. The cloud lines in our model are more disjointed and broken resulting in on-average smaller clouds, compared to the more continuous cloud lines in observations. That being said, the size of the larger-scale features matches more closely, with open cells ranging from 40-100 km in diameter. The I_{org} index for the model is 0.48±0.01, compared with 0.45-0.55 for the observations, indicating a mostly random distribution leaning towards regularly distributed.

The dominating terms in figure 2.6 are generally similar between sugar and gravel, reflective of both patterns being composed of smaller cloud elements as compared to flowers. The primary differences are in the higher q_r accretion, reflective of the increase in rain water from sugar to gravel, and in the vertical velocity diffusion being a dominant term controlling w. Here we believe that the w diffusion is acting in much the same way that a cold pool would by virtue of taking an updraft in a precipitating cloud and propagating it outward, similar to the circulation induced by a gust front with rising air at the gust front edge. The specific cold pool term does not appear to result in significant downward motion within the initial cloud, and as gravel clouds are defined with cold pool structures in mind (Stevens et al. 2019), this leads us to believe that the horizontal effects of cold pools on the vertical velocity are more important than the vertical effects.

Looking at the I_{org} deviation in figure 2.7 we again see the importance of the gravity drag, condensation, and precipitation depletion terms in producing gravel clouds and maintaining model stability. Both latent heating and environmental buoyancy are necessary for producing updrafts in

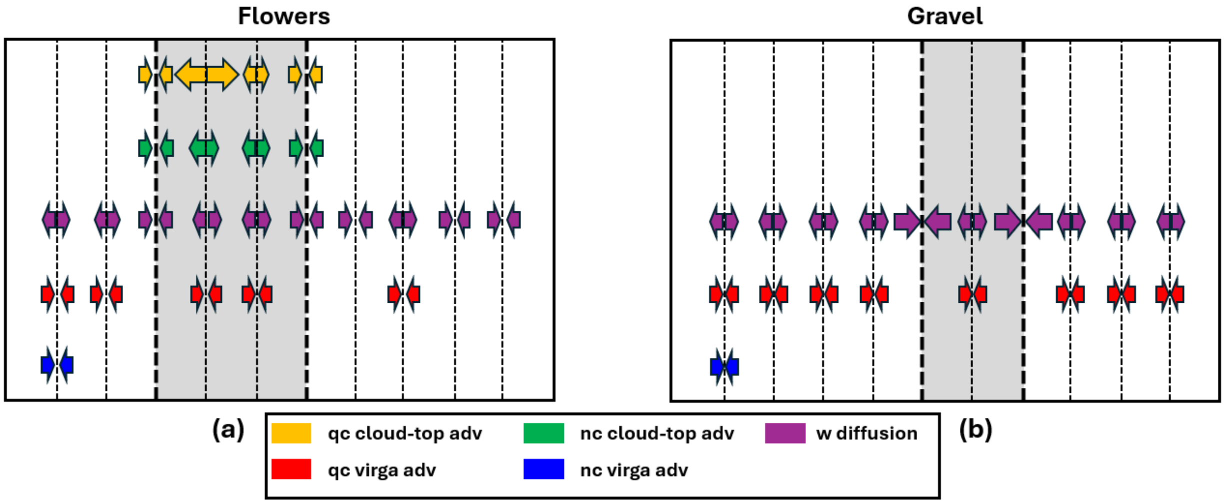

Figure 2.8: Advection term vectors horizontally bisecting a 2-D cloud at one representative time step following pattern formation for (a) flowers and (b) gravel. Direction of arrow shows source or sink of term at each grid point (dashed lines), while arrow length represents relative term strength. The cloud is indicated by the shaded gray region.

an environment of strong horizontal advection; this is in contrast to flowers and sugar, which favor one or the other, respectively. While flowers saw a small deviation in I_{org} as a result of w diffusion, this term has the most impact upon gravel. With the removal of the cold pool term not having an effect, as well as Narenpitak et al finding precipitation to not be essential for flower formation, this further strengthens our suspicion that the w diffusion acts as a cold pool effect here (Narenpitak et al. 2021).

2.3.4 Mesoscale Circulations in Flowers and Gravel

If we look in depth at how this model creates flowers, we find that every location that eventually grows a flower starts with a relatively strong updraft ($w > 0.85\ m/s$) within an area of cloud ($q_c > 0.05\ g/kg$). However, not all of these initial favorable locations grow a flower; some of these clouds dissipate early and do not reform. Both the condensation rate and the latent heating appear to be distinguishing factors in determining whether the flower will grow or decay, which stems from both of these terms being functions of both q_c and w.

Plotting a snapshot of the advection terms as shown in figure 2.8 reveals how these different terms contribute to the circulation. For flowers, we see that cloud-top advection is pushing q_c and n_c outward from the central updraft, while accumulating along the boundaries. The central region of the flower is where the cloud reaches the boundary layer inversion, while the surrounding areas are cloud-free. These terms, particularly the q_c advection, have the strongest oscillation in strength and act to balance the vertical cloud growth with the horizontal motions. This pulsing of the internal dynamics of the cloud is similar to what is seen in other LES runs of shallow cumulus, where changes in the buoyancy are balanced by horizontal convergence (Heus et al. 2009). Because we previously noted that our flowers are much smaller than what is typically observed in nature, the advection appears to be focused on balancing condensate convergence and not allowing the cloud to grow. The vertical velocity diffusion also pushes the strong updraft away from its center towards the cloud boundaries, although we previously showed that this term was not as critical to flower formation. The virga advection terms are randomly dispersed over the cross-section, are small compared to the other terms, and were shown in figure 2.6 to not impact cloud formation, and are thus not considered in the circulation.

For gravel, clouds form from the initial conditions along the boundaries of relatively clear areas. We can see this transition in the difference between figures 2.3 and 2.4 with the cloud arcs forming to outline the initial relatively clear spaces. The primary changes from flowers to gravel were increasing the condensation rate, the advection strength, and the inversion depth. As mentioned previously, the increase in condensation likely aids in maintaining condensed cloud water in an environment of increased horizontal advection. This would also increase the latent heating, which has been shown to favor an open cellular structure when heating is present near the surface (Feingold et al. 2010). Furthermore, gravel requires more cloud water in the domain to form as initializing the model with sugar does not result in gravel formation whereas initializing with flowers does, despite the equivalent environmental conditions.

A cross-section of the advection terms shows that there are primarily only two forms of advection present within gravel clouds in this model: vertical velocity diffusion and q_c virga advection. Even though all forms of coupling were strengthened to create gravel in the model, the deeper boundary layer and lower q_c means that the clouds no longer reach the inversion height and so the cloud-top advection term does not have an influence here. The w diffusion, as previously shown, plays a major role in the formation of gravel in our model, as figure 2.8 shows this term with strong convergence at the cloud boundaries. The cloud is thus maintained via vertical motions propagating outward, both from within the cloud and outside. We also note that virga advection occurs everywhere except at the cloud boundaries. As the presence of virga advection indicates both neighboring precipitation and a net circulation towards that point, this would indicate that the cold pools originate along the cloud boundaries to induce the central updraft.

2.4 Summary and Conclusion

Previous studies have shown that simple cloud models can be used to reproduce some realistic characteristics of cloud fields. We offer another such model that tracks cloud water, rain water, and cloud drop number concentrations, mediated by the vertical velocity, to simulate shallow convection in warm tropical clouds. By coupling this model using the mesoscale circulations defined by w, our model can approximate several shallow cumulus patterns commonly seen in nature by simply varying the parameter regime, which describes the environment. To wit, the model can distinguish between sugar, the shallow and fine-scale cumulus with random dispersion and little precipitation; gravel, small cumulus with frequent precipitation organized around cold pools; and flowers, aggregations of cloud surrounded by clear air.

Compared to observations of real-world clouds, some aspects of our modeled clouds are realistic while others require continued work. Sugar is comparable in terms of cloud size distribution, cloud separation, and peak cloud water content, while gravel matches observations of large-scale feature size. All three patterns showed the expected domain organization as defined by I_{org}. Flowers are a more difficult case: while the I_{org} index shows clustering similar to that of observations and realistic values of q_c and w, clouds in the model are small with large clear spaces in between as compared to the larger quasi-stable flowers observed in nature. This suggests that the model misses essential physics for flower formation and evolution, either in the internal cloud processes or through the coupling. Currently only the cloud-top coupling term plays a significant role in flowers formation, which puts the onus on a single term to control both aggregation and expansion, when in reality these processes are the result of vertical circulations between the clouds and their environment. In addition, aggregation may be related to Ostwald ripening, wherein humid areas become more humid at the expense of drier areas becoming drier (Wood et al. 2002; Narenpitak et al. 2021), suggesting the need to explicitly track changes in the water vapor concentration to capture this effect.

We find that in addition to processes common to any cloud type, sugar is most strongly controlled by the balance between environmental buoyancy and gravitational drag of liquid water. These clouds are small and have relatively low condensate, preventing them from efficiently using strong latent heating or cold pool circulations to grow. There is also little interaction between each cloud and its neighbors, fitting with their random distribution across large domains. Gravel clouds fall in between the sizes of typical sugar and flowers and so have elements of both cloud types in their controlling processes. The distinguishing factor is that gravel is significantly impacted by the vertical velocity diffusion term, resulting in the expansion of updrafts into a more open cell type pattern. This model process most closely aligns to what we would see around cold pools, with the horizontally diffused updrafts in particular simulating the rising air at the leading edge of gust fronts. We note that the horizontal effects of cold pools are more important than the vertical effects in forming gravel. For flowers, the latent heating and cloud-top advection are the two processes that dominate when compared to other patterns. We know from prior literature that latent heat release is a major source of instability in deeper clouds (Tao and Li 2016), and our model shows that strong latent heating supplants the environmental instability in driving the vertical motions. The cloud-top advection is then responsible here for maintaining the cloud boundaries.

Future work is being done on this model to increase the size of flowers in line with what we observe in nature, with a focus on the method of coupling used to produce mesoscale circulations. This requires that we split the coupling into cloud top and cloud base processes, which we do by introducing an equation for water vapor concentration q_v. Preliminary results with this model are promising in terms of cloud organization, but additional work needs to be done to ensure that individual clouds are realistic. This work will be discussed in depth in the following chapter.

Chapter 3

A Reanalysis of Coupling Methods in a Simple Cloud Model for Producing Cloud-Scale Circulations

3.1 Introduction

The self-organization of shallow cumulus into distinct patterns affects the Earth's radiation budget and provides a significant source of uncertainty in climate models, a topic of ongoing interest as our climate continues to evolve (Benner and Curry 1998; Bony and Dufresne 2005; Kazil et al. 2024). Stevens et al identified four such patterns, colloquially termed sugar, gravel, flowers, and fish, that frequently occur in the trade wind regions (Stevens et al. 2019). Sugar are small disorganized clouds not associated with precipitation, gravel are small clouds organized into arcs around cold pools, flowers are larger aggregations of cloud that clear out their surroundings, and fish have a skeletal-like structure of clouds and clear air organized along a line (Stevens et al. 2019). These patterns are linked to different environmental conditions, with the smaller sugar and gravel being associated with higher sea surface temperatures and lower stability while the more organized gravel and flowers occur more often in stronger surface winds (Bony et al. 2020). Many of these organized patterns are associated with the presence of shallow mesoscale circulations, controlled by the spatial variance in vertical velocity on a scale too small to be captured by climate models (George et al. 2023; Vogel et al. 2022).

Simple cloud models are one tool to help us understand the processes behind shallow cumulus pattern formation, and by coupling cloud box models across a grid they can be used to recreate these mesoscale circulations (Rosemeier and Spichtinger 2020; Feingold and Koren 2013). We presented one such coupled model in the previous chapter to simulate sugar, gravel, and flowers (fish, associated with large-scale features such as frontal passages, were not considered). While this model was able to acceptably produce sugar and gravel, the lack of a vertical coordinate hindered definable circulations from being resolved and did not allow flowers to grow to a realistic horizontal size, which in the real atmosphere can be up to 100km or more (Dauhut et al. 2023). Our main motivation is to investigate if we can modify the simple model to one which can produce more realistic flowers, while keeping its ability to generate realistic sugar and gravel clouds.

Several LES studies have been able to reproduce the formation of a flower using observational data from the Elucidate the Couplings Between Clouds, Convection, and Circulation (EUREC^{4}A) campaign (Narenpitak et al. 2021; Dauhut et al. 2023; Saffin et al. 2023). In all studies, flowers developed in response to the mesoscale vertical velocities converging moisture, making the moist patches moister and the dry areas drier (Saffin et al. 2023). Narenpitak et al found that transition to larger cloud aggregates was the result of the vertical advection of mesoscale total water content, dependent on the vertical gradient of moisture concentration (Narenpitak et al. 2021). Differences in vertical profiles of water vapor and cloud then suggest that this advection transports different forms of water at different levels, as cloud water concentrations are highest at cloud top while total water concentrations increase towards the surface (Bretherton and Blossey 2017). In addition cold pools were observed to form with flowers, which while they do not appear to initiate the aggregation, they may play a part in the later organization of a flower into a more circular structure as the cloudy updrafts preferentially move to the outside edge of the cold pool (Narenpitak et al. 2021; Dauhut et al. 2023).

These studies point to the need to both be able to simulate advection over the vertical profile of an updraft, as well as track atmospheric moisture throughout its life cycle in and around a cloud as it is aggregated by the circulation. For a vertically-averaged simple model, this implies coupling referencing different levels. Here we present a simple warm cloud model building upon the work presented in chapter 2 that models circulations of total water more explicitly in order to grow flowers to a more realistic size and discusses how such circulations function to aggregate moisture.

This chapter is organized as follows. The next section discusses the cloud box model equations and, specifically, their coupling terms. Section 3.3 discusses model results and compares them to observed cloud patterns. We then study the importance of the different terms in the equations so as to understand the minimal equation set for each cloud type. Section 3.4 provides a summary and concludes the chapter.

3.2 Methodology

3.2.1 Model Development

This model follows the same general structure as the one discussed in chapter 2, using a system of four nonlinear differential equations to define the evolution of a cloud over time. In that chapter, we used evolution equations for cloud water concentration q_c, rain water concentration q_r, cloud drop number concentration n_c, and vertical velocity w. In this chapter, most of the processes affecting cloud water concentration q_c, rain water concentration q_r, and vertical velocity w remain very similar. The equation for cloud drop number concentration n_c, found to have little utility in distinguishing the different patterns in the previous model, has been replaced with an equation describing the evolution of water vapor concentration q_v. This allows us to track variations in total water in a warm cloud system throughout its entire life cycle, as our previous assumption that a tropical environment has sufficient water vapor available to form cloud at any time was perhaps less than realistic. This updated model is defined in equations 3.1-3.4 and summarized in table 3.1. Values of q_c, q_r, and q_v are restricted to positive values, whereas w can be both positive or negative. The non-dimensionalization of the model is described in appendix B.

$$\frac{dq_v}{dt} = Sw + 0.01d_8q_r - d_5w(h_{v,1}q_v + h_{v,2}q_c) + E|w| + c_{q_v} \tag{3.1}$$

$$\frac{dq_c}{dt} = d_5w(h_{v,1}q_v + h_{v,2}q_c) - d_6q_c^2 - d_7q_cq_r - E|w| + d_{10}h_{v,2}w + c_{q_c} \tag{3.2}$$

$$\frac{dq_r}{dt} = d_6 q_c^2 + d_7 q_c q_r - d_8 q_r + P \tag{3.3}$$

$$\frac{dw}{dt} = -\epsilon_w \frac{w^2}{H} - \frac{g}{\rho}(q_c + q_r) + f_w + \frac{d_3 d_5}{\rho} w|w| q_v - \frac{d_4}{\rho} q_r - d_p w^3 + 0.61 \frac{g}{\rho} q_v^{'} + c_w \tag{3.4}$$

The evolution of q_v is controlled by four internal processes and one method of coupling. The primary sources of q_v in this model are evaporation from the warm ocean surface, parameterized in equation 3.1 as Sw, and entrainment parameterized as $E|w|$. Here S is a constant representing the relationship between water vapor evaporation efficiency and sea surface temperature, which follows a generally linear relationship over the warm ocean surfaces of the tropics (Stephens 1990). The vertical velocity w is a proxy for the strength of the mesoscale circulation and thus the horizontal wind, whereby higher wind speed allows for increased evaporation through both turbulent agitation of the ocean surface creating more evaporational surface area and transport of the moisture away from its source (either towards or away from the cloud, depending on the circulation direction) creating a q_v gradient (Birouk and Gokalp 2006). Entrainment also follows the mesoscale circulation strength (regardless of the direction) which affects the amount of mixing at cloud top, as both entrainment and detrainment have been shown to correlate with w (Savre 2022). The entrainment term is equal and opposite to that in the q_c equation as the entraining of dry environmental air at cloud top results in evaporation of q_c.

Whereas the previous model parameterized the condensation as a function of already present cloud water on which to condense vapor, the inclusion of spatiotemporal variations in q_v in equation 3.1 allows us here to explicitly model the condensation instead as a function of the exchange between water vapor and cloud water. Including w in this term is a proxy for adiabatic temperature changes with cooling (warming) air in an updraft (downdraft) resulting in increased condensation (evaporation). Here the step function h_v denotes the different source of moisture in condensation versus evaporation and is defined as $h_{v,1} = 1;\ h_{v,2} = 0$ for $w \geq 0$ and $h_{v,1} = 0;\ h_{v,2} = 1$ for $w < 0$. This ensures that condensation is a function of available water vapor, whereas evaporation is a function of available cloud water. The condensation efficiency parameter d_5 encompasses the other controls on condensation rate that cannot be directly or indirectly inferred from our four variables, such as supersaturation. Condensation is equal and opposite between q_v and q_c in the same manner as autoconversion and accretion between q_c and q_r, as well as being included in the latent heating term affecting w.

The fourth internal process controlling q_v is a source from evaporating virga below cloud. This process assumes that in the presence of precipitation ($d_8 q_r$), a percentage of that rain water will evaporate and moisten the sub-cloud region to be available to be ingested back into the cloud. While this term acts opposite to the precipitation term affecting q_r, it is scaled for q_v to represent the majority of rain water being removed from the system with only a small portion being converted to and retained as water vapor.

Equation 3.2 for q_c contains terms for autoconversion and accretion, that is, the combining of two cloud drops or a cloud drop and rain drop, respectively, as a simple nonlinear combination of the two (Khairoutdinov and Kogan 2000; Spassova and Nikolov 2005). We also include a term for subsidence parameterized as $d_{10} h_{v,2} w$ which represents the presence of a subsiding shell in the downdrafts surrounding the cloud and works to enhance evaporation in this area and suppress cloud formation (Heus and Jonker 2008). This term is only active in the presence of downdrafts. The vertical velocity equation 3.4 follows that described by Tao et al with one primary change to the previous model (Tao and Li 2016). Here we can explicitly include the water vapor buoyancy force calculated using the deviation of q_v from the domain-mean at each time step, as $q_v^{'} = q_v - q_v^{mean}$.

3.2.2 Model Coupling

Equations 3.1-3.4 are coupled together across a 2D grid through four processes that characterize the horizontal mixing affecting w, q_c, and q_v as shown in figure 3.1. The vertical velocity is coupled

Table 3.1: Summary of model terms and tuneable parameters in equations 3.1-3.4.

Model Term	Physical Meaning	Associated Parameter	Units
$d_5 w(h_{v,1}q_v + h_{v,2}q_c)$	Condensation	d_5: Cond efficiency	$1/m$
$d_6 q_c^2$	q_c Autoconversion	d_6: Autoconversion rate	$m^3/kg\ s$
$d_7 q_c q_r$	q_c Accretion	d_7: Accretion rate	$m^3/kg\ s$
$E\lvert w\rvert$	Entrainment	E: Entrainment rate	kg/m^4
$d_{10} h_{v,2} w$	Subsidence	d_{10}: Subsidence rate	kg/m^4
$d_8 q_r$	Precip depletion	d_8: Precipitation rate	$1/s$
P	Precip influx	-	$kg/m^3\ s$
Sw	q_v Env source	S: Evaporation rate	kg/m^4
$-\epsilon_w \frac{w^2}{H}$	Vertical w advection	H: Average cloud depth	m
$\frac{g}{\rho}(q_c + q_r)$	Gravity drag	ρ: Average air density g: Gravity	kg/m^3 m/s^2
f_w	Instability	f_w: Buoyancy	m/s^2
$\frac{d_3 d_5}{\rho} w\lvert w\rvert q_v$	Latent heating	d_3: Latent heating strength	$unitless$
$\frac{d_4}{\rho} q_r$	Cold pools	d_4: Cold pool subsidence	m/s^2
$d_p w^3$	Damping	d_p: Turb diffusion rate	s/m^2
$0.61 \frac{g}{\rho} q_v^{'}$	Water vapor buoyancy	-	-
c_w	w advection	γ_1: Turb mixing strength γ_2: Cold pool circ strength	$1/s$ $m^4/kg\ s$
c_{q_v}	Cloud-base coupling	γ_3: Subcloud mixing strength	$1/m$
c_{q_c}	Cloud-top coupling	γ_4: Inversion strength	$1/m$

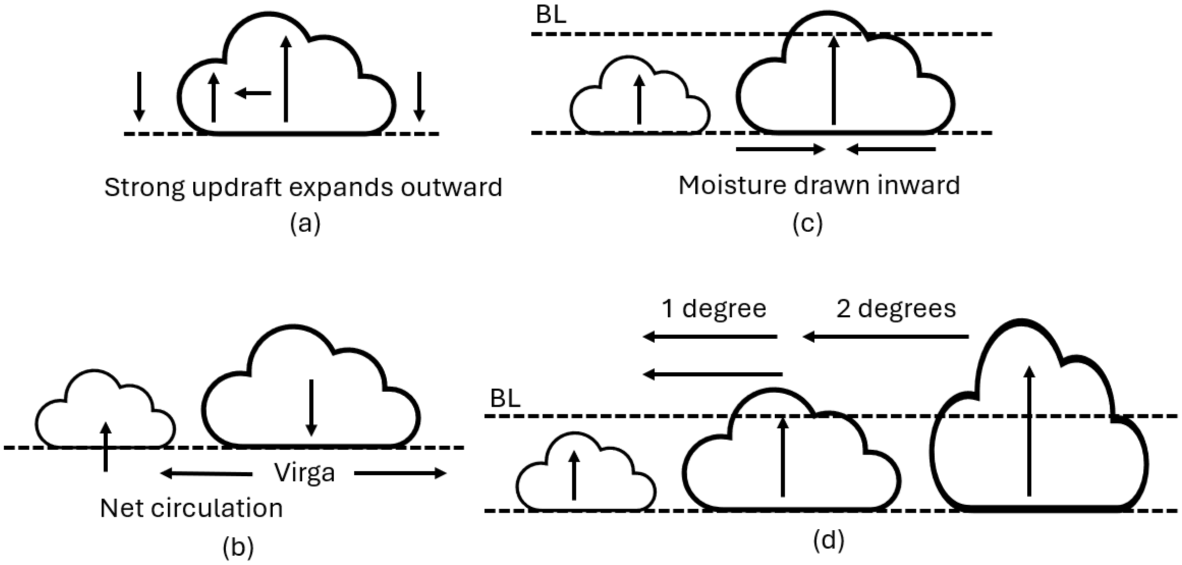

Figure 3.1: The four coupling methods used in the model to horizontally advect the (a,b) vertical velocity, (c) water vapor, and (d) cloud water.

in two ways: via horizontal diffusion of w through subgrid-scale turbulent processes and cold pool-induced circulations. Water vapor is coupled through circulations at cloud base while cloud water is advected at cloud top when interacting with the boundary layer inversion, reflecting the vertical moisture profile of vapor versus liquid water (Narenpitak et al. 2021).

Specifically,

$$c_w = \frac{1}{8}\gamma_1 \sum_{i=1}^{8} (j_i w_i) + \gamma_2 \sum_{i=1}^{8} (j_i max(q_{ri} - q_{r0})) \tag{3.5}$$

in which the first term in equation 3.5 calculates the weighted average vertical velocity of the surrounding grid boxes as those vertical motions expand horizontally, with the subscript i referring to each immediately neighboring grid point. j_i is a weighting factor based on distance, with grid boxes on the diagonals being further away than those grid boxes immediately to the left or right and thus weighted by a factor of $1/2$. The second term calculates the precipitation differential between grid boxes. Boxes with higher rain water concentrations, and thus more precipitation, result in stronger cold pools which then induce updrafts in their more weakly precipitating neighbors. Both processes are further controlled by coupling weights γ_1 and γ_2 with units of $1/s$ and $m^4/kg\ s$, respectively, representing the strength of horizontal mixing in the environment.

The coupling term at cloud base in the q_v equation reads:

$$c_{q_v} = \frac{1}{8}\gamma_3 \sum_{i=1}^{8} (j_i max(w - w_i, 0) q_{v,i} + j_i min(w - w_i, 0) q_v) \tag{3.6}$$

Circulation of moisture through the cloud is split into two processes: water vapor advected at cloud base and cloud water advected at cloud top. The advection at cloud base in equation 3.6 is a function of the circulation strength as defined by the vertical velocity differential. The direction of circulation as identified by the max and min functions determines the source of q_v

being advected: either drawn inward from a neighboring cloud or pushed outward from the central cloud. The strength of this process is modulated by the coupling weight γ_3 in m^{-1} as a function of the distance over which the turbulent mixing acts.

Coupling at cloud top in the q_c equation is generally modeled as

$$c_{q_c} = \gamma_4 \sum_{i=1}^{8} \frac{1}{n}(q_c - q_{c,i}) \tag{3.7}$$

and is a function of the depth of the boundary layer and the strength of the capping inversion, where clouds that try to grow past the inversion level are instead advected horizontally. We make the assumption that cloud water concentration grows linearly with height, allowing us to define a domain-wide amount of cloud water corresponding to the inversion height (Nicholls 1989). q_c that exceeds this defined value is then advected horizontally, whereas q_c below the threshold represents a cloud growing and decaying vertically. In equation 3.7, q_c will advect when $q_c > q_{c,i}$ and $q_{c,i}$ is below the inversion threshold. The value of n equals the number of advecting pairs at that grid point. The coupling weight γ_4 characterizes the inversion strength with larger values equating to more horizontal advection.

It is of interest to us whether the distance over which the grid points are coupled affect the size of the clouds, particularly with flowers. Therefore, cloud top transport follows a two-step process. In the first scenario of two neighboring grid boxes where one cloud reaches the inversion and one does not, then a percentage of the excess q_c is pushed from the former to the latter in accordance with equation 3.7. We refer to this as one degree of coupling. If two neighboring clouds both reach the inversion in this scenario or if neither do, then no advection will occur between these grid points. Here the clouds either have no available room to allow advection or are not yet developed enough to advect horizontally. In the second scenario, if two neighboring clouds both reach the inversion height, then the box with the higher q_c can push the condensate past that immediate neighbor and into any neighbor's neighbors below the inversion. We term this two degrees of coupling. Here excess condensate continues to advect horizontally until space is available. Both scenarios of cloud-top coupling are depicted in figure 3.1d. Results in the following section use two degrees of coupling except where specifically stated.

3.3 Results

Eight different sets of initial conditions representing shallow cumulus of different size are used to initialize the model and are shown in figure 3.2. Five scenes use cloud mask data from MODIS imagery from 9 Feb 2017 in the tradewind region NE of Barbados. Different locations from within this satellite image were selected, then converted into a range of realistic q_c values with peak q_c within each cloud following the relation $q_c \approx \alpha A_r^\beta$, where A_r is the cloud area, $\beta = 0.3$, and $\alpha = 60 \times 10^{-6}$ (Feingold et al. 2017; Koren and Feingold 2011; Chiu et al. 2021). Additionally, because shallow tropical cumulus are known to follow a power law distribution in regards to size, another three cloud fields were randomly generated with the number concentration of cloud diameter obeying this relationship (Benner and Curry 1998; Feingold et al. 2017). The fields of w, q_v, and q_r were initialized with a random distribution within physical constraints to represent clouds in different stages of their life cycles. These eight total initial cloud fields are then used in conjunction with different parameter settings representing the environmental conditions to statistically analyze the resulting patterns as compared to observations.

There are three groups of model settings that control the cloud output: the initial conditions, the internal parameter settings that produce clouds, and the coupling parameters that organize these clouds into patterns. For this model we find that sugar forms in an initial environment of higher water vapor content as compared to flowers and gravel, but evolves over time to contain less water vapor. The parameter settings for sugar show a more unstable environment with higher rates of condensation but less precipitation and very weak coupling, consistent with observed environments and sugar's definition as having little to no precipitation (Stevens et al. 2019; Bony et al.

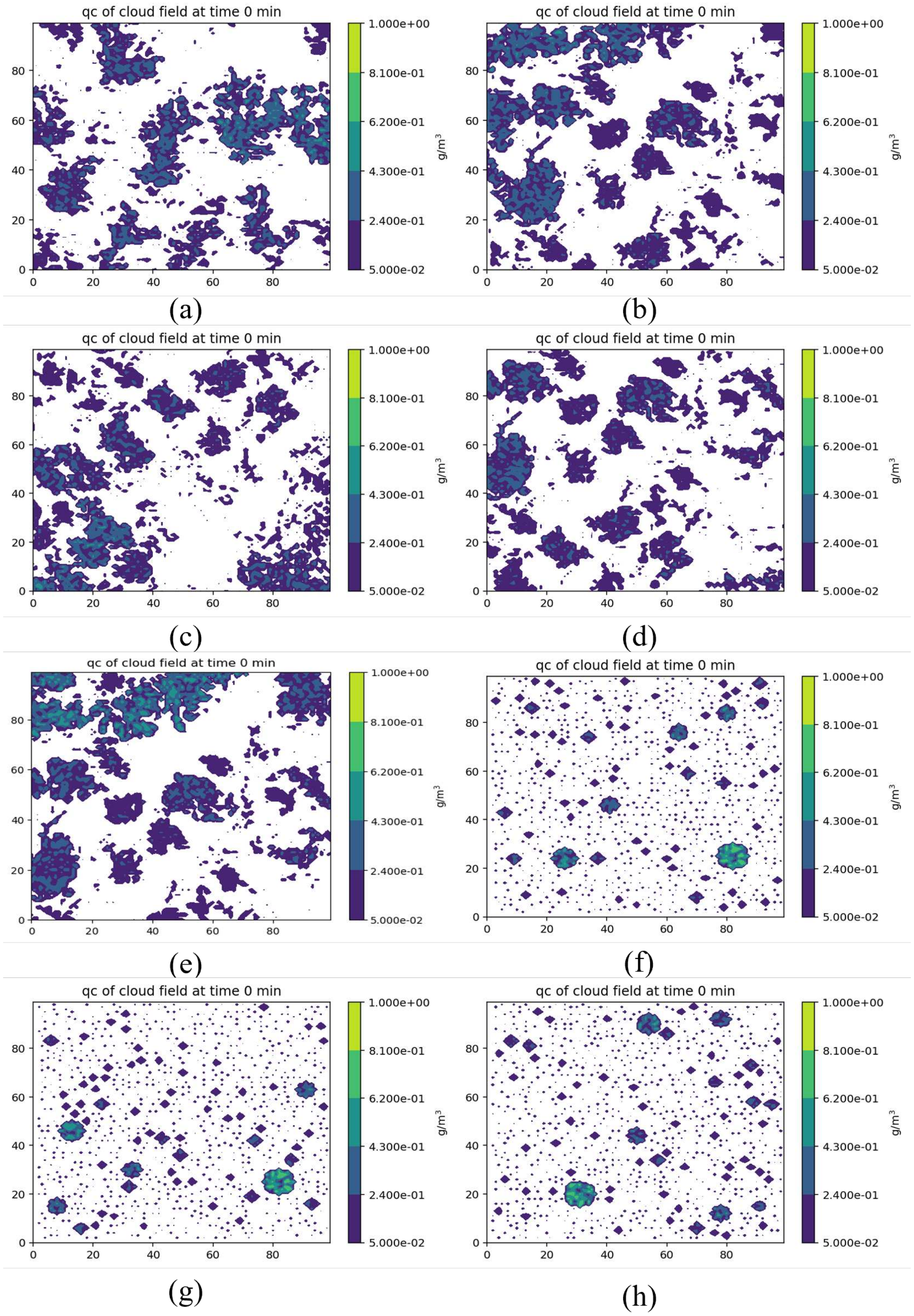

(a) (b) (c) (d) (e) (f) (g) (h)

Figure 3.2: Initial conditions for the simple model. Images a-e are taken from MODIS 1km imagery on 9 Feb 2017 at five different locations in the tradewind region NE of Barbados (NASA 2024). Images f-h are randomly-generated sugar fields following a power law size distribution.

2020). Flowers occurred in the presence of strong coupling through q_v and q_c showing pronounced mesoscale circulations combined with a more stable but deeper boundary layer and stronger latent heating rates, again matching with observations (Narenpitak et al. 2021). Gravel required strong coupling through the vertical velocity with a deep inversion layer and pronounced precipitation effects, fitting with their association with cold pool structures (Stevens et al. 2019). Additionally, the environment surrounding gravel was initially varied over time as the pattern stabilized, with stronger condensation and cold pools and weaker w diffusion at the beginning of the model run. Sea surface temperature, represented by the evaporation rate S, was lower for sugar than for flowers and gravel, the reverse of that found by Bony et al but in line with model results from Narenpitak et al (Bony et al. 2020; Narenpitak et al. 2021).

3.3.1 Evolution of Sugar

Our model generates sugar, seen in the middle column of figure 3.3, following a spin-up time of roughly 30 minutes with the cloud locations staying relatively consistent in the absence of a background wind flow. These small clouds have an irregular shape with q_c in the range of $0.05 - 0.2\ g/m^3$, matching with results found in both observation (Chiu et al. 2021) and modeling studies (Bretherton and Blossey 2017). q_v falls around $0.5 - 1\ g/m^3$, which is at the lower end of observed tropical water vapor content but not unrealistic for small sugar clouds (Mascaut et al. 2022). w is around $\pm 0.5\ m/s$ across the domain and q_r is below the threshold for observable precipitation (Kitchen and Caughey 1981; Chiu et al. 2021).

Figure 3.4 shows the distribution of cloud sizes throughout the domain divided into bins of width 0.5km after the pattern has formed and averaged over the 8 runs. This distribution is compared to observations of sugar from the tropical Atlantic in Jan 2017, taken from MODIS imagery over 19 different days when sugar was identifiable. We can see that the model follows the observed distribution quite well for the smallest cloud sizes up to 4km in diameter, which are the most representative of the typical size of sugar (Bony et al. 2020). Both observations and model also show an exponential decrease in number of clouds per cloud diameter bin, a relationship well-

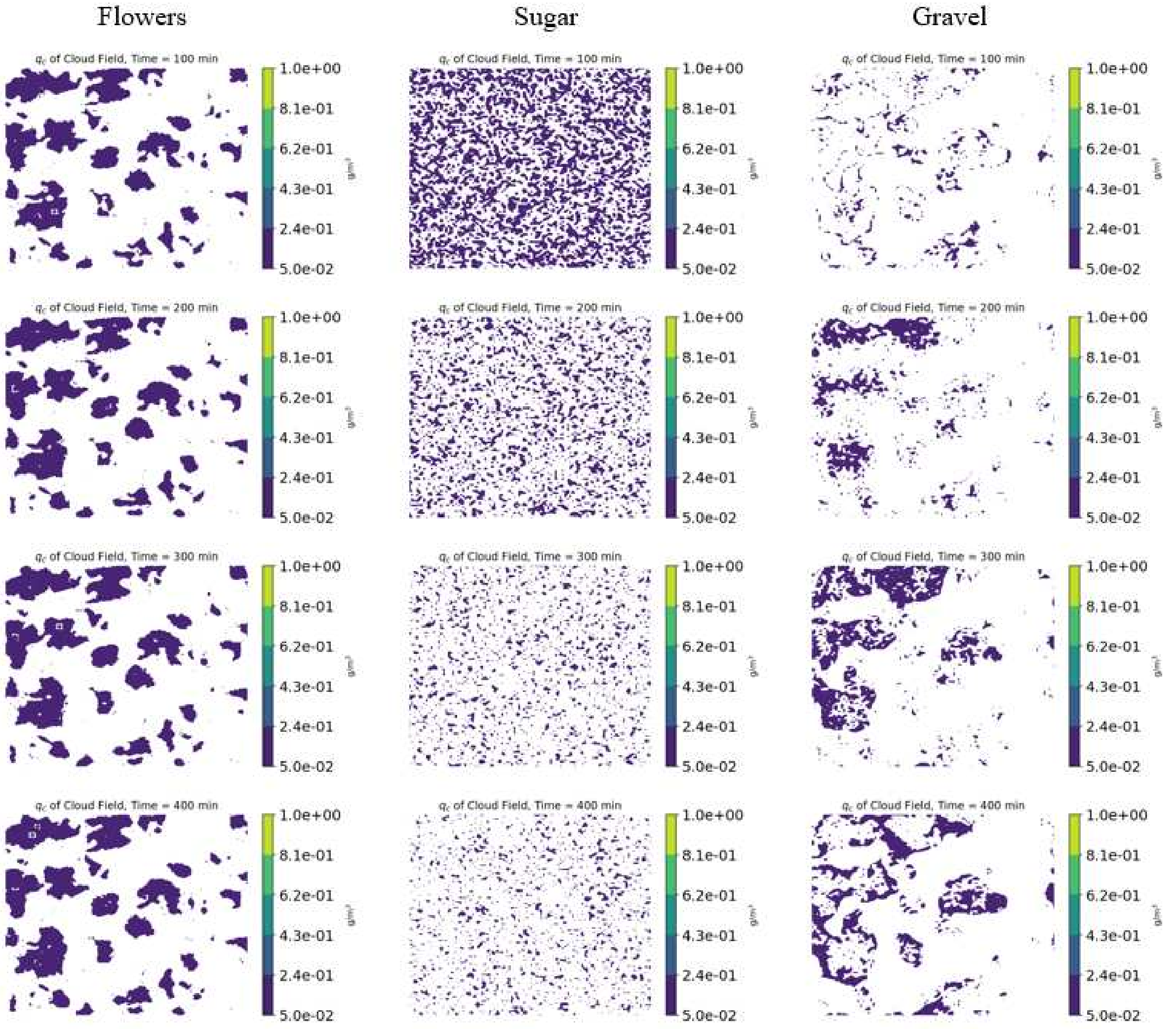

Figure 3.3: Representative model output over time for flowers (left), sugar (middle), and gravel (right) using initial conditions from figure 3.2(b). Model output for all 8 sets of initial conditions is shown in appendix B.

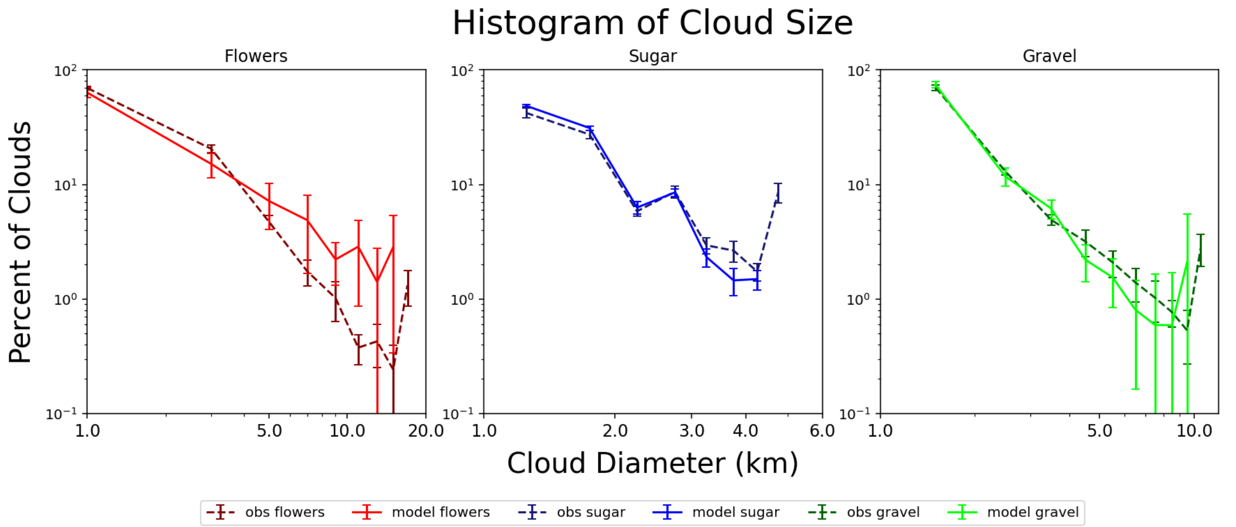

Figure 3.4: Histograms of cloud diameter for model output (solid lines) vs observations (dashed lines). Observed cloud fields are taken using MODIS imagery from Jan 2017 and manually classified into patterns. Sugar bin widths are 0.5km, gravel bin widths are 1km, and flower bin widths are 2km. The final observed bin encompasses all cloud sizes larger than the model clouds. Error bars show one standard error from the mean.

quantified over the decades (Benner and Curry 1998; Feingold et al. 2017). The model does not produce the largest cloud sizes that we see in the atmosphere, however we also argue that these larger observed clouds may be more of a result of our measurement technique and are not actually sugar. Stevens et al notes that sugar is unlikely to be present over a large area, therefore there is a high probability that any image of sugar will have some contamination from other clouds that are not sugar (Stevens et al. 2019). Indeed, this is the case for measuring any pattern, as we will note with flowers and gravel later on.

Figure 3.5 shows the impact on the average cloud diameter and cloud number from removing individual processes from the model. Significant deviations from the control run here indicate that either clouds did not form or significantly changed size as a result of removing each given term. The processes required for model stability across all three patterns are the condensation and precipitation terms; these processes are the dominant sinks for q_v and q_r, respectively, and ensure that these variables do not grow out of control. This result is the same as that found for our previous model and indeed is necessary in any predator-prey-type model (Wacker 1995). In addition, the

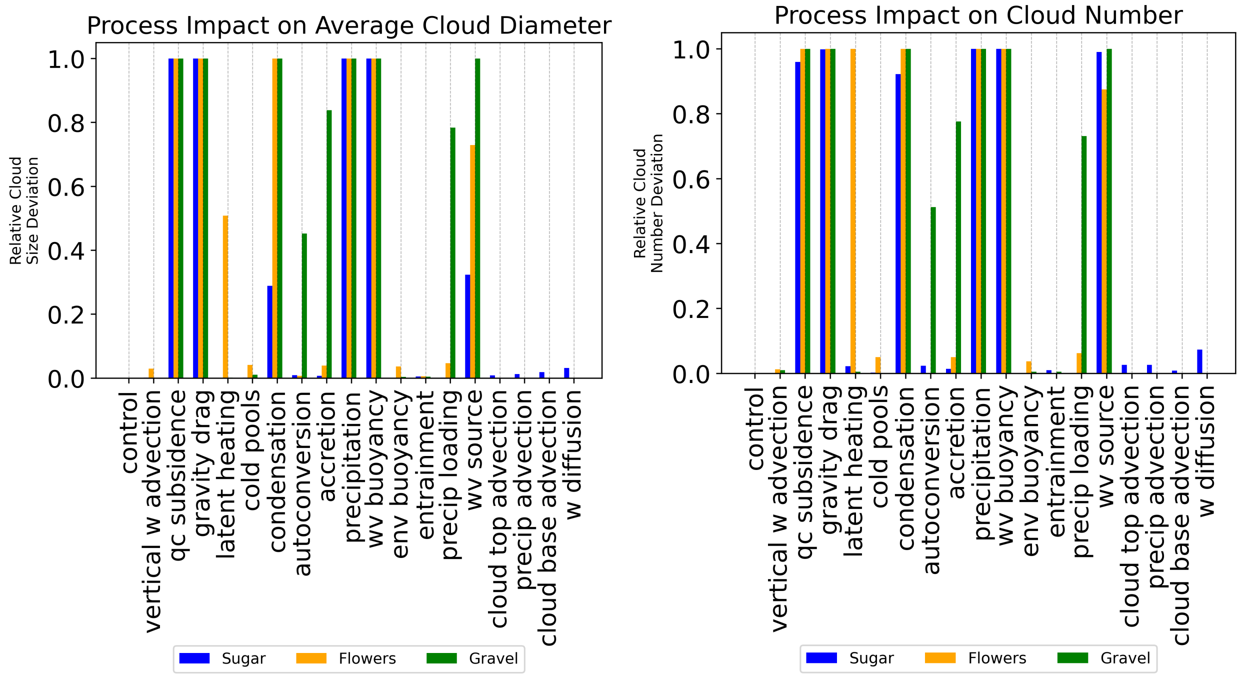

(a) (b)

Figure 3.5: Changes in average cloud diameter (top) and cloud number (bottom) when removing one process as compared to the control run in figure 3.3b.

water vapor buoyancy and gravitational drag on w, an oceanic source of water vapor for q_v, and cloud-edge subsidence for q_c were all critical in forming sugar. Water vapor uptake from the ocean is straightforward to understand as the primary source of q_v without which the small sugar cannot maintain its size in the presence of even weak advection. Ambient water vapor in the subcloud layer is quickly depleted without replenishment from the sea surface. The loss of q_c subsidence resulted in a significant increase in q_c across the domain, as this term suppresses cloud formation in the drier downdrafts in the environment. Meanwhile the presence of water vapor provides a source of positive buoyancy inducing cloud formation, as the loss of this term resulted in significantly fewer clouds forming through the domain. The remaining terms, while having a slight impact on cloud size and cloud number, do not appear to drive or preclude the clouds from organizing into recognizable sugar.

3.3.2 Evolution of Flowers

Flowers in figure 3.3 in the left column are formed with a spin-up time of also around 30 minutes and remain relatively consistent in location while growing slowly over time. The larger clusters of flowers range from circular to elongated with an average effective diameter between 5-16km. This is at the smaller end of the range of flower sizes that we see in observations, which from the fields in figure 3.2 have an effective diameter up to 26km while other observational and modeling studies have shown them capable of being even larger (Bony et al. 2020; Narenpitak et al. 2021). The size of the resulting flowers appears to be dependent upon the initial cloud field, as flowers formed from a field of sugar were smaller than those that formed from initially larger clouds, although similar in shape and relative void size between initial conditions. q_c ranges between $0.2 - 0.4\ g/m^3$, a reasonable range for shallow cumulus, and has much more temporal variation compared to sugar (Chiu et al. 2021). q_v in cloud falls around $0.1\ g/m^3$, which is quite low for the deeper flowers as it appears that q_v is being immediately condensed (Mascaut et al. 2022). Updrafts in cloud are around $2\ m/s$ with a domain-mean weak negative w outside of cloud. Precipitation remains weak with flowers, but is up to an order of magnitude higher than that seen in sugar.

If we look at these clouds with respect to their size distribution in figure 3.4, we can see that the number of observed clouds drops off more steeply with size compared to our modeled clouds, indicating that the model tends to produce an even number of clusters across these middle sizes throughout the domain. Both observed and modeled fields still contain primarily small clouds of diameter 1-5km. With the model these small clouds are found predominantly along the cloud boundaries as the edges mix with the environment and break apart the clusters, while the observations show these clouds scattered throughout the domain and are not actually flowers but rather sugar that is contaminating the picture.

Compared to sugar, flowers in this model form primarily as a result of increasing the coupling strength at both cloud top and cloud base, as well as from the w diffusion. This aligns with the presence of shallow mesoscale circulations that we see in multiple observation campaigns and modeling studies surrounding larger cloud aggregates (Bretherton and Blossey 2017; Dauhut et al. 2023; George et al. 2023). The impact of different processes on cloud size shown in figure 3.5 identify which terms are critical here for the model to form flowers. As previously discussed, both condensation and precipitation are necessary for model stability in forming any clouds. The q_c subsidence, gravitational drag, water vapor buoyancy, and water vapor source terms are all also critical terms in forming distinct flowers, with effects similar to that seen in forming sugar. Flowers were also impacted by the latent heating, as removing this term weakened the updrafts and served to break up the clouds.

None of the coupling terms had an individual impact on the formation of flowers despite the required increase in coupling strength, which implies that these terms act in concert to aggregate condensate. We therefore reran the model eliminating every unique combination of the coupling processes shown in figure 3.1 and assessed the resulting patterns. In doing so we find that the coupling of w through diffusion controls cloud aggregation whereas the coupling of q_c and q_v at cloud top and cloud base, respectively, controls the separation of clouds into individual elements. In the absence of w diffusion, clouds only coupled through advection at either cloud base or cloud top resulted in sugar, either regularly or irregularly distributed throughout the domain, while including both q_v and q_c coupling terms dissipated these small clouds completely. On the other hand, only coupling the model via w diffusion resulted in a field best described as stratocumulus as the clouds expanded unhindered. By adding either cloud top or cloud base coupling we start to see the individual flower clusters return as the advection of condensate separates off smaller clouds that then dissipate. The model output as a function of the different coupling terms is shown in appendix B.

3.3.3 Evolution of Gravel

Gravel is generated in this model following an increase in the coupling of w and a decrease in q_v and q_c coupling in relation to flowers. Organization occurred after roughly 20 minutes with clouds exhibiting strong periodic behavior, forming in a central location before being quickly advected towards the boundaries to form the prototypical arcs. The resulting arcs are on average 5km wide but can extend almost 70km in length, fitting with Stevens et al identification of meso-β scale lines (Stevens et al. 2019). Cloud water is in the range of $0.1 - 0.7\ g/m^3$ while rain water is around $1e^{-5}\ g/m^3$, both falling within acceptable observed ranges (Chiu et al. 2021). Rain water concentration is at the low end of observations, similar to that seen in our modeled flowers, but also requires an increase in the precipitation parameters and therefore still in line with gravel's association with precipitation (Stevens et al. 2019). The water vapor field continues to be low around $0.1\ g/m^3$ for the same reasoning as with flowers. Updrafts are present up to $0.5\ m/s$ along the lines of the clouds with domain-mean downdrafts in the clear regions.

The size distribution of gravel in figure 3.4 calculates the frequency of cloud diameter using bin widths of 1km and distances measured over the arc width (as opposed to the much longer arc length). We can see that our modeled gravel again matches very well with the cloud size distribution seen in nature, although the model has a much larger variance at larger cloud sizes. Both fields still contain an abundance of small sugar, visible interspersed between the cloud arcs in figure 3.3. The two histograms agree most closely at the larger cloud sizes above 5km in diameter, which we noted as the average cloud width across the domain. Observed gravel ranges from very fine-scale lines comparable to sugar in size to thicker arcs with stronger cold pools (Stevens et al. 2019). The higher concentration of large clouds seen in both distributions reflects the growth of deeper clouds at the nexus of multiple cold pools inducing strong updrafts.

Like both sugar and flowers, gravel in this model is dependent on terms representing condensation, precipitation, q_c subsidence, water vapor buoyancy, gravitational drag, and a water vapor source. All six terms were necessary for model stability in the presence of stronger coupling through w, as removing these terms resulting in the cloud field dying or growing exponentially. Additionally, removing the autoconversion and accretion terms caused thicker arcs of clouds as less precipitation was formed and subsequently removed. Finally we see a similar to flowers in that the coupling terms did not have an impact on their own but rather acted in concert. Running the same coupling combinations showed that this pattern is dependent on the coupling of w through both diffusion and precipitation, as the clouds were too shallow to reach the inversion level while the weaker circulations advected less q_v.

3.3.4 Circulations in Flowers and Gravel

In order to better understand how the advection terms function within flowers and gravel, we look at the term temporal evolution at three different locations around a cloud shown in the red boxes in figure 3.6: 1. a point at the center of the flower or inside a gravel arc (blue line), 2. a point at the edge of the flower or along the gravel arc (orange line), and 3. a point completely outside the cloud (green line). Plots a-d show flowers and plots e-h show gravel. The peak q_c inside the flower remains high throughout the cloud's lifetime while q_c at the cloud edge is much more variable. Meanwhile q_c in gravel is highly oscillatory, growing first at point 1 then being advected towards point 2 and precipitating out. q_c outside of the cloud is small as expected.

The advection terms then paint a picture of how moisture and vertical velocity are being redistributed within the cloud, particularly within the stronger mesoscale circulation surrounding the flower. Plot (b) shows the cloud-top advection of q_c, which for point 1 for flowers is entirely negative throughout the model run. The flower grows q_c most strongly in this location through condensation and buoyancy (as the only internal sources), keeping the cloud deep enough that condensate is consistently pushed outwards towards the cloud edge. Point 2 at the edge of the flower uses q_c advection as a balancing act to regulate cloud size. The evolution of q_c appears to most closely follow the cloud top advection. Point 3 is far enough away from the cloud's edge that no q_c advection reaches that far. For gravel in plot (f), no q_c advection is occurring as the clouds are too shallow to reach the inversion layer.

The advection of q_v in (c) tells the opposite story to that in (b) and makes the shallow mesoscale circulations in flowers more clear. At cloud base the advection of q_v at point 1 in both cases is strongly positive, accumulating q_v at the center of the cloud from its immediate surroundings as a function of the spatial differences in w. Meanwhile q_v advection at point 2 at the edge of the

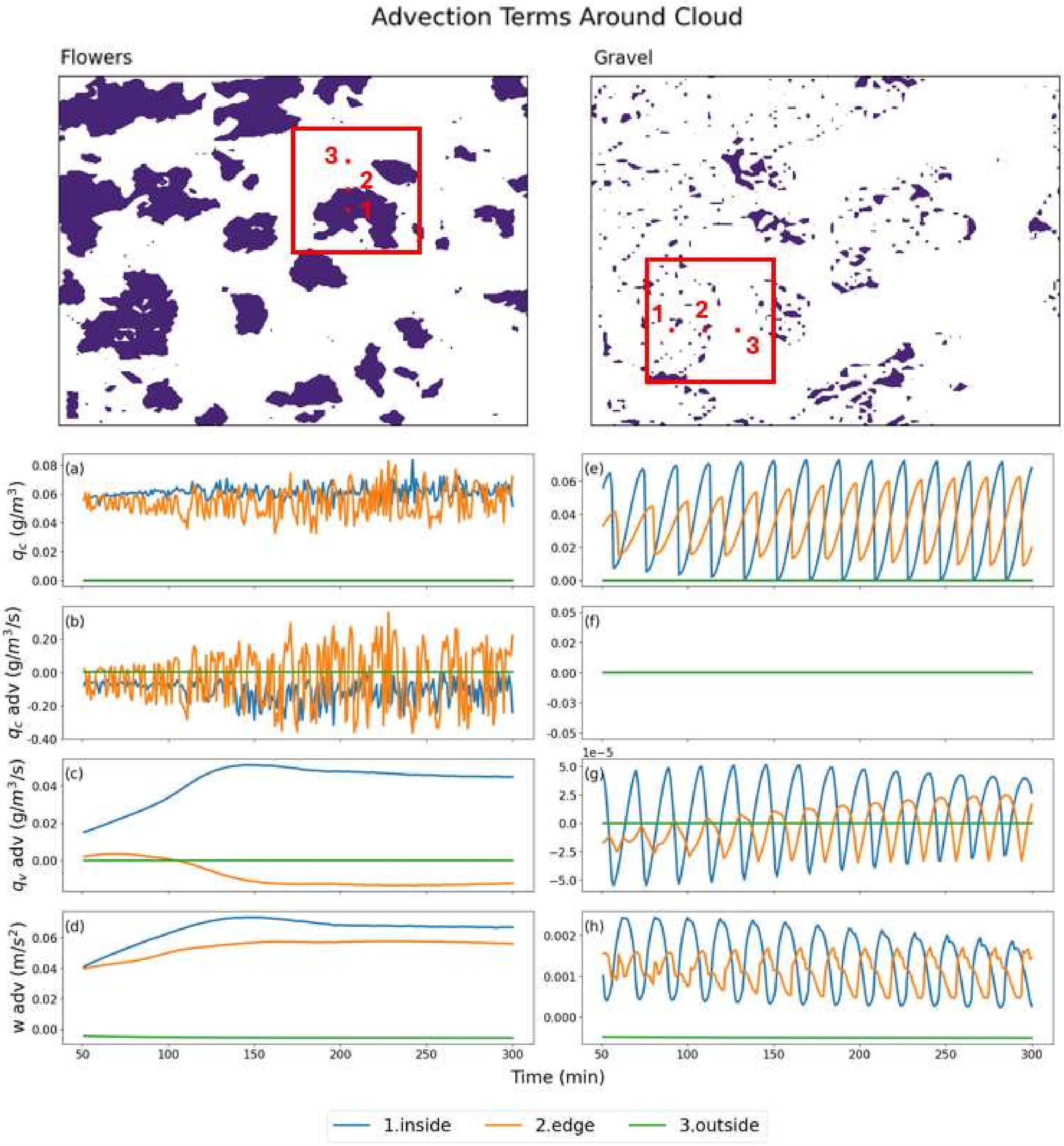

Figure 3.6: Evolution of flower (left) and gravel (right) cloud in figure 3.3 over time at three points (red dots): 1. inside the cloud, 2. at the edge of the growing cloud, and 3. outside the cloud. (a,e) shows changes in q_c, (b,f) shows the advection at cloud top, (c,g) the advection at cloud base, and (d,h) the advection of w.

cloud becomes negative as we reach the edge of the updraft. We note the lack of advection at point 3, indicating the circulation does not extend that far. Thus between these two advection terms we can ascertain the structure of our modeled cloud aggregates. Water vapor is drawn inward at cloud base, condenses and rises in the strong central updraft, then is pushed outward to a point where the advection and condensation are in balance. For gravel in plot (g) the q_v advection is in phase with changes in q_c but is also very small compared to other terms and therefore negligible.

w advection in (d) and (h) is primarily a function of the expansion of the updraft due to the precipitation effect being weaker. Both points 1 and 2 are most strongly affected by the expansion of surrounding updrafts, while point 3 is affected by both weak updrafts and downdrafts that average each other out. This term is the strongest of the three advection terms for gravel and follows the same oscillatory pattern between points 1 and 2 while also being 90 degrees out of phase with q_c, indicating that the w advection is leading the movement of clouds across the domain.

3.3.5 Impact of Coupling Distance

As discussed in the methodology, it is of interest to see whether or not the range of cloud-top coupling has an effect on the overall pattern, that is, does allowing q_c to advect beyond its immediate neighbors change the size of the resulting flowers? To investigate this, we ran the model with a set initial condition and parameter regime using both one and two degrees of coupling and plotted the resulting cloud field. Each corresponding cluster was assigned a number and the centroid location calculated, shown in figure 3.7.

On the whole, the centroid locations moved very little between the two images. The most prominent change is instead the minor breakup of clouds as the coupling distance increases. For example, we can see that the right side of cloud 9 splits off from the main body when given two degrees of coupling, or that cloud 6 breaks apart from one cloud into half a dozen smaller clouds. One small cloud at the top of the domain disappears altogether with the increase in coupling distance. Overall the edges of clouds become more ragged and broken at two degrees of coupling,

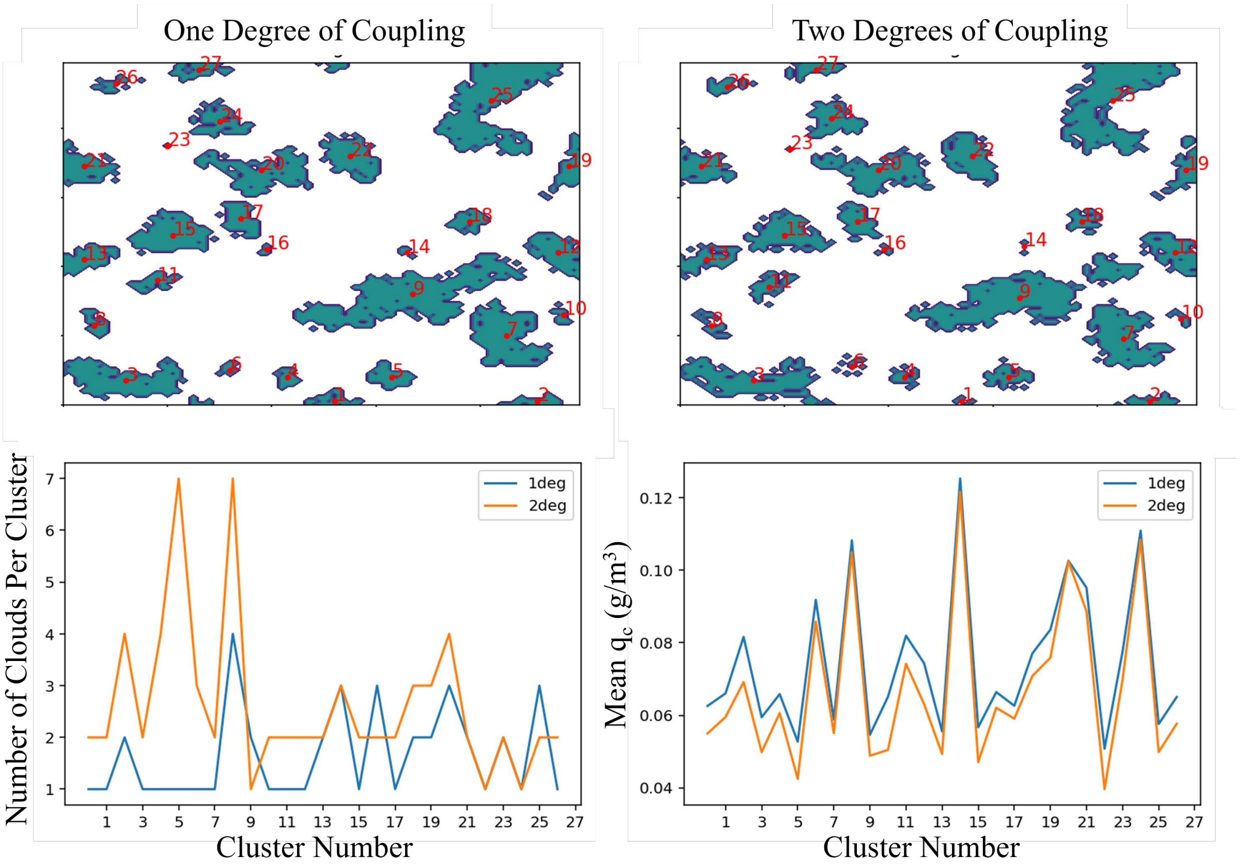

Figure 3.7: A comparison of flower size using one degree (top left) and two degrees (top right) of coupling. Clusters are equivalently defined by their position between the two images and labeled at their centroid. The bottom left plot shows the number of individual clouds in each cluster, while the bottom right plot shows the mean q_c per cluster.

compared with the almost smooth boundaries at one degree. This is more prominently illustrated by plotting the number of clouds contained within each cluster, which shows that clusters with two degrees of coupling are made up of more individual clouds than at one degree of coupling. In addition, the mean q_c is higher in almost every cluster at one degree of coupling vs two.

These changes tell us that increasing the cloud-top coupling distance, rather than increasing the cloud diameter as originally hypothesized, instead acts to average out the cloud at the boundaries. The increased loss of q_c over the larger coupling distance is not balanced by an increase in condensation at cloud center; rather the production of q_c appears to have a finite limit. Physically this averaging appears similar to an increase in lateral entrainment as dry air outside the cloud dilutes the cloud edges. Most importantly, we can conclude that coupling a simple model only with its immediate neighbors is sufficient to grow a flower across multiple grid points and that coupling across two (or more) degrees is likely not necessary to analyze the circulations.

3.3.6 Comparison of Models

By changing our simple model to track the entire life cycle of water within a warm shallow cumulus cloud and reevaluating how this moisture circulates in the atmosphere, we are able produce comparable patterns of sugar and gravel as well as more realistic-looking patterns of flowers. Figure 3.8 compares the results of our two models with MODIS observations: model A is our previous model described in chapter 2 using n_c and model B is our current model described here in chapter 3 using q_v.

In the top row, sugar clouds are on average smaller and more disconnected in model B than in model A. Both appear to be randomly distributed about the domain and have a number distribution that decreases with size similar to observations, but model A has more clustering that is larger than those sizes typically defined as sugar. q_c still oscillates in model B but not with the same amplitude as in model A. In terms of controlling processes, condensation and precipitation remain important between the two models in keeping the evolution stable. Meanwhile the buoyancy term,

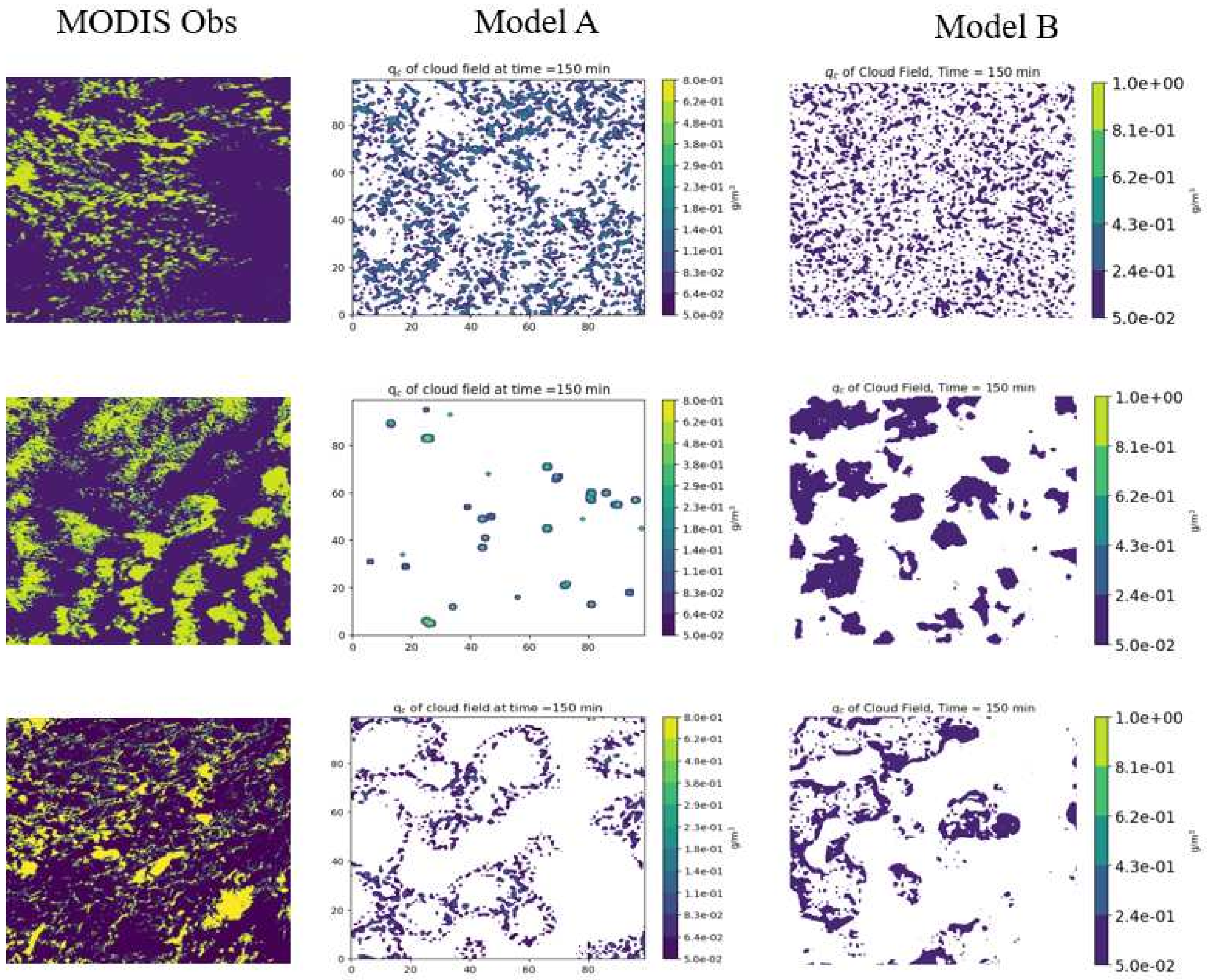

Figure 3.8: A comparison of patterns between MODIS observations (left), our first model using cloud drop number concentration from chapter 2 (center), and our current model using water vapor concentrations (right) for sugar (top row), flowers (middle row), and gravel (bottom row).

found to be critical in producing small clouds in model A, is split into environmental and water vapor-induced buoyancy in model B with the latter found to be the controlling process between the two.

The most striking difference between the models is in the size of the flowers, which go from circular point clouds at most several kilometers across in model A to sizes and shapes in model B that more closely resemble those observed. The distribution of cloud sizes in model B also more closely matches the observations, showcasing a range of cloud sizes with number inversely proportional to diameter in comparison to the single size clouds of model A. While circulations were present in both models around the flowers, model A was unable to expand these circulations past more than two points, whereas model B exhibits circulations over 20km wide spanning the entire width of flowers. This may reflect the necessity for the manner in which model B is coupled, specifically in splitting the coupling into cloud base and cloud top processes. Model A was unable represent this using only the single variable of q_c as the two processes canceled each other. We therefore conclude that the horizontal interactions of both q_c and q_v are necessary for a simple model to properly produce shallow mesoscale circulations of a more realistic size. The controlling terms between the two models are largely similar, with model B showing a stronger interdependence of the coupling terms on the development of flowers compared to model A's reliance on the cloud-top coupling only.

The differences in gravel between models A and B is in the width of the cloud arcs and the persistence of the pattern. Model A forms gravel after a long spin-up time which while initially close to the size and shape of observed gravel, then decays through the remainder of the model run into a few thin, broken lines. Model B meanwhile produces clouds that oscillate between flowers and gravel, forming central clouds that decay and push condensate towards the edges into arcs. Both models match the observed size distribution at different points in the cloud life cycles, particularly for smaller cloud elements less than 5km in width. Of the critical terms we again see similarities between the two models the same as previously described surrounding condensation, precipitation, buoyancy, and w diffusion, with an increase in the coupling strength and boundary layer depth necessary to transition from sugar/flowers to gravel.

3.4 Conclusions and Summary

This work uses a simple warm cloud model to simulate the organization of three patterns commonly seen in shallow trade wind cumulus. These patterns include sugar, small and disorganized non-precipitating clouds; gravel, small clouds organized into lines or arcs around cold pools; and flowers, larger aggregations of cloud that clear out their immediate surroundings. Our model in this chapter updates the one developed in the previous chapter and resolves the inability to produce larger flowers by virtue of including a prognostic equation for water vapor concentration q_v. By tracking water vapor explicitly, we are able to separate model coupling into cloud top and cloud base processes that simulate the vertical circulation of moisture through the cloud. The three resulting patterns match reasonably well with observed cloud sizes and size distributions.

Seven terms across the four equations were found to be critical in this model for all three patterns: condensation and precipitation (necessary for model stability across all three patterns); water vapor buoyancy, latent heating, and gravitational drag affecting vertical velocity; water vapor uptake from the ocean surface; and subsidence suppressing cloud water in large-scale downdrafts. On the whole the model reacted similarly to the loss of each individual term between the three patterns. The coupling processes affecting w, namely diffusion and cold pool expansion, controlled the formation of gravel while q_v advection at cloud base and q_c advection at cloud top both were necessary to form flowers. This model is thus most useful in assessing the structure of circulations surrounding flowers and gravel. We can see from cross-sections of the advection terms that flowers form a relatively steady mesoscale circulation, with q_v being advected inwards at cloud base, drawn through the central updraft and condensed, then pushed back outwards at cloud top against the boundary layer inversion. Circulations within gravel are more a function of condensate being pushed outwards into arcs in the presence of cold pools.

We also tested the impact of coupling distance on the resulting size of flowers and found that coupling over two grid points instead of one did not result in larger clouds. In fact, increasing the coupling distance resulted in the breakup of cloud edges as the advection terms acted as averaging agents most similar to lateral entrainment. We conclude going forward that a simple model only needs to be coupled with its nearest neighbors to produce recognizable patterns.

The importance of mesoscale circulations in cloud aggregation, particularly with flowers, is a known fact (Narenpitak et al. 2021), but less is known on the impacts of environmental moisture variance. As we continue this work in chapter 4, this model will be used to analyze differences in the surrounding environment, as well as the sensitivity to changes in both circulation strength and moisture concentrations.

Chapter 4

Investigation of Flower Size Using Both a Simple Model and Large Eddy Simulation

4.1 Introduction

Shallow cumulus organization remains an oft discussed topic, particularly in the context of climate change shifting these patterns and their resulting radiational feedbacks (Kazil et al. 2024). As such, many studies focus on the mechanisms that drive these small clouds to self-aggregate as they are frequently seen to do in both observational campaigns (Dauhut et al. 2023; George et al. 2023) and modeling studies (Narenpitak et al. 2021; Seifert and Heus 2013), sometimes spontaneously and without intention in the latter (Jansson et al. 2023). Of the cloud patterns identified by Stevens et al, sugar and flowers are the two most commonly discussed in literature, likely due to the ubiquitousness of the former and the striking nature of the latter (Stevens et al. 2019; Bony and Dufresne 2005; Dauhut et al. 2023). The presence of mesoscale circulations in flowers presents a particularly interesting challenge in modeling studies, as while we recognize the importance of these circulations, it is still unclear what drives their size and the ultimate size of the flowers that they form (Narenpitak et al. 2021).

Early modeling studies on mesoscale aggregation, such as that by Seifert et al, found that given a large enough domain with a high enough resolution, shallow cumulus would organize naturally even in the presence of homogeneous surface conditions or large-scale forcings (Seifert and Heus 2013). Many studies linked organization to the presence of precipitation and cold pools, as the two frequently occur together and provide circular feedbacks (Alinaghi et al. 2024b; Dauhut et al. 2023). However, other studies have determined that cold pools are not necessary for moisture aggregation, with flowers seen to blossom prior to the formation of any precipitation at the surface (Bretherton and Blossey 2017). The most commonly understood method for flower aggregation is via the mesoscale wind, itself a function of rising air within the cloud and subsiding air above it driving convergence at cloud base and divergence at cloud top (Narenpitak et al. 2021). This circulation redistributes moisture in the domain, causing moist areas to become moister and dry areas to become drier. The subcloud convergence, initially thought to desiccate clouds through mixing of dry air, actually has the effect of increasing cloudiness and thickening the cloud, which can lead to a decoupling between the boundary layer and the cloud layer (Vogel et al. 2022; Narenpitak et al. 2021). Convective-scale circulations are present within the mesoscale circulation sustaining the entire flower, particularly as precipitation forms later in the life cycle (Dauhut et al. 2023).

While much is analyzed regarding the dynamical controls on flower formation, it is unclear whether moisture concentrations have a significant impact on flower size as well. Indeed, Narenpitak et al found difficulty in modeling flowers as large as those observed and speculated on whether moisture availability was an additional controlling factor (Narenpitak et al. 2021) (P. Narenpitak, personal communication, June 23, 2025). The prevalence of precipitation that eventually forms in flowers points to moisture concentrations being a necessary consideration, if not for initial aggregation, then for maintenance of the flower structure. The presence of cold pools, for example, enhances the shallow mesoscale circulation by further driving convergence in the subcloud layer, and the amount of available water vapor and cloud water controls the degree to which cold pools are able to form (Dauhut et al. 2023; Alinaghi et al. 2024b). Vogel et al also found a moderate correlation between vertical velocity and relative humidity, showing a feedback between moisture convergence and aggregation, as well as that both cloud base convective mass flux and relative humidity are the dominant drivers of cloud fraction (Vogel et al. 2022). While the tropical boundary layer is assumed to be sufficiently moist, spatial variations in water vapor and cloud water are sufficiently large that they influence transitioning tiny sugar clouds into aggregated flowers (Narenpitak et al. 2021).

As discussed in previous chapters, simple models provide an additional tool to assess the dynamical structure of shallow cumulus, and coupling such a model allows us apply those ideas towards organized convection (Koren and Feingold 2011). Feingold et al showed that a simple model can be stably coupled over a grid in a dynamically relevant way, while Mascaut et al showed that such a coupled simple model can be used to simulate real world cloud patterns given sufficient observations (Feingold and Koren 2013; Mascaut et al. 2022). The previous two chapters showed two such simple models of our own capable of simulating aspects of real-world shallow cumulus organization, and it behooves us to move this study further out of the realm of theory and test our model's capabilities against real case studies in order to ascertain whether physical conclusions can be drawn.

This chapter compares the results from our simple model described in chapter 3 to those from a more complex modeling study to see if the simple model can sufficiently replicate those results without the aid of more involved physics. We then apply both models during a case study of the formation of flowers to determine the level of impact of moisture concentrations throughout the 3D domain on cloud size, then compare these results to variations in the circulation strength.

4.2 Methodology

4.2.1 Large Eddy Simulation (LES) Data

For the LES we look to the work of Narenpitak et al using the System for Atmospheric Modeling (SAM), developed in 2003 by Khairoutdinov and Randall to study cumulus convection surrounding the Atmospheric Radiation Measurement (ARM) Program Southern Great Plains site ((Narenpitak et al. 2021; Khairoutdinov and Randall 2003)). SAM is a 3-dimensional cloud resolving model (CRM) that uses a bulk microphysics scheme, anelastic approximations to the equations of motion, and parallel processing capabilities to reduce the computational cost typically associated with 3D models compared to their 2D counterparts (Khairoutdinov and Randall 2003; Khairoutdinov et al. 2002). It uses large-scale forcings, in this specific case from the European Center for Medium-Range Weather Forecasts (ECMWF) Reanalysis 5th Generation (ERA5) data set, to prescribe the synoptic environment, while SAM calculates the temperature and humidity profiles in the boundary layer (Narenpitak et al. 2021). SAM has been shown to have some sensitivity to horizontal resolution in the vertical profiles of cloud water and vertical velocity variance, which tended to increase and decrease, respectively, with a coarser resolution (Khairoutdinov and Randall 2003). This effect was mitigated in the LES simulations discussed here by running the model at a fine-scale 100 m resolution and coarse-graining the output to a 16x16 km^2 grid to remove the effects of microscale convection that do not contribute to mesoscale organization, as well as nudging the atmospheric profiles of temperature and humidity towards ERA5 in the free troposphere (Narenpitak et al. 2021).

SAM was used to reproduce a case of sugar-to-flowers transition observed during the Atlantic Tradewind Ocean-Atmosphere Mesoscale Interaction Campaign (ATOMIC) on 2-3 February 2020. The domain size is 192x192 km^2 with a 100 m horizontal grid spacing and a 50 m vertical grid spacing up to 5 km, then increasing geometrically up to 8 km, and the temporal resolution is 2 seconds with data output every 15 minutes (Narenpitak et al. 2021). These LES simulations corroborate the importance of mesoscale circulations driving moisture to converge while leaving dry areas drier found by Bretherton et al and seen in numerous other studies since ((Bretherton and Blossey 2017; Dauhut et al. 2023; Vogel et al. 2022; George et al. 2023)). In addition, the presence of cold pools, while ubiquitous around large precipitating shallow cumulus, do not appear to drive the initial organization into flowers but rather uphold the flower shape subsequent to formation (Narenpitak et al. 2021; Dauhut et al. 2023).

4.2.2 Data Availability and Processing

LES data has been made publicly available from Narenpitak et al as 3D fields of cloud and water vapor concentrations over a period of 24 hrs (Narenpitak et al. 2021). The 3D fields were used here to calculate the effective diameter of flowers as they formed and developed over time by calculating the equivalent area covered by a circular cloud from the same number of cloudy pixels. Peak cloud diameters were seen around a height of 1500 m, shown in figure 4.1 as near the height of maximum q_t and w perturbations. A crude tracking algorithm enabled us to follow clouds over time by assigning cluster numbers to adjacent cloudy pixels in the same manner as described in the previous chapters, then tracking the most frequent cluster number, i.e. the large flower, as it passed through a user-defined box. Once the cloud was identified at each time step, we calculated the maximum q_c and q_v within the total cloud area at each height and correlated it with effective cloud diameter over time.

In addition, vertical profiles of total water concentration q_t and vertical velocity w were available prior to and following flower development, shown in figure 4.1. These profiles were organized into quartiles by total water path (TWP). Quartile 4 represents the moistest pixels in the domain and is considered synonymous with flowers while quartile 1 represents the driest pixels, with pixels in each quartile not necessarily being adjacent to one another. Data from quartile 4 was used to estimate the average strength of the circulations in the flowers by calculating the difference in maximum and minimum vertical velocity over the profile. Because only two time steps were present here, we looked at the percent change in circulation strength as compared to changes in average cloud size and maximum q_t.

Narenpitak et al conducted two simulations of the sugar-to-flowers transition observed during ATOMIC (Narenpitak et al. 2021). We followed their methodology with two runs of our simple model to observe the effects of the vertical velocity: a control run (hereafter referred to as CTL) allowing clouds to develop naturally and a run that forcefully reduced the domain mean w by 50% at each time step for a period of 10 hrs during the middle of the model run (referred to as WeakW). We first looked at how altering the vertical velocity in this manner affected the development of flowers in our simple model and compared our results with those of Narenpitak et al, then took a deeper dive into investigating whether or not the moisture concentrations played an equally important role in developing flowers as compared to the circulation strength (Narenpitak et al. 2021).

Clouds in our simple model were classified by cluster using the same algorithm described in the previous chapters. We identified six flowers present at the end of the model run, shown in

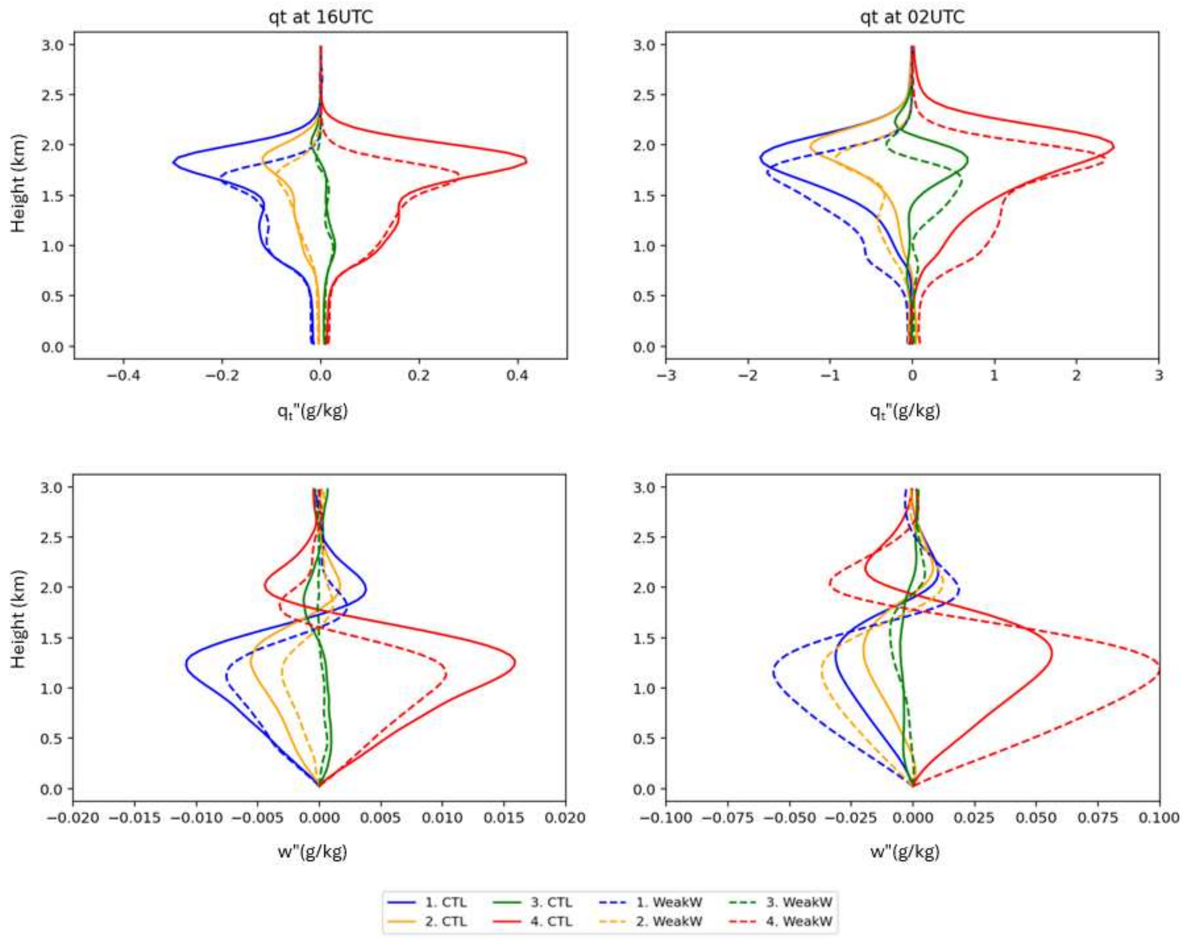

Figure 4.1: Profiles of q_c (top) and w (bottom) perturbations before (left) and after (right) flower formation using LES data from Narenpitak et al (Narenpitak et al. 2021). Data is divided into quartiles based on total water path at each grid point, with quartile 1 showing the driest points and quartile 4 the moistest points. Solid lines show CTL run output while dashed lines show WeakW run output. Note the variability in the horizontal axis scales.

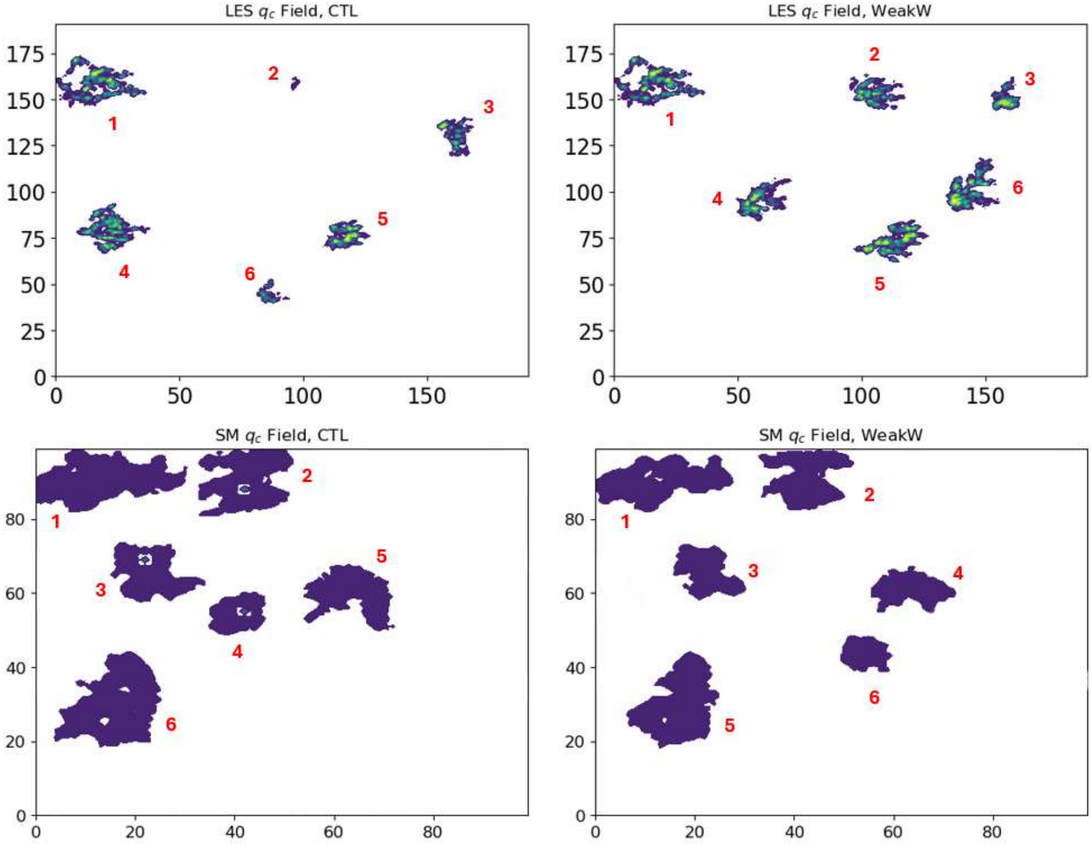

Figure 4.2: Six clouds identified and tracked through the domain for analysis.

figure 4.2, and manually tracked their location backwards in time to their origin. Due to the lack of a horizontal wind profile in the simple model, these clouds remained fairly stationary over time and made tracking very simple. The six clouds were measured for peak water vapor concentration q_v, peak cloud water concentration q_c, and peak circulation strength as defined above within each cloud. Cloud size was again measured using the effective diameter of a circular cloud containing the same number of cloudy pixels as the model-derived cloud. We then calculated the Pearson correlation between q_c, q_v, and circulation strength with the cloud size over time and compared these results to those correlations calculated using LES output from the (Narenpitak et al. 2021) study. Correlations were lagged between 0-2 hours to see whether the internal cloud properties were leading the cloud size as the flowers developed.

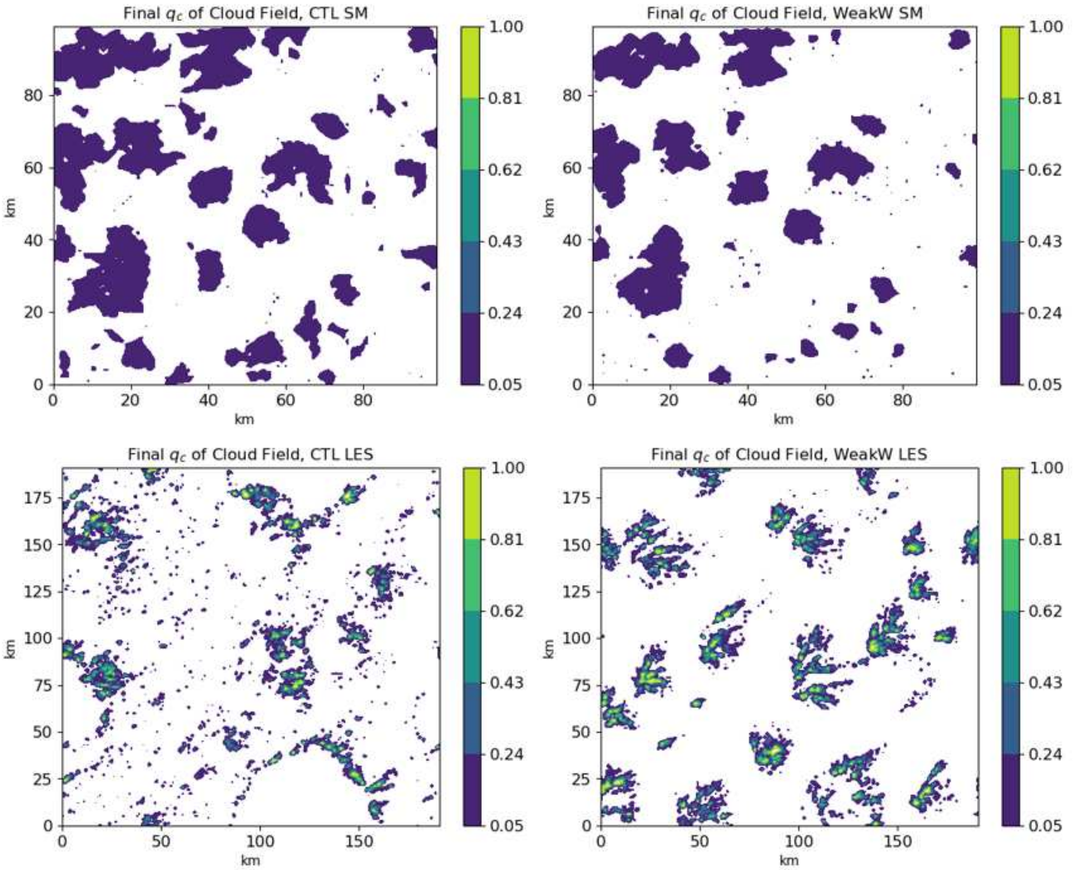

Figure 4.3: Final q_c field for the control run (left) and the WeakW run (right) using data from our simple model (top) and the LES (bottom).

As results are discussed in the following section, data from the simple model will be referred to as ’SM’ and LES data will be referred to as ’LES’. The control and WeakW runs are labeled as ’CTL’ and ’WeakW’, respectively. Each run of SM using either CTL or WeakW conditions was conducted eight times using different sets of initial conditions as defined in chapter 2 figure 14 to verify the robustness of the results. One set of representative output for SM will be shown here for comparison with the LES.

4.3 Results

4.3.1 Flower Development in Weak Upward Motion

The final cloud fields for both SM and LES are shown in figure 4.3 and we can immediately ascertain a number of differences between the CTL and WeakW runs. First, CTL has flowers that have progressed further in their development, forming strong cold pools earlier in the LES as noted by Narenpitak et al and identifiable in the arcs surrounding clear air (Narenpitak et al. 2021). The LES also forms a number of small sugar-type clouds interspersed about the domain which are not present in SM, likely as a result of the strong coupling in SM dispersing and mixing out these small clouds as discussed in the previous chapter.

Second, clouds in CTL are slightly larger, which is more readily apparent in SM but can be diagnosed from the way that the LES clouds are less compact as compared to the WeakW output. This difference in average cloud size over time is further illustrated in figure 4.4 showing the average diameter of clouds within the domain starting from the point of flower formation. SM forms flowers almost immediately with the average size staying relatively consistent throughout the run, while the LES takes around 6 hrs to begin aggregating sugar into flowers with WeakW lagging behind CTL by roughly an hour. The point at which w is reduced is readily apparent in SM with the sharp decrease in average cloud size at hour 6. In both cases, the average cloud size is higher in CTL than in WeakW by the end of the run. The suppression of vertical velocity midway through the model run delays the LES in aggregating flowers, while for SM which forms flowers almost immediately, results in these clouds breaking apart in the weaker updrafts and reforming at a smaller size once the natural updraft strength is restored. Narenpitak et al states that the stronger updrafts in CTL intensify the mesoscale circulations which promote moisture aggregation earlier and stronger (Narenpitak et al. 2021). We see that same effect reflected in SM as the coupling term controlled by w that we know drives the flower to aggregate, namely the vertical velocity diffusion, is reduced, thus weakening the circulation.

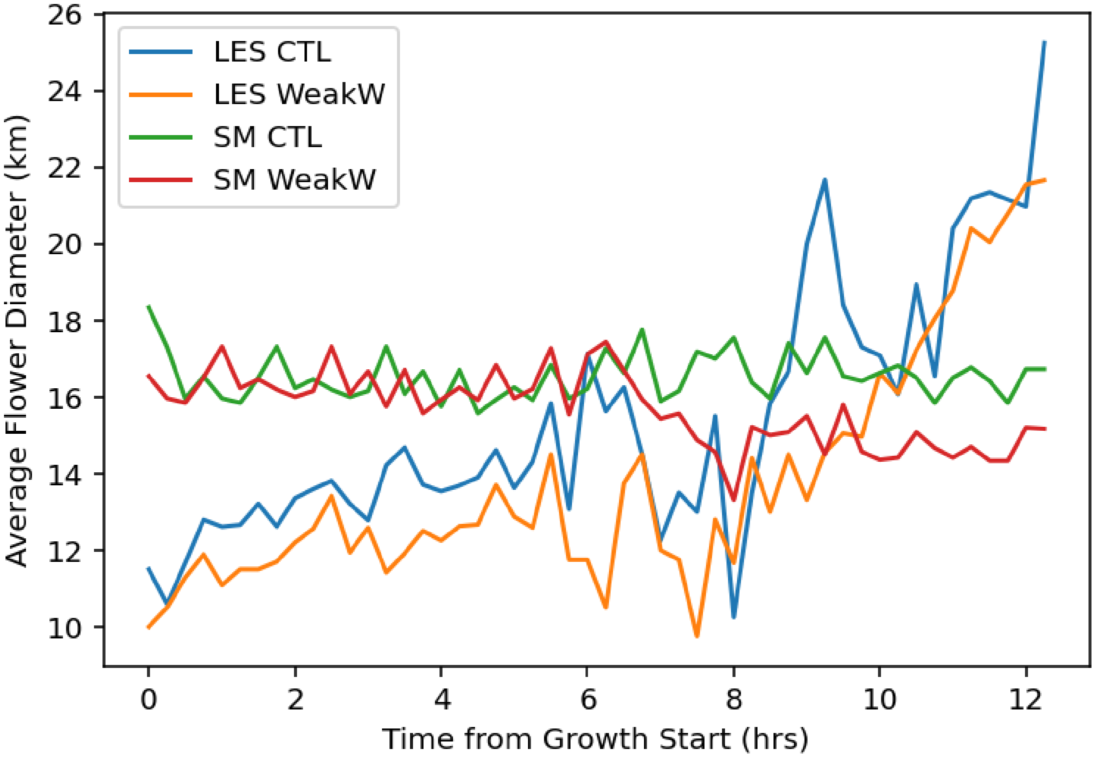

Figure 4.4: Average cloud diameter over time. t=0 represents the time at which flowers are first identifiable in the domain for each model run, which occurs in our simple model after 1-2 hours while the LES takes 13-14 hours.

Finally, WeakW results in more flowers forming than does CTL. In the LES this is the result of the weaker circulations eventually catching up to and surpassing the CTL circulations in strength, aggregating moisture more quickly, whereas CTL has already formed cold pools by the end of the run which appear to disrupt the formation of new flowers (Narenpitak et al. 2021). In SM the increase in cloud number results from the weaker w breaking up the already present flowers, which then reform into new, smaller flowers once w is restored. This effect on SM is more pronounced depending on when the adjustment to domain-mean w is applied. Reducing w in the middle of the run as we have in the WeakW experiment, after flowers have already formed, results in the pattern as described above. However, if we instead reduce w for the entirety of the model run, before flowers have a chance to form, then the ultimate size and number of clouds by the run's conclusion is further decreased and increased, respectively.

Figure 4.5 gives another look at how WeakW compares to CTL in SM by measuring the changes in average cloud diameter and cloud number as a result of each individual process in the same manner as presented in chapter 2. Just by itself the full-process control run in WeakW resulted in both smaller and fewer clouds compared to its counterpart in CTL as discussed above, and this trend mostly continues as each process is removed. We note that the removal of gravitational drag and precipitation each cause an increase in cloud size for WeakW as opposed to a size decrease for the control. For CTL removing both terms results in the model becoming unstable and so no clouds are produced, thus appearing as a cloud size and number decrease. In the case of removing gravitational drag, the reduction of w in WeakW acts in a similar manner to this term and allows flowers to form in an almost normal manner. Meanwhile removing the precipitation term in WeakW produces the very interesting effect of propagating the initial cloud to its boundaries in a pattern almost similar to gravel. This is caused by the dramatically increased rain water, no longer allowed to precipitate out from the cloud, mimicking a strong cold pool that induces strong upward motion along the cloud boundaries at the edge of the gust front, enhancing the cloud in that area.

4.3.2 Moisture Variations Compared to Cloud Size

While the effects of the vertical velocity on the mesoscale circulation are well-established (Bretherton and Blossey 2017; George et al. 2023), less study has been made towards whether the environmental moisture has a significant impact on the growth rate and ultimate size of flowers. To investigate this further, we looked at whether cloud water and water vapor concentrations at different heights in the cloud correlated strongly and/or independently to the change in cloud size over time. Figures 4.7-4.8 and 4.10-4.11 show the correlation of q_c and q_v in CTL and WeakW, respectively, to the cloud size at each level to ascertain at what height(s) these variables are the best predictors of size, with a lag of 0-2 hrs. For CTL in figure 4.7, q_c is best analyzed in the range of 1500-2000 m shown by the yellow-green lines, which from figure 4.1 we know is the peak of q_c in the column and encompasses the main depth of the cloud itself. Increases in q_c at these levels best precede increases in cloud size by one hour, which may give an insight into the strength of the

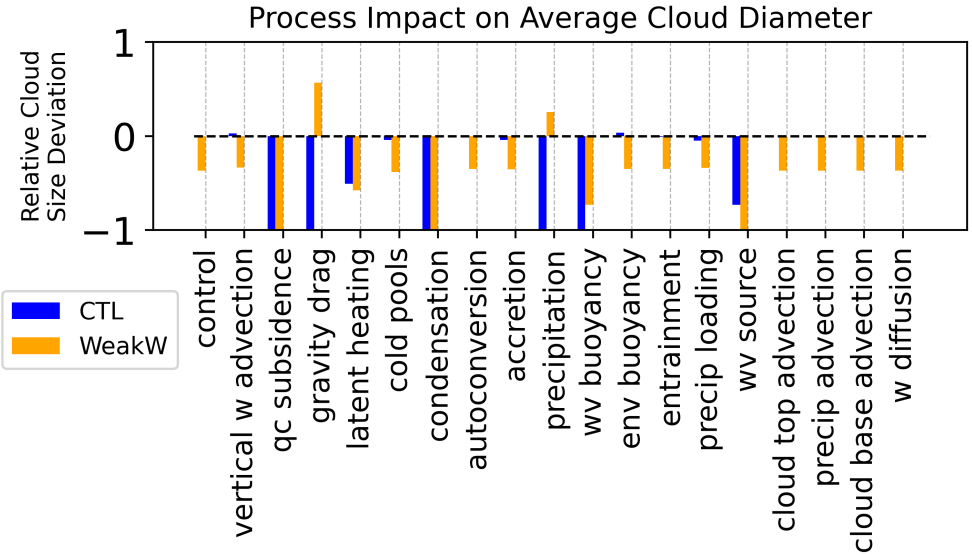

(a)

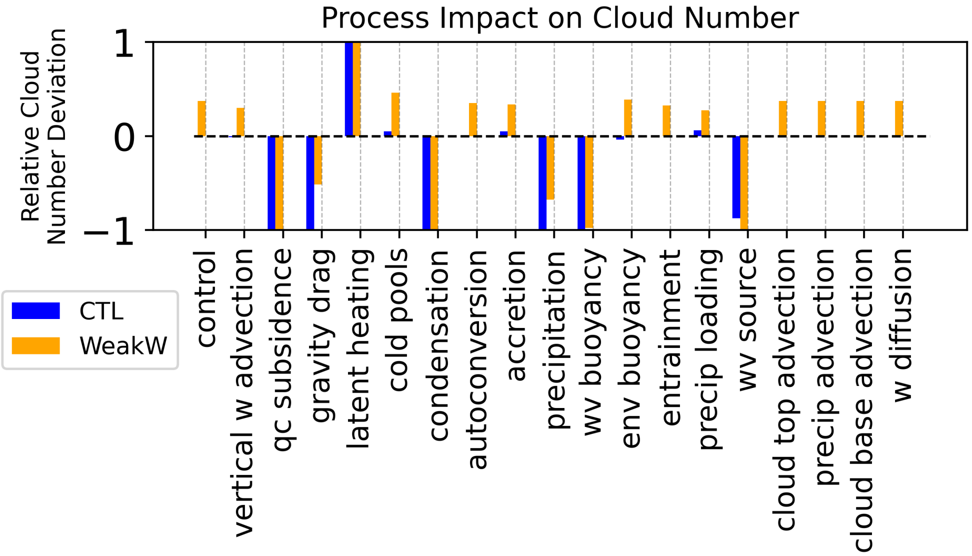

(b)

Figure 4.5: Changes in average cloud diameter (top) and average number of clouds in the domain (bottom) as a result of removing individual processes for the control run (blue) and a run using 50% reduced mean vertical velocity (orange).

circulation advecting q_c through the cloud. Size correlation with q_c drops off steadily with height in the upper regions of the cloud and through the inversion layer, where despite increasing with lag time are essentially non-correlated once we reach the dry free troposphere. In the subcloud layer, despite the very low values of q_c throughout, the correlation between q_c and cloud size is very high with no lag time and decreases significantly when the lag time is increased. The relationship between subcloud relative humidity and cloud fraction was also measured during the EUREC^{4}A campaign and was found to be exaggerated by most models as compared to real-world observations, which may be the case here too (Vogel et al. 2022). q_c changes in the subcloud layer are likely responding to changes in cloud size, not the other way around, as the relationship falls off once the lag time is increased beyond the growth rate of the cloud.

Correlations with q_v with height in figure 4.8 surprisingly show a similar relationship as that of q_c, with peak correlation between q_v and cloud size occurring in the middle to upper regions of the cloud with a lag time of one hour. This is in spite of q_v concentrations being highest in the subcloud layer (Bretherton and Blossey 2017; Dauhut et al. 2023) and may be an indicator of the stronger decoupling of the subcloud layer present in CTL that prevents moisture increases near the surface from strongly impacting the cloud layer. (Narenpitak et al. 2021). The data in figure 4.6 shows that the temporal variation in q_v in the subcloud layer is initially very steep then stabilizes during the period of maximum cloud growth, likely the result of strong circulations below cloud, whereas in the upper levels the aggregation of water vapor occurs much more gradually as the decoupling slows the rate of moisture circulation into the cloud. The changes in cloud size, shown by the black lines, most closely align with changes in both q_v and q_c in the upper region of the cloud. We again see the sharp drop-off in correlation between q_v and cloud size in the subcloud layer with increasing lag time, consistent with the reasoning previously given.

In the WeakW case in figure 4.10, the height of maximum q_c correlation is lower as a result of the shallower boundary layer producing shallower clouds (Narenpitak et al. 2021), but otherwise follows the same general pattern with correlations decreasing with height up through the inversion

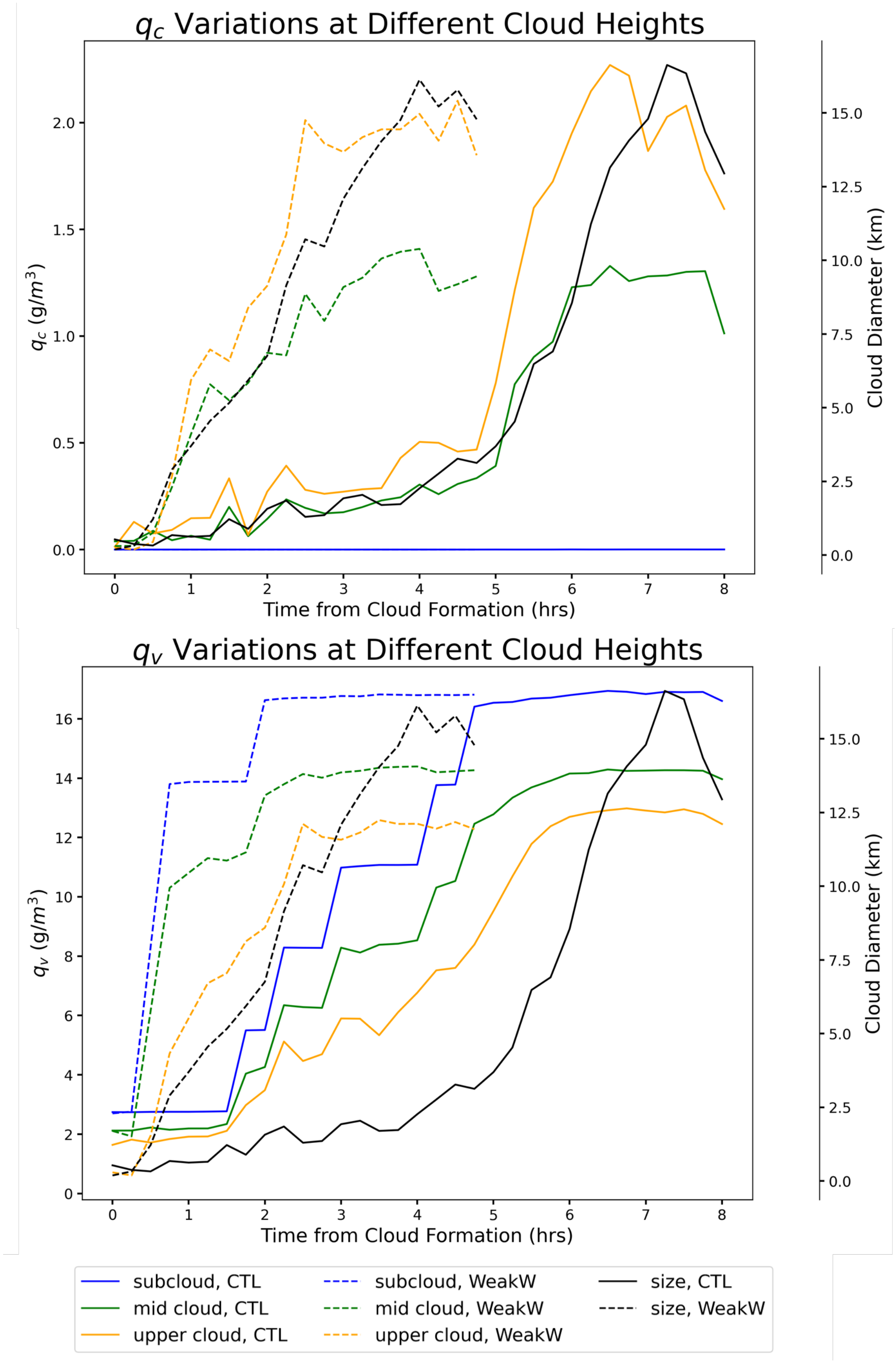

Figure 4.6: Average changes in q_c (top) and q_v (bottom) at different atmospheric levels within the column of a flower over time. Subcloud (blue) = 525 m, middle cloud (green) = 1525 m, upper cloud (orange) = 2025 m. Cloud properties are measured from the time of cloud formation. Solid lines show CTL, dashed lines show WeakW. Averages are taken over the six tracked clouds in figure 4.2.

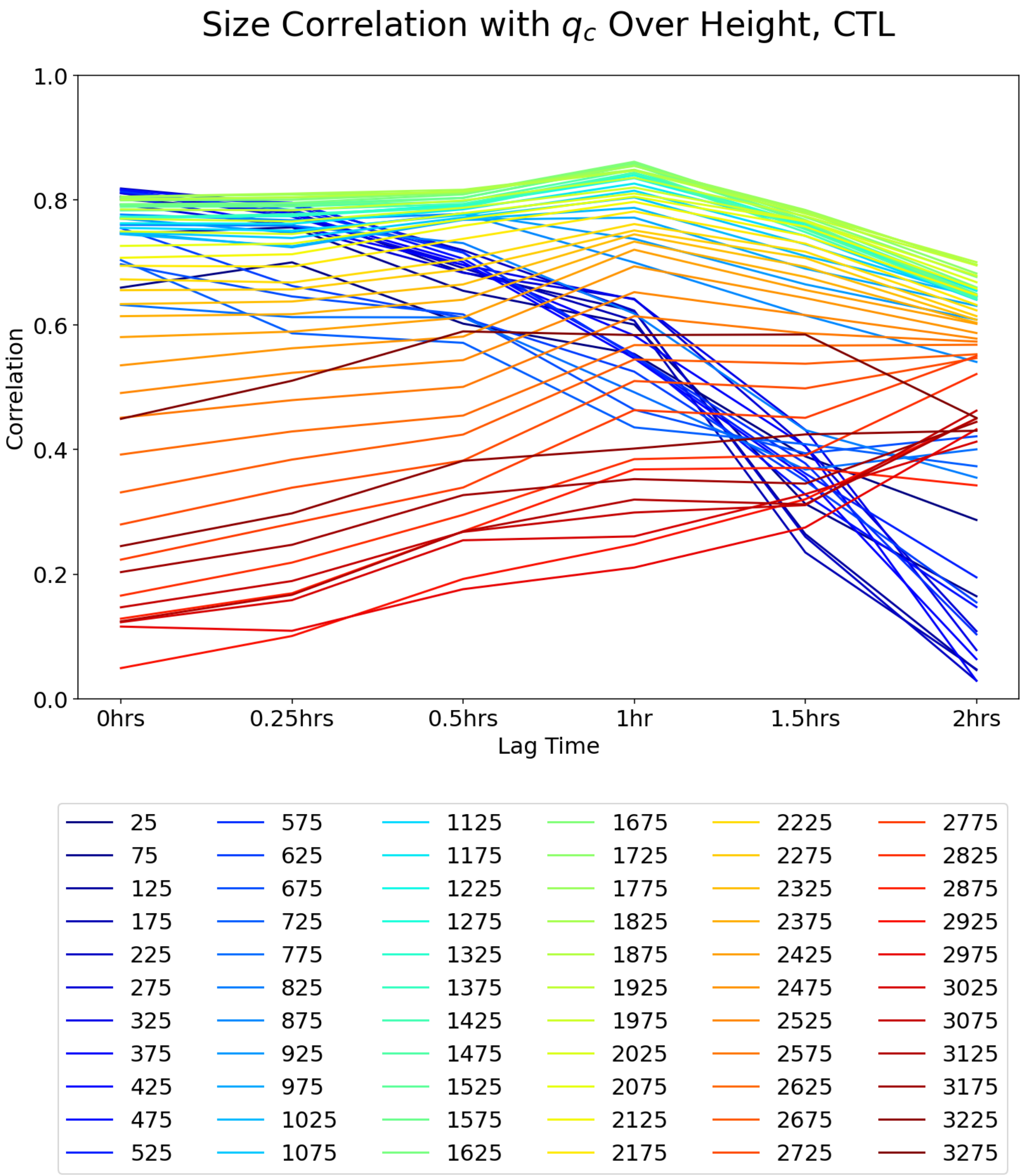

Figure 4.7: Lag correlations between cloud diameter and q_c at different heights (in m) as they develop over time using LES control output. Peak correlation between q_c and cloud size occurs at 1775 m with a lag time of 1 hr.

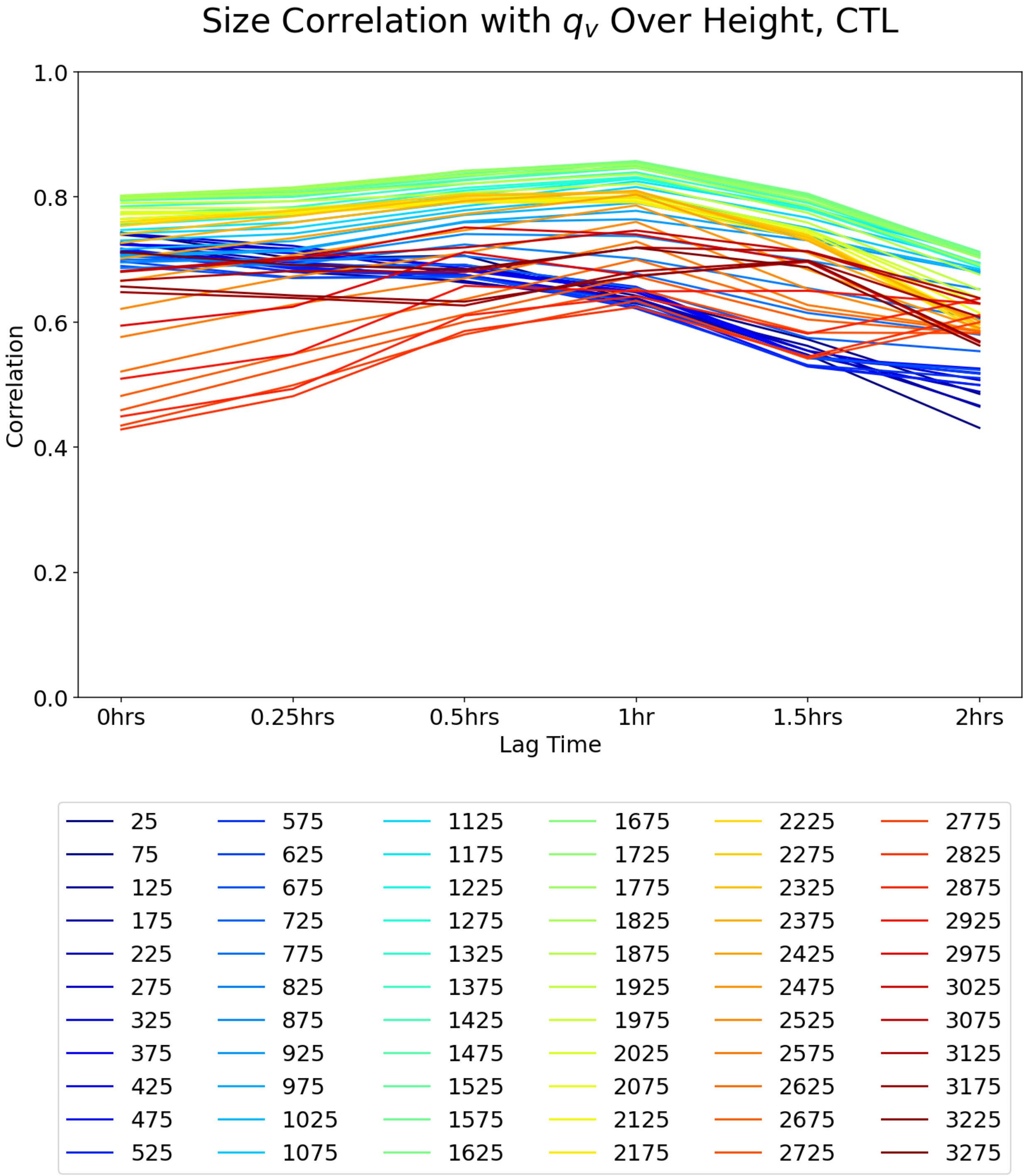

Figure 4.8: Lag correlations between cloud diameter and q_v at different heights (in m) as they develop over time using LES control output. Peak correlation between q_v and cloud size occurs at 1725 m with a lag time of 1 hr.

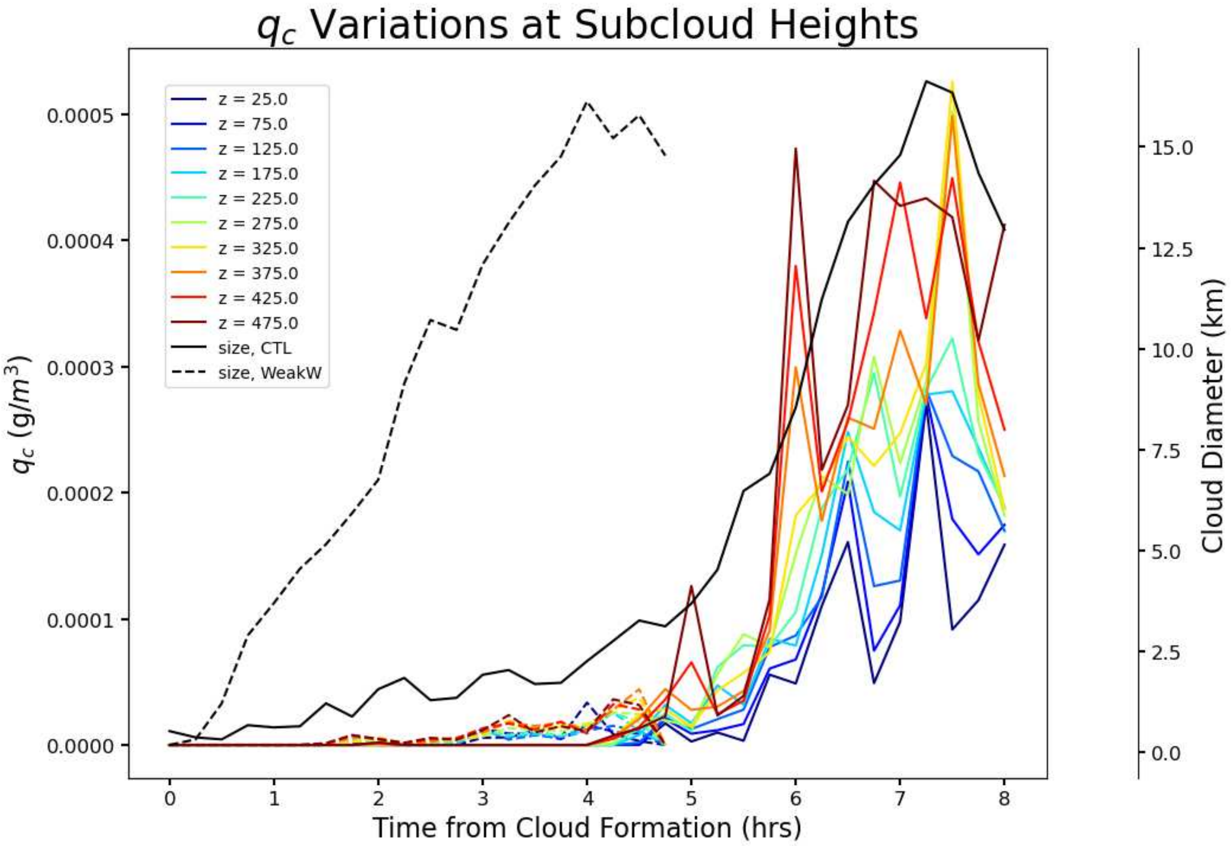

Figure 4.9: Same as q_c in figure 4.6 but for heights (in m) in the subcloud region to show variance at lower concentrations. Solid lines are for CTL, dashed lines are for WeakW.

layer and into the free troposphere. The subcloud layer tells a different story with q_c between CTL and WeakW, as the CTL correlations below cloud were quite organized with height whereas with WeakW they are all over the place. We know that the boundary layer is less decoupled in WeakW in the presence of the initially smaller clouds, meaning that circulations extend much deeper below the cloud base as opposed to the more independent circulations in the decoupled CTL run (Bretherton and Wyant 1997; Narenpitak et al. 2021). This means that in WeakW the subcloud layer is more well-mixed, a structure we can see in figure 4.9 by focusing in on the very low q_c concentrations in the subcloud layer. q_c is small and uniform in WeakW in the 500 m nearest the surface reflecting the strong mixing, while in CTL q_c increases with height in the decoupled circulation. Thus it makes sense why q_c has little correlation with the cloud size in WeakW below cloud when concentrations are simply constant.

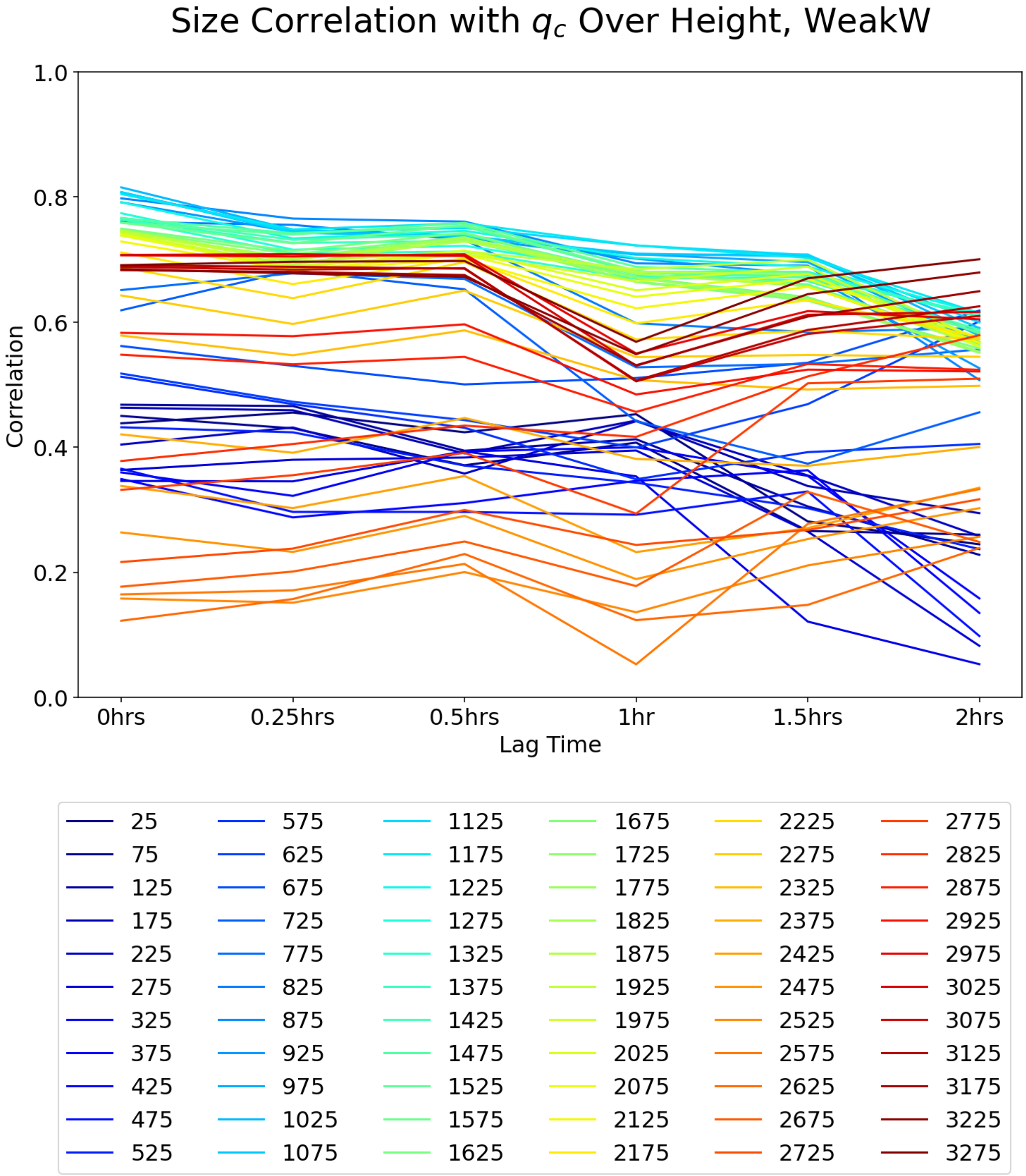

Figure 4.10: Lag correlations between cloud diameter and q_c at different heights (in m) as they develop over time using LES WeakW output. Peak correlation between q_c and cloud size occurs at 875 m with no lag time.

q_v correlations with cloud size in the WeakW case in figure 4.11 were on the whole slightly lower than their counterparts in CTL, with the peak correlation again being at a lower height due to the shallower boundary layer. The pronounced lag correlation at one hour is also no longer present, with values instead remaining relatively steady around 0.75. We can see the reason for this in figure 4.6 in terms of the length of the growth period of clouds. For CTL cloud sizes continue to increase for 1-1.5 hrs after q_v stabilizes, while in WeakW this additional growth period lasts 1.5-2 hrs. Therefore a longer lag time may actually show a later peak in the q_v correlation for WeakW, which unfortunately can't be tested due to the length of the simulation. Correlations with q_v at the lowest levels with zero lag are strongest of all those calculated and higher than the corresponding heights in CTL, as in the same manner that the weakened boundary layer decoupling resulted in the strong mixing of q_c below cloud, it also promoted enhanced advection of water vapor into the moist patches preferred by shallow cumulus and more water vapor flux between the cloud and subcloud layers (Seifert and Heus 2013).

4.3.3 Moisture and Circulation Controls on Cloud Size

Figures 4.12 and 4.13 show the correlation between different cloud properties with the cloud size as assessed using the LES and SM, respectively, within each cloud analyzed from figure 4.2. For the LES, most clouds show a higher correlation with cloud water concentrations than they do with water vapor, particularly in CTL. This is consistent with our previous analysis as we correlate size with q_c and q_v nearer to the top of the cloud. The differences between the CTL and WeakW runs may again be related to the increased decoupling of the boundary layer in CTL, which inhibits transport of water vapor into the cloud from below and therefore limits the availability in cloud (Kazil et al. 2017). The deep circulations present in WeakW mean that both q_c and q_v are able to influence the cloud size in equal measure, leading to no consistent distinction between the two. Additional differences may arise simply due to the clouds chosen to be tracked, which are at different points in their life cycle by the end of the model run. Clouds 3 and 5 in CTL appear to

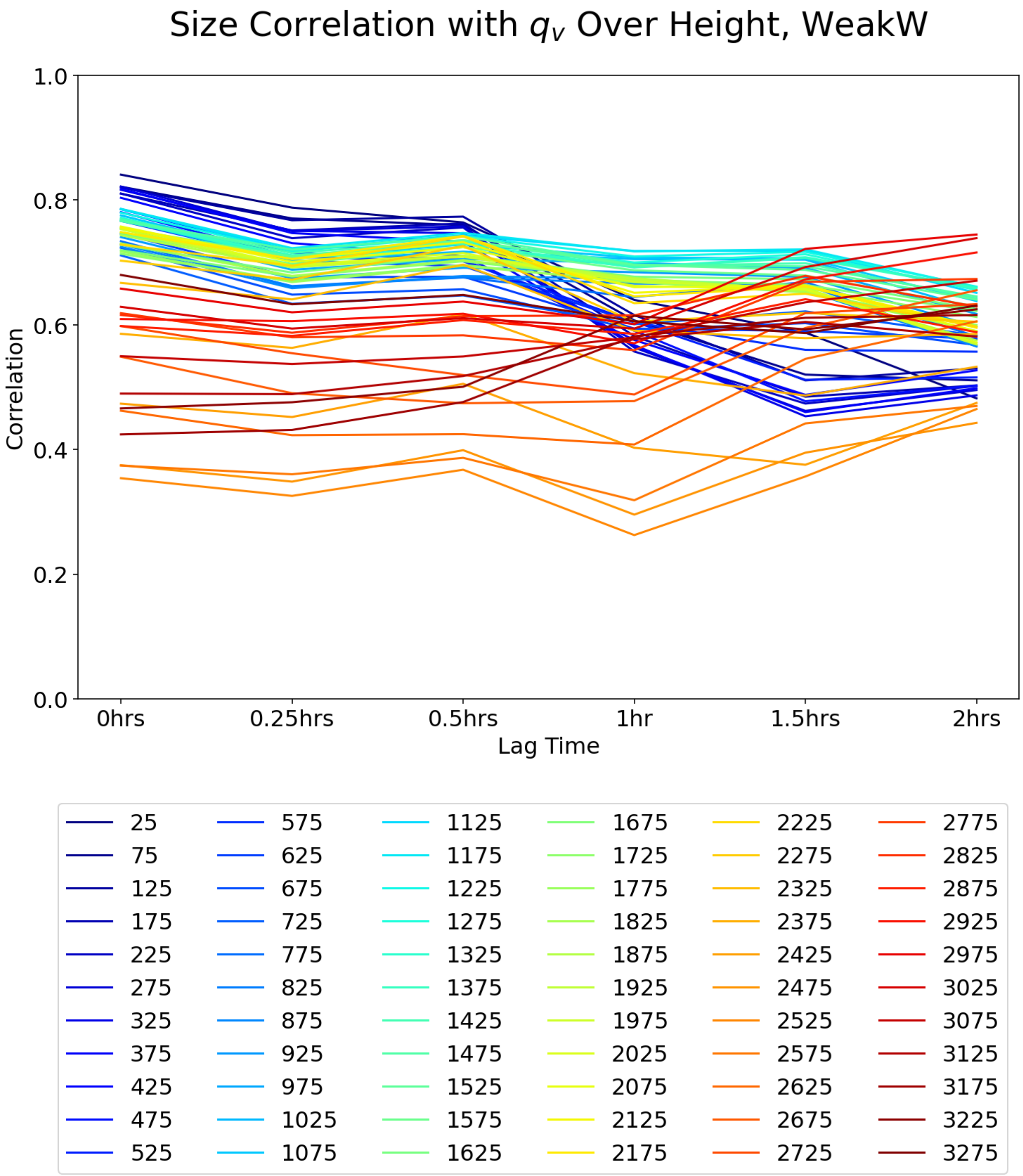

Figure 4.11: Lag correlations between cloud diameter and q_v at different heights (in m) as they develop over time using LES WeakW output. Peak correlation between q_v and cloud size occurs at 225 m with no lag time.

still be growing, 1 and 4 are both fully mature, and 2 and 6 are in the decaying stage by the end of the run.

For the SM we actually observe the opposite relationship between q_c and q_v for CTL, with q_v correlations (which are generally equivalent to the correlation with circulation, making the blue and green lines concurrent and thus difficult to see) being the higher of the two. In CTL this is likely impacted by the rate at which flowers form, which occurs within one hour of model initialization with cloud size then remaining relatively constant throughout. Both q_c and q_v concentrations are also fairly steady but q_c concentrations are higher in the model, making them more susceptible to variance with minor changes in cloud size. By reducing the domain mean w in WeakW in that way and forcing a cloud size change midway through the model run, we can get a better picture of the differences between q_c, q_v, and circulation. The correlations for WeakW are calculated starting at the point at which clouds reach their minimum size, roughly halfway through the period of reduced w, and encompass the slow growth to their final size. The results are a mix of those from the LES CTL and WeakW runs, with q_c correlations exceeding those of q_v in half of the cases and being equivalent in the other half. The former group occurred in the largest clouds which match to those results of fully mature clouds in LES CTL, while the smaller clouds of the latter group match the results from the decaying clouds in LES CTL. The circulation strength does not appear to be a consistent distinguishing factor when compared to q_c and q_v, being equivalent in correlation to q_c for the large clouds while a mix of strong and weak for the small clouds.

Averaging over our tracked clouds we can thus estimate the importance of our three different variables. Figure 4.14 shows the comparison between correlations of q_c, q_v, and circulation strength, with error bars representing one standard deviation from the mean. The most robust difference was between circulation/q_v and q_c in the CTL run of SM, which is again opposite to the results of the other three runs and may have more to do with the steady state nature of the run itself. The remaining three runs all showed q_c correlations exceeding those of q_v, but with enough variance that we cannot draw a conclusion to say that these correlations are separate, particularly as the q_v correlation varies quite dramatically. Only the WeakW run of SM showed a large differ-

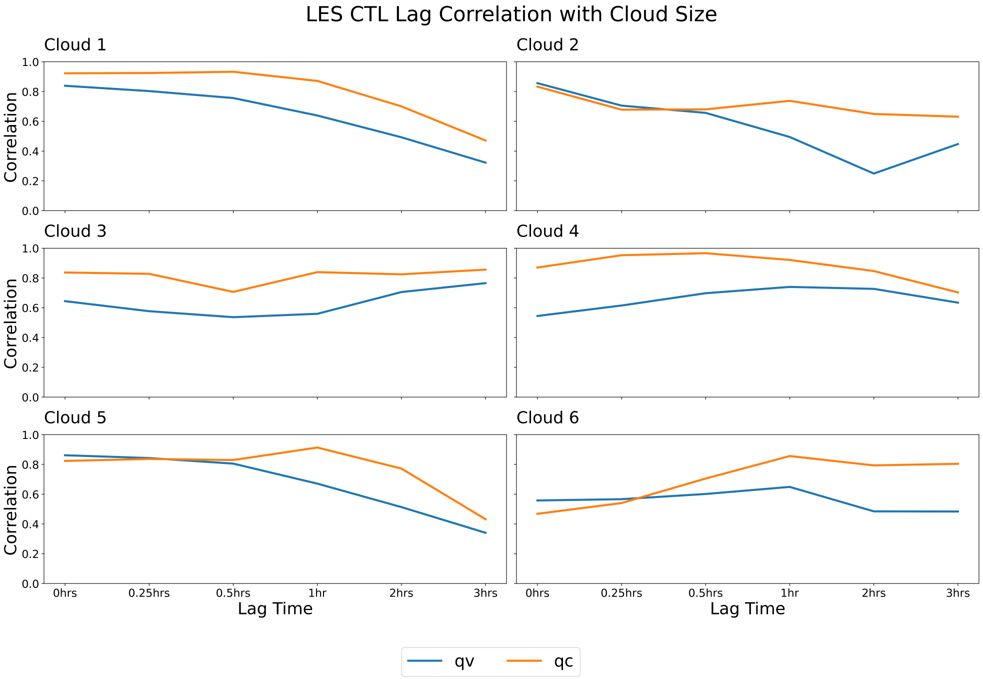

(a)

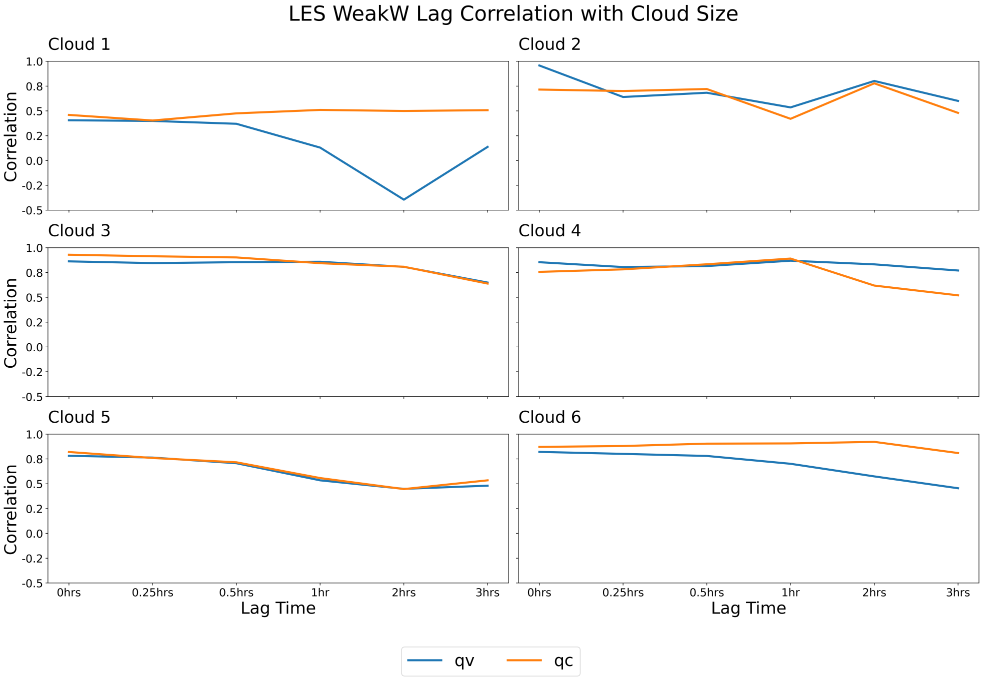

(b)

Figure 4.12: Lag correlations between cloud diameter and q_c/q_v for six different clouds in the domain as they develop over time using 3D LES output. The top image shows the control run and the bottom image shows the WeakW run. Correlations with circulation strength are not shown for the LES data due to 3D vertical velocity profiles not being available.

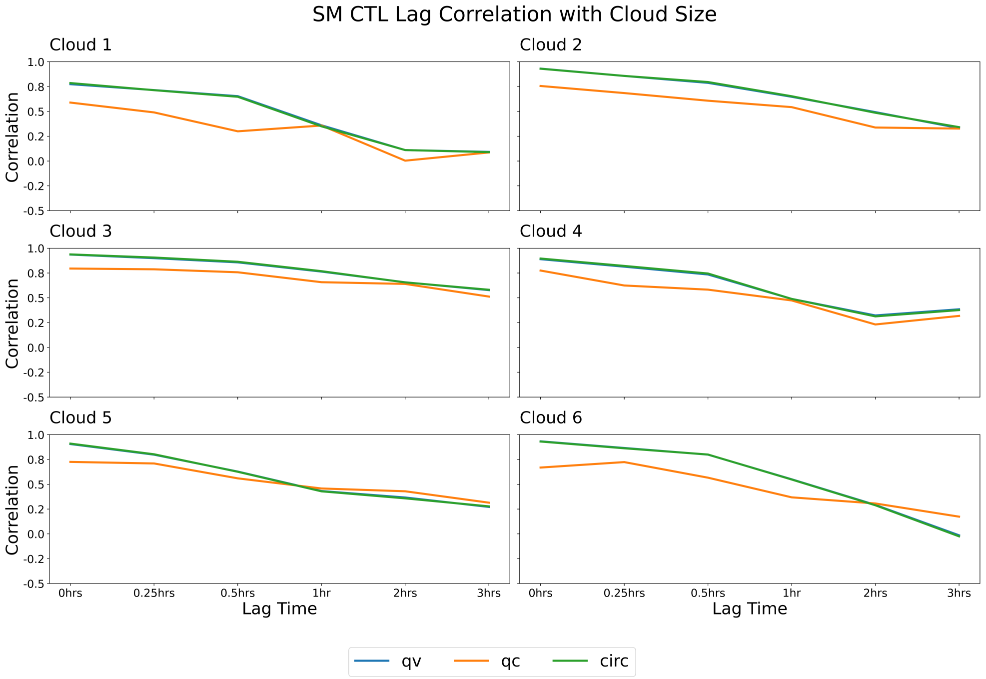

(a)

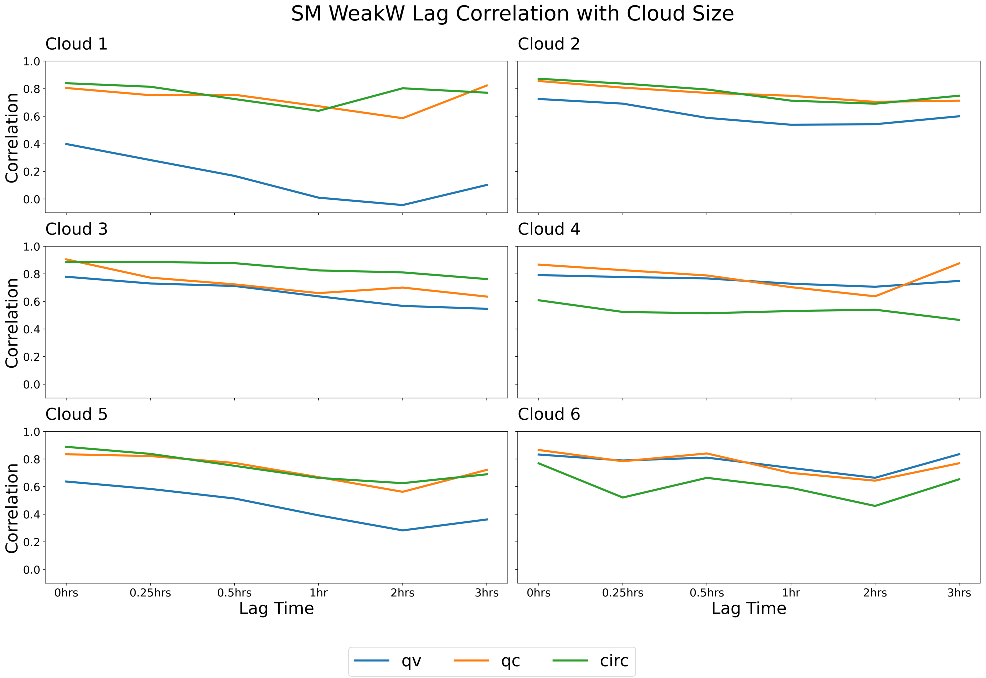

(b)

Figure 4.13: Lag correlations between cloud diameter and q_c/q_v/circulation strength for six different clouds in the domain as they develop over time using out simple cloud model. The top image shows the control run and the bottom image shows the WeakW run. Correlations with circulation strength and peak q_v were found to be virtually equal in the control run, whereas correlation with q_v was much lower in the WeakW run.

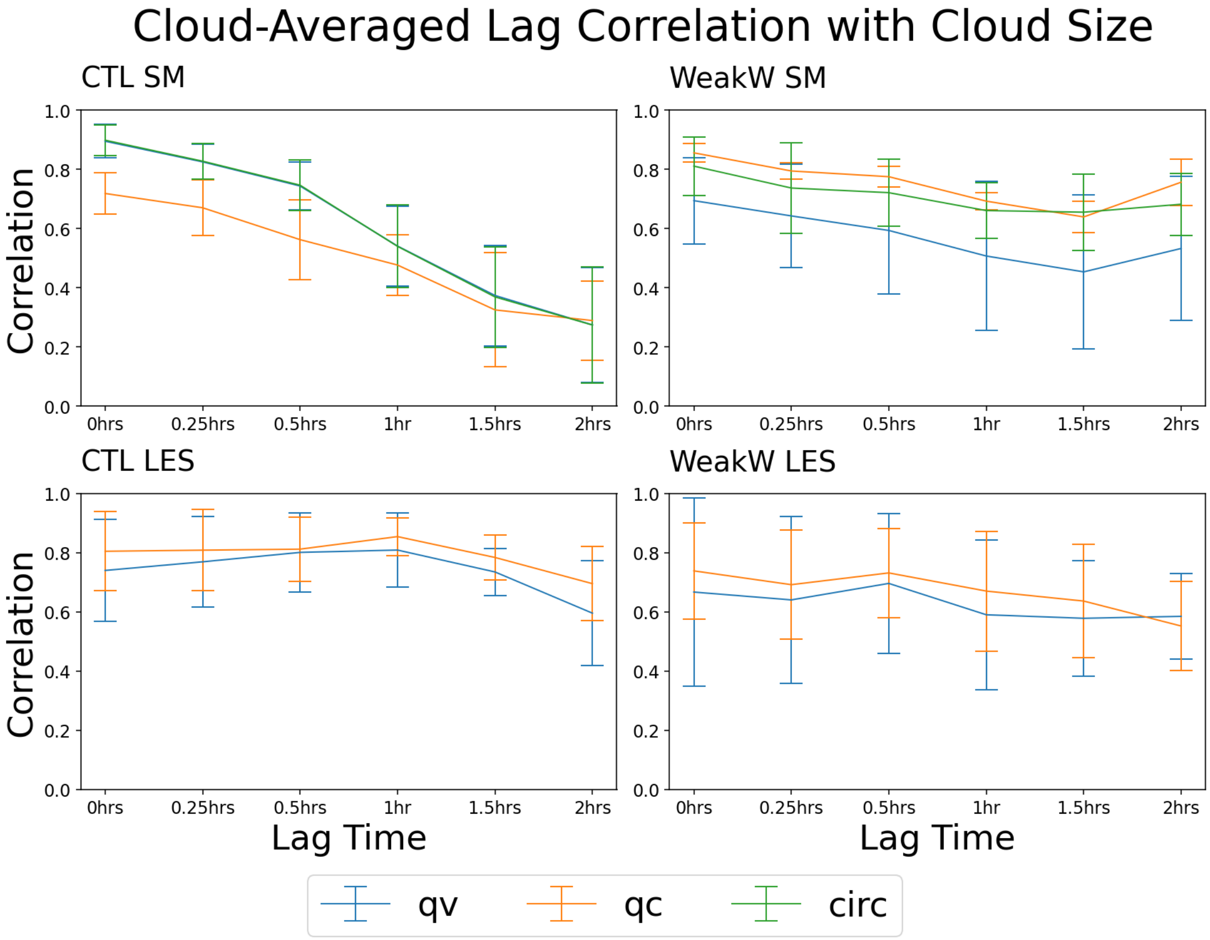

Figure 4.14: Lag correlations between cloud diameter and q_c/q_v/circulation strength averaged over six different clouds in the domain as they develop over time. Top plots show correlations using our simple cloud model and bottom plots show output using 3D LES output. The control run is on the left and the WeakW run in on the right. Correlations with circulation strength are not shown for the LES data due to 3D vertical velocity profiles not being available.

ence in the correlations with zero lag time. The cloud size correlation to circulation strength was generally high in both CTL and WeakW cases, but again appears to be indistinguishable from q_c.

Finally, we use the LES profiles to look at how changes in cloudy column moisture compare to the strength of the circulations and relate these results our previous discussion. Figure 4.15 shows the changes in average cloud size, total water concentration, and circulation strength, calculated as described in section 4.2.2. All three variables have a stronger percent increase in the WeakW case as despite taking longer for flowers to form, the much stronger circulations seen in figure 4.1

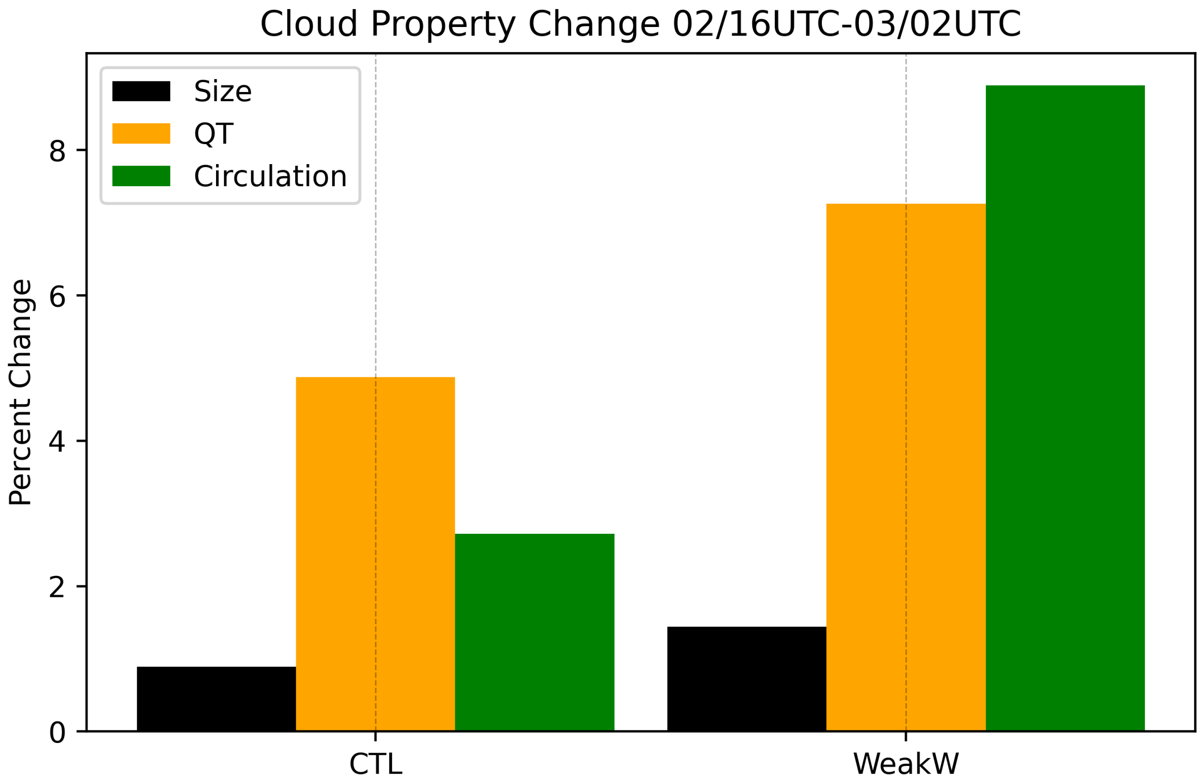

Figure 4.15: Percent change in cloud properties between 02/16UTC and 03/02UTC using LES profiles in the moistest quartile. QT is taken as the maximum total water concentration in the column, while circulation strength is calculated as the difference between maximum and minimum w in the column. Cloud size is calculated as previously discussed using 3D LES output.

accumulate available moisture more quickly and grow the flowers to a larger size. CTL grows q_t higher than it does the circulation strength given the longer period of time, but this also means that the rate of change in circulation strength is closer to the rate of change in cloud size, which matches the CTL results from SM with circulation strength being equivalently correlated with q_v and higher than q_c. Conversely the rate of change in moisture in WeakW is very similar to that of circulation, whereas SM could not fully distinguish between the two.

4.4 Conclusions

In this study we analyzed the environment in which flowers formed using data from both our simple model developed in chapter 3 as well as from a series of LES runs from Narenpitak et al

(Narenpitak et al. 2021). The models were run in both a naturally-developing environment and one in which the domain mean vertical velocity was reduced by 50% for a period of ten hours. For the LES, this delayed flower formation by almost two hours with initially smaller clouds, which then grew more quickly to end with stronger circulations, more clouds, and larger clouds. The simple model grew flowers almost immediately from the initial conditions, but the reduction in w served to break up these clouds slightly which then reformed at a smaller size once w was restored. Sensitivity tests on the different processes within the simple model showed that the same processes critical to flower formation were further affected by the weak w. The exceptions to this were removing the gravitational drag, which acted to counter the decreased w, and removing the precipitation, which produced a dramatically enhanced cold pool effect as opposed to the control run's unstable growth.

Correlating changes in average cloud size to cloud water and water vapor concentrations at different heights in the boundary layer and cloud layer showed that both q_c and q_v correlated most strongly to cloud size at heights in the mid to upper levels of the cloud. The control run saw the strongest correlations by lagging cloud size behind q_c and q_v by one hour while the WeakW run saw no lag, which is most likely a function of the faster growth in the latter case. With a longer model run, a longer lag time may be prudent. Weaker boundary layer decoupling in the WeakW run also produced stronger circulations through the depth of the boundary layer, resulting in subcloud q_v being well correlated with cloud size while q_c was well-mixed.

Comparing moisture controls on cloud size to circulation strength, there is some evidence of circulation outweighing q_c in the control run and q_v in the WeakW run, but the differences are not strong enough to be conclusive here. Averaging over multiple clouds at different points in their life cycles resulted in highly variable correlation strengths, particularly in the LES data. The simple model showed more separation between q_c and q_v but still retained a large variance. LES profiles of high total water path showed more dramatic changes in the total water concentration and the circulation strength in the WeakW run before and after cloud formation.

In order to continue this work, we would ideally like to simulate this sugar-to-flowers scenario with a domain mean reduction in relative humidity in the same manner as the WeakW run here. From this we can ascertain a more robust understanding on whether the relationships between cloud size and moisture concentrations as seen here hold true. While some conclusions can be drawn about the nature of moisture distributions and their effect on cloud size, more data is needed on the vertical velocity to properly compare these effects to the strength of circulations.

Chapter 5

Conclusions and Future Work

In this thesis we have attempted to build a simple cloud model that captures the essential physics of shallow tradewind cumulus as they self-organize into the patterns known as sugar, gravel, and flowers. After testing hundreds of iterations of different model structures and parameter settings, assessing terabytes of model output for organizational accuracy, and reviewing thousands of satellite images to understand variations in these patterns, we present two different models that are capable of evolving the patterns in question between them. This chapter provides an overview of information gained and lessons learned in the pursuit of this goal, summarizing and expanding upon the conclusions of chapters 2-4, and answering our initial question of whether or not simple cloud models are a viable method for assessing the underlying processes of self-organization, particularly when compared to an LES. We will close with a discussion on future directions for this research and provide any final comments on the work.

5.1 Conclusions from Model A Using Cloud Drop Number Concentration

Our first model contained prognostic equations for vertical velocity w, cloud water concentration q_c, rain water concentration q_r, and cloud drop number concentration n_c, and was realistically able to capture two of the three patterns that we set out to simulate, answering our first research question from section 1.4. Sugar and gravel were readily apparent in their organization, both from a visual analysis and statistical comparisons to real world cloud images. In addition, comparing these patterns to the typical cloud size distributions that we see in the atmosphere yielded similar results, with cloud number dropping off exponentially with diameter (Benner and Curry 1998). Flowers on the other hand presented a challenge, as the model was capable of initiating condensation at a point around the strong central updraft but not advecting it far enough outwards to form a true flower of appropriate size. As the strength of the advection terms clearly showed that the model was attempting to simulate some sort of circulation through the cloud top advection, we conclude that this model is in effect "halfway there", i.e. it is able to simulate only one half of the circulation.

The failure of this model to form realistic flowers therefore gives us valuable insight into what is necessary to simulate them in a coupled simple model. In particular, it is the lack of an implicit vertical coordinate that prevents such models from being used for this purpose. That is not to say that vertical gradients of motion cannot be derived; the second model is proof of the opposite. It simply requires an understanding of the dynamics involved around flowers and some creativity on the part of the modeler to apply this knowledge to the variables at hand.

All three cloud patterns were observed to “pulse” over their life cycle, with oscillations in sugar being the most apparent as clouds form and dissipate. While this may be an artifact of deliberately finding chaotic oscillatory solutions in a simple model, this behavior does have a basis in the natural world. Coupled oscillators are mathematically driven to synchronize even in the most unexpected of place, such as in the famous example of fireflies blinking in unison, and observed shallow cumulus exhibit this pulsing behavior as well (Strogatz and Stewart 1993; Heus et al. 2009). That we see this behavior in our simple model therefore lends credence to its realism.

Isolating the different processes in the three patterns revealed which ones were critical in a simple model to form clouds and induce them to organize into distinct patterns in conjunction with research question 2. For sugar, these terms were the environmental buoyancy, gravitational drag, condensation, precipitation depletion, precipitation influx, entrainment, and cloud drop activation. On the whole, these terms make complete sense in being able to form sugar compared to what we know of their environment. Condensation and precipitation are the ingredients common to any simple model based on the predator-prey relationship and will remain important in any model presented in this work. Meanwhile the more unstable boundary layer as noted by Bony et al in the case of small clouds provides a suitable environment for these clouds to grow, particularly in the absence of driving circulations (Bony et al. 2020). Entrainment also plays a larger role when circulations are weakened as cloud base mixing is not mitigated by the convergence of moisture and therefore results in drying of the layer (Vogel et al. 2022). Compared to sugar, latent heating and cloud top advection are necessary for this model to form our pseudo-flowers. The deeper flowers have more vigorous updrafts, even at this size, which makes strong latent heat release necessary for enhancing these motions. Gravel, meanwhile, at a real-world size falling in between that of sugar and flowers, would by nature be expected to exhibit characteristics of both and is the result that we see here. The main driver of this pattern is the coupling of the vertical velocity, which we can link to that of the leading edge of a gust front propagating outward from a cold pool.

5.2 Conclusions from Model B Using Water Vapor Concentration

The analysis of our first model found that simulating cloud drop number concentration did not have a significant impact on the resulting pattern; rather it almost seemed to be a hindrance in managing a variable with such radically different orders of magnitude to the others and was the only variable that did not evolve realistically. Because we also needed another prognostic variable with strong impacts near cloud base and desired to keep the model as simple as possible, the decision was made to switch the cloud drop number concentration for water vapor concentration q_v. The atmospheric profile in the tradewind boundary layer shows that moisture is most concentrated below cloud in the form of vapor (Narenpitak et al. 2021), allowing us to adapt the coupling to show convergence/divergence of water vapor at cloud base as a function of the vertical velocity gradient. This thus completes the implicit vertical circulations that the first model was missing and results in flowers that now grow to a proper size while retaining simulations of sugar and gravel, updating our conclusions of research questions 1 and 2.

Sugar in this new model, like the previous one, was composed of small and randomly distributed clouds with realistic levels of cloud water and no precipitation. The pulsing behavior continues to be present here, quickly synchronizing despite the very low coupling strength. The number distribution of cloud diameter fits equally as well for the small cloud sizes most representative of sugar. The biggest change between the two models in simulating sugar was in the initial conditions, which were required to be more moist to evolve sugar in the second model. This may be a function of the boundary layer being shallower, which would compress equivalent moisture from the gravel and flowers scene into a smaller space (Narenpitak et al. 2021). Conversely it may also be related to providing the model with enough moisture to form clouds as it spins up and finds a stable oscillation. The parameter settings for sugar were comparable to that from our first model.

Gravel in the second model covers less of the domain than it did in the first and exhibits the same pulsing behavior as sugar, but it continues to have the clear arc-like structures that characterize its association with cold pool boundaries. Cloud sizes are in-line with our observations, as is the size distribution. Gravel once again formed as a function of strong vertical velocity diffusion and a deeper boundary layer, while also requiring enhanced condensation and cold pools with weaker coupling at the beginning of the model run until the pattern was able to stabilize. While the second model was able to reproduce sugar and gravel in a comparable manner to both the first model as well as observed clouds in the trades, it is also now capable of producing flowers of a more realistic size. An analysis of the advection across a developing flower clearly showed the advection terms successfully reproducing the shallow mesoscale circulation that characterizes these clouds in the real atmosphere. Flowers in this model formed in a deeper boundary layer with a stronger inversion layer and were observed to have much stronger latent heating rates associated with them.

5.3 Conclusions from Comparing Our Simple Model with an LES

The second simple model utilizing q_v was tested against LES model runs by Narenpitak et al to measure the degree to which the simple model could produce realistic and interpretable results and provides an evaluation of research question 3 (Narenpitak et al. 2021). An observed sugar-to-flowers event was simulated by the LES, both as an unchanged run and one in which the domain mean vertical velocity was reduced by 50%. Simulating the same type of environment in the simple model showed enough similarities in the response that lead us to believe a simple model can indeed produce viable results, even if only to identify scenarios for later further scrutiny. In this case, both models saw a decrease in cloud size and a delay in their formation time as a result of the decrease in vertical velocity. From there the simple model can be used for what the LES cannot, namely eliminating whole processes to test the pattern sensitivity, which we can see resulted in an enhancement of the impacts of the reduction in w.

In terms of the importance of moisture and circulation strength on the flower size, we can conclude that moisture is the best predictor at heights in the mid to upper layers of the cloud. This was true for both cloud water and, surprisingly, water vapor concentrations as well. In addition, we can see the impacts that the boundary layer decoupling has on the profile of cloud and water vapor as well as the depth of the circulation, as near-surface water vapor became much better correlated with cloud size in the weak w run where the circulation extended all the way through the layer. We can also conclude that both moisture and circulation strength are important predictors of cloud size changes, with correlations reaching 0.8 and greater for both. What we cannot conclude, unfortunately, is whether one process is a more important predictor than the other, as the variances were large enough to overlap at most points. In order to reach more discerning conclusions about the differences in moisture versus circulation strength and their impacts on cloud size, we would need to run an additional set of experiments to test the pattern's response to a reduction in domain mean moisture content in the same manner as the weak w experiments, thus allowing us to compare cloud size changes as the environment is altered.

5.4 Overarching Conclusions

At the beginning of this thesis we asked the question of if a simple cloud model could be used to simulate self-organizing patterns of shallow cumulus in the trade winds. After all the work presented here, we believe that the answer to that question is an emphatic yes. We presented two such models: the first that was able to simulate two patterns, and the second that built from it to simulate three. The fact that a nonlinear dynamical system of four equations, all developed to be as uncomplicated as possible in the way that processes are parameterized, was able to reproduce such wildly different patterns solely by placing them in different environments, is honestly astounding, and we confess to many days of skepticism on whether a simple model was the correct tool for the job. Instead, after many many different combinations of terms and parameterizations, a model emerged that was capable of simulating sugar, gravel, and flowers through the most basic of methods: a series of coupled grid boxes exchanging moisture and momentum. We feel that this is a good omen towards being able to represent shallow cumulus patterns in climate models, as this work shows that interactions do not need to be complicated to induce self-aggregation.

In terms of the minimum processes necessary to include in a simple model, we find that there is significant overlap in the critical terms calculated from both models using n_c and q_v. Both models required gravitational drag, latent heating, condensation, precipitation, vertical velocity diffusion, and cloud top coupling to create at least one of the three patterns. This agreement between the two models strengthens our belief that these are essential processes to include in a simple model if one wants to simulate self-organization of shallow cumulus. In fact, many of these terms were also adapted from prior modeling studies. As to simulating the specific patterns of sugar, gravel, and flowers, the critical difference in gaining all three patterns was the addition of coupling at cloud base in addition to at cloud top, with the two processes a function of different variables so that they do not cancel each other out. We know from observational and LES studies how critical the formation of mesoscale circulations are in driving moisture aggregation, and that result holds true for simple models as well. There are many processes that can be simplified or estimated and still produce a generally realistic outcome, such as defining rain sedimentation as purely a function of the amount of rain water present in the cloud. The vertical circulation is one such process that appears cannot be parameterized into a single entity.

5.5 Future Work

This thesis is a foundational work in the patterning of shallow cumulus using a simple model and as such, there are multiple avenues of research with which to direct our future efforts. The most fundamental is the continued development of our model to better parameterize certain terms. We found in this study that processes such as condensation and precipitation were critical to include in a simple model. The idea that water vapor condenses to form clouds then precipitates out is not a groundbreaking result, and terms such as these are simple to understand and adapt their relationship to the variables at hand. We know for instance that condensation rate is related to supersaturation of the local environment and it is a short jump to subsequently link that to available concentrations of water vapor (Rogers and Yau 1989). The model handles most of these terms quite well for what they are required to do. However, several processes in the model defied our expectations by not appearing to affect the resulting pattern. In addition, there are processes which could not be adapted to the simple model due to conflicting with the overly simple nature of the model. The terms we would like to address in future updates include entrainment rate, cold pool formation, and background wind flow. Improved parameterizations of these three terms may reveal a heretofore hidden relationship in the way that clouds self-organize.

The second model already links the entrainment rate to the vertical velocity, simply assuming that larger vertical motions induce stronger mixing, particularly at the top and bottom of the cloud. However entrainment in nature is unsurprisingly a much more complex process, and there are several places in the model where entrainment could theoretically play a larger role and influence the different patterns. First, while entrainment rate is related to the vertical velocity, it is also a function of the surface buoyancy flux and exhibits a strong diurnal cycle (Vogel and Bony 2020; Vogel et al. 2022). This could be included in the model as simply a time-varying parameter in place of a constant, with changes a function of user-defined time of day. More interestingly, entrainment rate is found to have an impact on autoconversion and accretion rates, making them more efficient due to broadening of the droplet size distributions and speeding up the production of precipitation

(Cooper et al. 2013). It is unclear whether this effect is large enough to change precipitation distributions and alter pattern formation times in the simple model, but it is a curious thought. Finally, the current understanding that lateral mixing is more common than cloud top mixing does not change the dependence on vertical velocity (as a proxy for the strength of horizontal motions), but the presence of subsiding shells outside the cloud means that the character of entrained air may be different from that in the environment at lower levels and result in more pronounced drying at cloud edges (de Rooy et al. 2013).

Perhaps the most perplexing result from our simple cloud model is the lack of effect that the cold pool term has on structuring the vertical velocity. While it is well understood that cold pools do not drive, nor even impact, the initial formation of flowers (Bretherton and Blossey 2017), current evidence shows that cold pools help to organize flowers after the fact, restructuring the primary updraft into an arc at the downstream edge (Dauhut et al. 2023). This implies a stronger effect between both the cold pool and coupling terms affecting the vertical velocity in our model than any of our patterns show. One way to improve this term may be to link it to changes in water vapor. Observations show that cold pools are associated with lowered surface specific humidity (Zuidema et al. 2012; Vogel et al. 2021). Any air parcels that pass through this region, namely those transporting moisture from the ocean surface to the cloud, will experience some drying. In addition we may find a way in which to strengthen the current parameterized version of the cold pool term in conjunction with the vertical velocity advection, forcing the terms to have more of an impact.

Adding a background wind flow was something of a problem throughout this project due to the mechanics of the simple model. Because there is no vertical coordinate, any background wind flow added to the model will affect every level equally, which runs counter to the documented impacts of background winds in the literature. Bony et al notes that the near-surface wind speed was a discriminating factor in determining the cloud pattern that formed (Bony et al. 2020). Meanwhile K.C Helfer has done extensive work on the impact of different types of vertical wind shear on tradewind cumulus. Backward shear, where surface easterlies transition to upper level westerlies, leads to weaker surface winds and a shallower boundary layer, producing clouds that are moister, shallower, and wider (Helfer et al. 2020). Forward shear, in which the wind strengthens with height, has the effect of strengthening subcloud circulations and promoting deeper clouds (Helfer and Nuijens 2021). These results imply that adding a background wind flow to our simple model is a necessary next step in analyzing pattern formation. While the first simple model has no vertical coordinate with which to distinguish impacts, the second may be able discriminate between upper and lower level winds using the advection terms at cloud top and cloud base.

There is perhaps one last thought that we have been avoiding for the entirety of this project: whatever happened to fish? Early in the work the decision was made to forego this pattern due to its association with the large-scale features of gust fronts, which our simple model was incapable of handling. Now that we have shown that it is possible to realistically simulate the substantially different patterns of sugar, gravel, and flowers, it is worth revisiting adapting our model to handle the input of synoptic-scale features in the form of large-scale forcings to produce fish. We have already seen how manually altering the domain wind speeds affects the mesoscale circulations controlling flowers, and adding such a large feature to the domain will be a challenge. So little is known about fish as they remain largely unexplored in the literature, making simple model simulations a particularly interesting line of future research as we attempt to diagnose their environmental drivers.

Appendix A

Supplementary Information for Chapter 2

A.1 Nondimensionalization of n_c model

The following nondimensionalization relationships are used for this model:

$$t = t^*\tau,\ w = w^*X,\ q_c = Q^*Y,\ q_r = Q^*Z,\ q_v = Q^*V$$
$$\frac{dM}{dz} = \epsilon_M \frac{M}{H}$$

In the following we start from each dimensional equation and demonstrate the non-dimensionalization in a step-by-step manner. We omit the coupling terms for clarity.

Vertical Velocity

$$\begin{aligned}
\frac{dw}{dt} &= -w\frac{dw}{dz} - \frac{g}{\rho}(q_c + 0.1q_r) + f_w + \frac{d_3 d_5}{\rho}w|w|q_c - \frac{d_4}{\rho}q_r - d_p w^3 \\
\frac{dw}{dt} &= -\epsilon_w w\frac{w}{H} - \frac{g}{\rho}(q_c + 0.1q_r) + f_w + \frac{d_3 d_5}{\rho}w|w|q_c - \frac{d_4}{\rho}q_r - d_p w^3 \\
\frac{w^*}{t^*}\frac{dX}{d\tau} &= -\epsilon_w\frac{w^{*2}}{H}X^2 - \frac{gQ^*}{\rho}(Y + 0.1Z) + F_w + \frac{d_3 d_5 w^{*2} Q^*}{\rho}X|X|Y - \frac{d_4 Q^*}{\rho}Z - d_p w^{*3}X^3 \\
\frac{dX}{d\tau} &= -\epsilon_w\frac{w^* t^*}{H}X^2 - g\frac{t^* Q^*}{w^*\rho}(Y + 0.1Z) + F_w\frac{t^*}{w^*} + \frac{d_3 d_5 t^* Q^* w^*}{\rho}X|X|Y - d_4\frac{Q^* t^*}{w^*\rho}Z \\
&\quad - d_p w^{*2} t^* X^3
\end{aligned}$$

We have six dimensionless parameters that determine the dynamical regime of the vertical velocity. These are:

$$\begin{aligned}
\alpha_1 &= \frac{\epsilon_w w^* t^*}{H} \\
\alpha_2 &= \frac{g t^* Q^*}{w^* \rho} \\
\beta_1 &= F_w \frac{t^*}{w^*} \\
\alpha_3 &= \frac{d_3 d_5 t^* Q^* w^*}{\rho} \\
\alpha_4 &= d_4 \frac{Q^* t^*}{w^* \rho} \\
\alpha_p &= d_p {w^*}^2 t^*
\end{aligned}$$

This gives the nondimensionalized equation for vertical velocity:

$$\frac{dX}{d\tau} = -\alpha_1 X^2 - \alpha_2 (Y + 0.1Z) + \beta_1 + \alpha_3 X|X|Y - \alpha_4 Z - \alpha_p X^3$$

Cloud Water Concentration

$$\begin{aligned}
\tfrac{dq_c}{dt} &= d_5 w q_c - d_6 \frac{q_c^3}{n_c^2} - d_7 q_c q_r - E \\
\tfrac{Q^*}{t^*} \tfrac{dY}{d\tau} &= d_5 Q^* w^* XY - d_6 \frac{{Q^*}^3}{{N^*}^2} \frac{Y^3}{N^2} - d_7 {Q^*}^2 YZ - E \\
\tfrac{dY}{d\tau} &= d_5 t^* w^* XY - d_6 \frac{{Q^*}^2 t^*}{{N^*}^2} \frac{Y^3}{N^2} - d_7 Q^* t^* YZ - E \frac{t^*}{Q^*} \\
\tfrac{dY}{d\tau} &= \alpha_5 XY - \alpha_6 \frac{Y^3}{N^2} - \alpha_7 YZ - \beta_2
\end{aligned}$$

Rain Water Concentration

$$\begin{aligned}
\tfrac{dq_r}{dt} &= d_6\frac{q_c^3}{n_c^2} + d_7 q_c q_r - d_8 q_r - E + P \\
\tfrac{Q^*}{t^*}\tfrac{dZ}{d\tau} &= d_6\frac{Q^{*3}}{N^{*2}}\frac{Y^3}{N^2} + d_7 Q^{*2} YZ - d_8 Q^* Z - E + P \\
\tfrac{dZ}{d\tau} &= d_6\frac{Q^{*2}t^*}{N^{*2}}\frac{Y^3}{N^2} + d_7 Q^* t^* YZ - d_8 t^* Z - E\frac{t^*}{Q^*} + P\frac{t^*}{Q^*} \\
\tfrac{dZ}{d\tau} &= \alpha_6\frac{Y^3}{N^2} + \alpha_7 YZ - \alpha_8 Z - \beta_2 + \beta_3
\end{aligned}$$

Cloud Drop Number Concentration

$$\begin{aligned}
\tfrac{dn_c}{dt} &= d_9(n_a - n_c) - d_{10} q_c^2 - d_7 n_c q_r \\
\tfrac{N^*}{t^*}\tfrac{dN}{d\tau} &= d_9(n_a - N^*N) - d_{10} Q^{*2} Y^2 - d_7 N^* Q^* NZ
\end{aligned}$$

Here we take $n_a = N^*$

$$\begin{aligned}
\frac{dN}{d\tau} &= d_9 t^*(1-N) - d_{10}\frac{Q^{*2}t^*}{N^*}Y^2 - d_7 Q^* t^* NZ \\
\frac{dN}{d\tau} &= \alpha_9(1-N) - \alpha_{10}Y^2 - \alpha_7 NZ
\end{aligned}$$

Nondimensionalized System of Equations The model consists of the following 4 nondimensionalized equations:

$$\begin{aligned}
\frac{dX}{d\tau} &= -\alpha_1 X^2 - \alpha_2(Y + 0.1Z) + \beta_1 + \alpha_3 X|X|Y - \alpha_4 Z - \alpha_p X^3 \\
\frac{dY}{d\tau} &= \alpha_5 XY - \alpha_6\frac{Y^3}{N^2} - \alpha_7 YZ - \beta_2 \\
\frac{dZ}{d\tau} &= \alpha_6\frac{Y^3}{N^2} + \alpha_7 YZ - \alpha_8 Z - \beta_2 + \beta_3 \\
\frac{dN}{d\tau} &= \alpha_9(1-N) - \alpha_{10}Y^2 - \alpha_7 NZ
\end{aligned}$$

Table A.1: n_c nondimensionalization parameters

Parameter	Definition	Physical Meaning
α_1	$\frac{\epsilon_w w^* t^*}{H}$	Vertical Advection
α_2	$\frac{g Q^* t^*}{w^* \rho}$	Gravitational Drag
α_3	$\frac{d_3 d_5 t^* Q^* w^*}{\rho}$	Latent Heating
α_4	$\frac{d_4 Q^* t^*}{w^* \rho}$	Cold Pools
α_5	$d_5 t^* w^*$	Condensation Rate
α_6	$d_6 \frac{{Q^*}^2 t^*}{{N^*}^2}$	Autoconversion Rate
α_7	$d_7 Q^* t^*$	Accretion Rate
α_8	$d_8 t^*$	Precipitation Rate
α_9	$d_9 t^*$	n_c Activation Rate
α_{10}	$d_{10} \frac{{Q^*}^2 t^*}{N^*}$	n_c Condensation Rate
α_p	$d_p {w^*}^2 t^*$	Turbulent Diffusion
β_1	$F_w \frac{t^*}{w^*}$	Environmental Instability
β_2	$E \frac{t^*}{Q^*}$	Entrainment Rate
β_3	$P \frac{t^*}{Q^*}$	Precipitation Influx Rate

A.2 Summary of parameters in n_c model

This system of equations is subject to 11 internal and 3 external non-dimensional model parameters listed in table A.1.

A.3 Additional plots

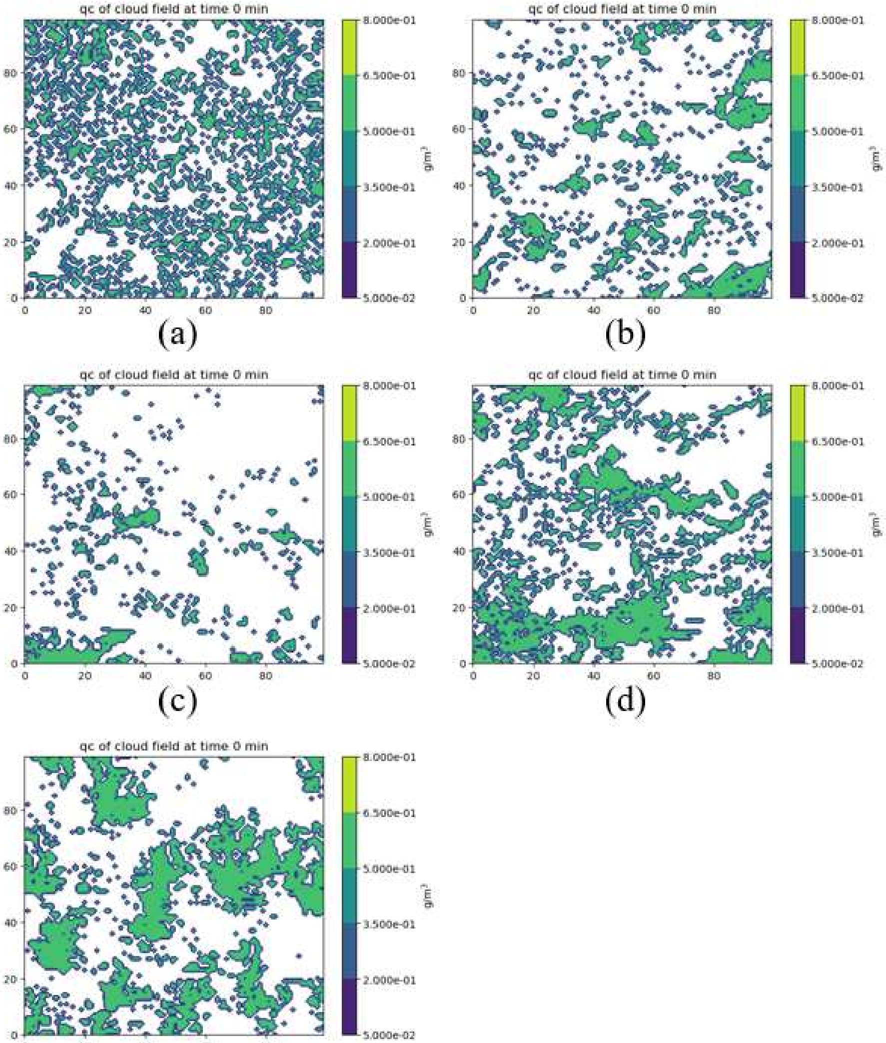

(a) (b) (c) (d) (e)

Figure A.1: All sets of initial conditions using the first simple model.

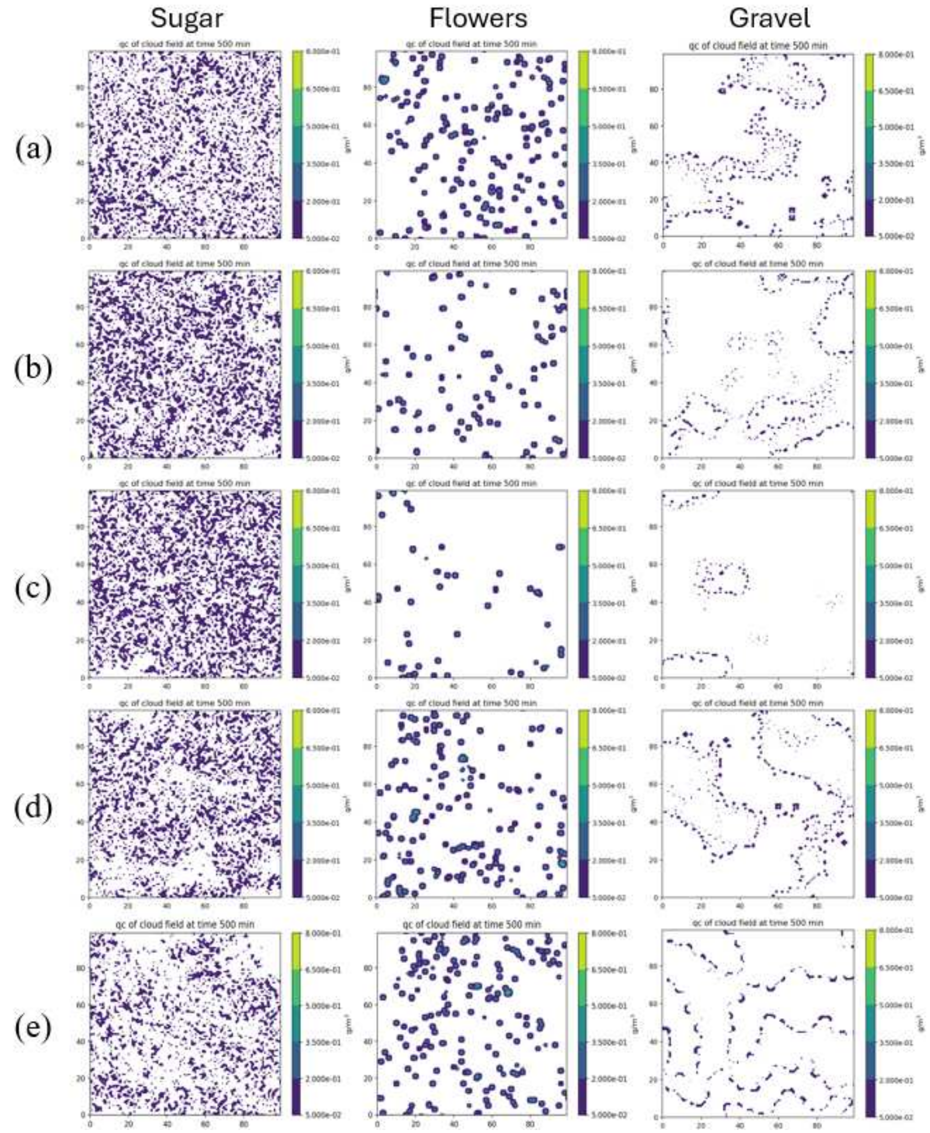

Figure A.2: Model output at run conclusion for each set of initial conditions shown in figure A.1 using the first simple model.

Appendix B

Supplementary Information for Chapter 3

B.1 Nondimensionalization of q_v model

The following nondimensionalization relationships are used for this model:

$$t = t^* \tau,\ w = w^* X,\ q_c = Q^* Y,\ q_r = Q^* Z,\ q_v = Q^* V$$

$$\frac{dM}{dz} = \epsilon_M \frac{M}{H}$$

In the following we start from each dimensional equation and demonstrate the non-dimensionalization in a step-by-step manner. We omit the coupling terms for clarity.

Vertical Velocity

$$\begin{aligned}
\frac{dw}{dt} &= -\epsilon_w \frac{w^2}{H} - \frac{g}{\rho}(q_c + q_r) + f_w + \frac{d_3 d_5}{\rho} w|w| q_v - \frac{d_4}{\rho} q_r - d_p w^3 + 0.61 \frac{g}{\rho} q_v^{'} \\
\frac{w^*}{t^*}\frac{dX}{d\tau} &= -\epsilon_w \frac{w^{*2}}{H} X^2 - \frac{gQ^*}{\rho}(Y + Z) + f_w + \frac{d_3 d_5 w^{*2} Q^*}{\rho} X|X|V - \frac{d_4 Q^*}{\rho} Z - d_p w^{*3} X^3 \\
&\quad + 0.61 \frac{gQ^*}{\rho} V' \\
\frac{dX}{d\tau} &= -\epsilon_w \frac{t^* w^*}{H} X^2 - \frac{gQ^* t^*}{w^* \rho}(Y + Z) + f_w \frac{t^*}{w^*} + \frac{d_3 d_5 Q^* t^* w^*}{\rho} X|X|V - d_4 \frac{Q^* t^*}{w^* \rho} Z \\
&\quad - d_p t^* w^{*2} X^3 + 0.61 \frac{gQ^* t^*}{w^* \rho} V'
\end{aligned}$$

We have seven dimensionless parameters that determine the dynamical regime of the vertical velocity. These are:

$$\begin{aligned}
\alpha_1 &= \frac{\epsilon_w t^* w^*}{H} \\
\alpha_2 &= \frac{g Q^* t^*}{w^* \rho} \\
\beta_1 &= f_w \frac{t^*}{w^*} \\
\alpha_3 &= \frac{d_3 d_5 Q^* t^* w^*}{\rho} \\
\alpha_4 &= d_4 \frac{Q^* t^*}{w^* \rho} \\
\alpha_p &= d_p t^* {w^*}^2 \\
\alpha_9 &= \frac{q Q^* t^*}{w^* \rho}
\end{aligned} \tag{B.1}$$

This gives the nondimensionalized equation for vertical velocity:

$$\frac{dX}{d\tau} = -\alpha_1 X^2 - \alpha_2 (Y + Z) + \beta_1 + \alpha_3 X|X|V - \alpha_4 Z - \alpha_p X^3 + 0.61 \alpha_9 V^{'}$$

Cloud Water Concentration

$$\begin{aligned}
\tfrac{dq_c}{dt} &= d_5 w (h_{v,1} q_v + h_{v,2} q_c) - d_6 q_c^2 - d_7 q_c q_r - E|w| + d_{10} h_{v,2} w \\
\tfrac{Q^*}{t^*} \tfrac{dY}{d\tau} &= d_5 Q^* w^* X (H_{v,1} V + h_{v,2} Y) - d_6 {Q^*}^2 - d_7 {Q^*}^2 Y Z - E w^* |X| + d_{10} h_{v,2} w^* X \\
\tfrac{dY}{d\tau} &= d_5 t^* w^* X (h_{v,1} V + h_{v,2} Y) - d_6 Q^* t^* Y^2 - d_7 Q^* t^* Y Z - E \frac{t^* w^*}{Q^*} |X| + d_{10} h_{v,2} \frac{t^* w^*}{Q^*} X \\
\tfrac{dY}{d\tau} &= \alpha_5 X (h_{v,1} V + h_{v,2} Y) - \alpha_6 Y^2 - \alpha_7 Y Z - \beta_2 |X| + \alpha_{10} h_{v,2} X
\end{aligned}$$

Rain Water Concentration

$$\begin{aligned}
\tfrac{dq_r}{dt} &= d_6 q_c^2 + d_7 q_c q_r - d_8 q_r + P \\
\tfrac{Q^*}{t^*}\tfrac{dZ}{d\tau} &= d_6 Q^{*2} Y^2 + d_7 Q^{*2} YZ - d_8 Q^* Z + P \\
\tfrac{dZ}{d\tau} &= d_6 Q^* t^* Y^2 + d_7 Q^* t^* YZ - d_8 t^* Z + P\frac{t^*}{Q^*} \\
\tfrac{dZ}{d\tau} &= \alpha_6 Y^2 + \alpha_7 YZ - \alpha_8 Z + \beta_3
\end{aligned}$$

Water Vapor Concentration

$$\begin{aligned}
\tfrac{dq_v}{dt} &= Sw + 0.01 d_8 q_r - d_5 w(h_{v,1} q_v + h_{v,2} q_c) + E|w| \\
\tfrac{Q^*}{t^*}\tfrac{dV}{d\tau} &= Sw^* X + 0.01 d_8 Q^* Z - d_5 Q^* w^* X(h_{v,1} V + h_{v,2} Y) + Ew^*|X| \\
\tfrac{dV}{d\tau} &= S\frac{t^* w^*}{Q^*} X + 0.01 d_8 t^* Z - d_5 t^* w^* X(h_{v,1} V + h_{v,2} Y) + E\frac{t^* w^*}{Q^*}|X| \\
\tfrac{dV}{d\tau} &= \beta_4 X + 0.01\alpha_8 Z - \alpha_5 X(h_{v,1} V + h_{v,2} Y) + \beta_2 |X|
\end{aligned}$$

Nondimensionalized System of Equations The model consists of the following 4 nondimensionalized equations:

$$\begin{aligned}
\tfrac{dX}{d\tau} &= -\alpha_1 X^2 - \alpha_2 (Y + Z) + \beta_1 + \alpha_3 X|X|V - \alpha_4 Z - \alpha_p X^3 + 0.61\alpha_9 V^{'} \\
\tfrac{dY}{d\tau} &= \alpha_5 X(h_{v,1} V + h_{v,2} Y) - \alpha_6 Y^2 - \alpha_7 YZ - \beta_2 |X| + \alpha_{10} h_{v,2} X \\
\tfrac{dZ}{d\tau} &= \alpha_6 Y^2 + \alpha_7 YZ - \alpha_8 Z + \beta_3 \\
\tfrac{dV}{d\tau} &= \beta_4 X + 0.01\alpha_8 Z - \alpha_5 X(h_{v,1} V + h_{v,2} Y) + \beta_2 |X|
\end{aligned}$$

B.2 Summary of parameters in q_v model

This system of equations is subject to 11 internal and 3 external non-dimensional model parameters listed in table B.1.

Table B.1: q_v nondimensionalization parameters

Parameter	Definition	Physical Meaning
α_1	$\frac{\epsilon_w w^* t^*}{H}$	Vertical Advection
α_2	$\frac{gQ^* t^*}{w^* \rho}$	Gravitational Drag
α_3	$\frac{d_3 d_5 t^* Q^* w^*}{\rho}$	Latent Heating
α_4	$\frac{d_4 Q^* t^*}{w^* \rho}$	Cold Pools
α_5	$d_5 t^* w^*$	Condensation Rate
α_6	$d_6 Q^* t^*$	Autoconversion Rate
α_7	$d_7 Q^* t^*$	Accretion Rate
α_8	$d_8 t^*$	Precipitation Rate
α_9	$\frac{gQ^* t^*}{w^* \rho}$	n_c Activation Rate
α_{10}	$d_{10} \frac{t^* w^*}{Q^*}$	n_c Condensation Rate
α_p	$d_p {w^*}^2 t^*$	Turbulent Diffusion
β_1	$f_w \frac{t^*}{w^*}$	Environmental Instability
β_2	$E \frac{t^* w^*}{Q^*}$	Entrainment Rate
β_3	$P \frac{t^*}{Q^*}$	Precipitation Influx Rate
β_4	$P \frac{t^*}{Q^*}$	Water Vapor Uptake Rate

B.3 Additional plots

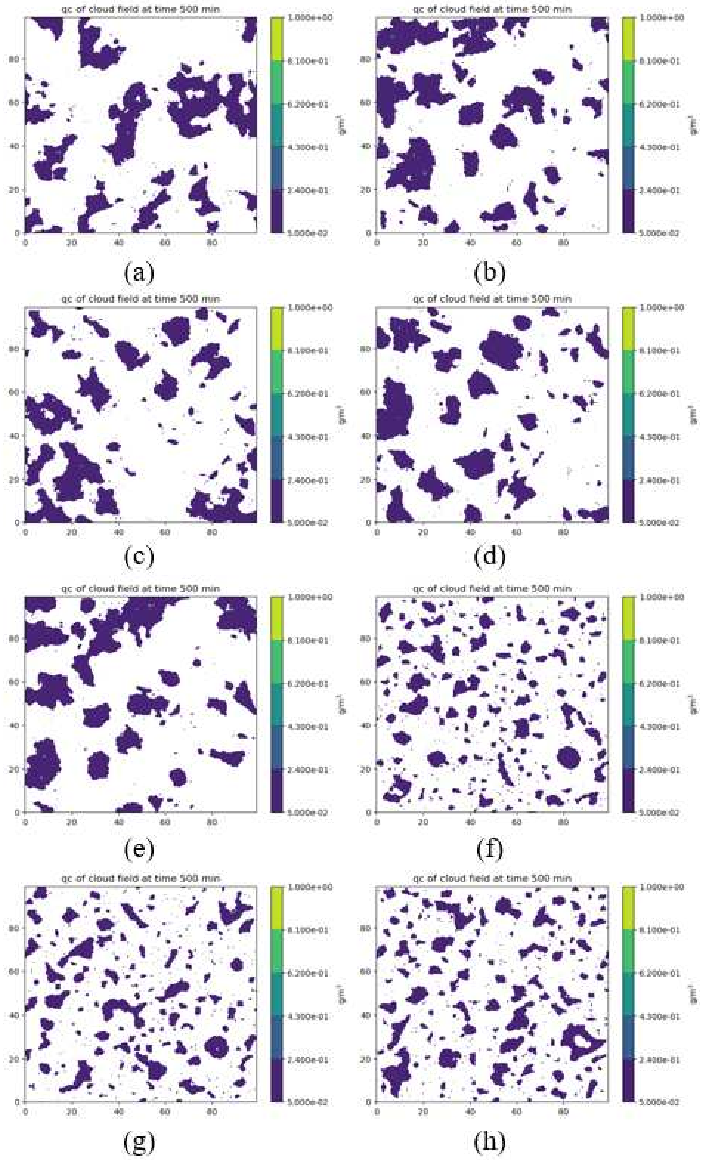

(a) (b) (c) (d) (e) (f) (g) (h)

Figure B.1: Model output at run conclusion for each set of initial conditions shown in figure 3.2 using the second simple model.

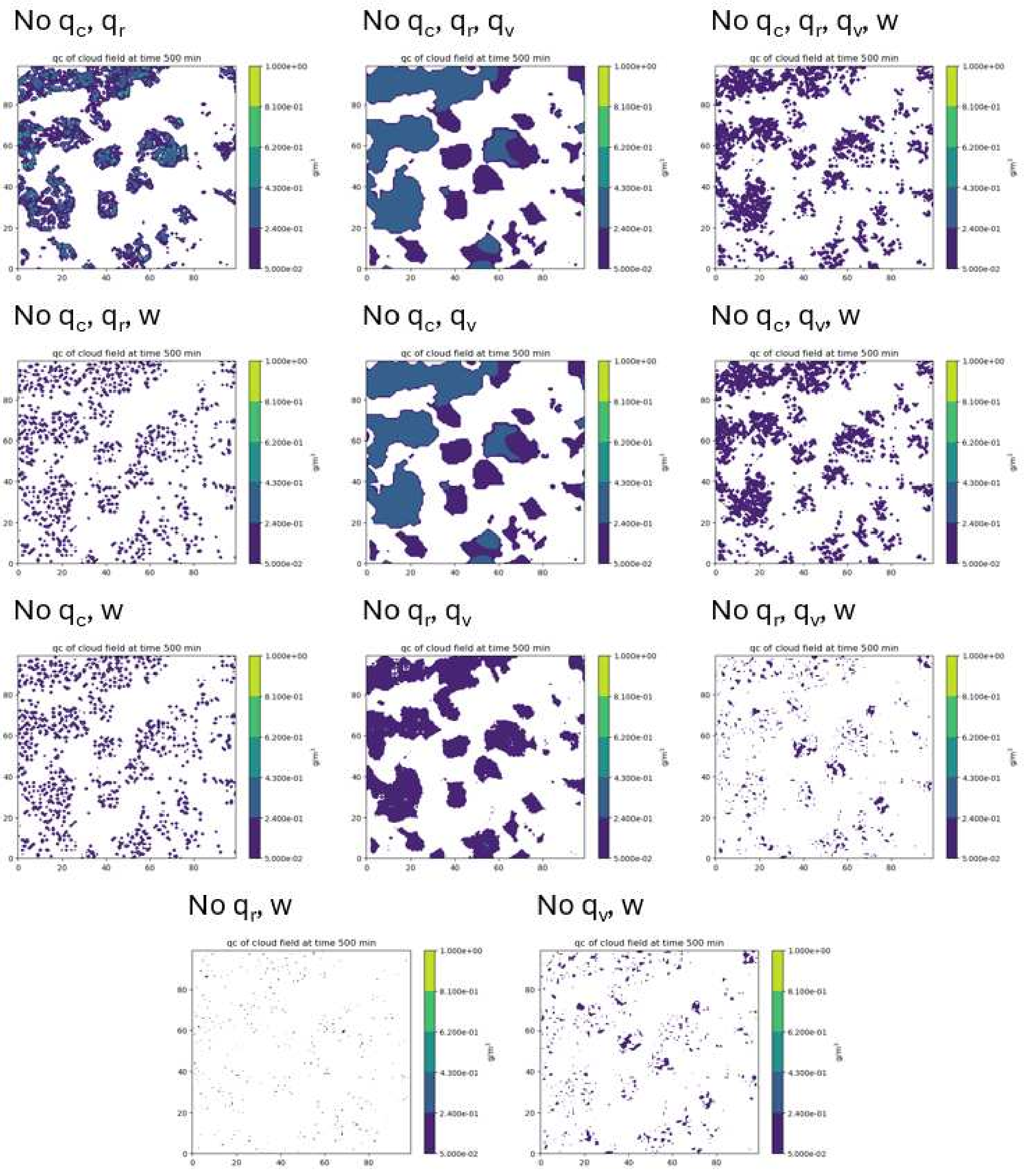

No q_c, q_r

No q_c, q_r, q_v

No q_c, q_r, q_v, w

No q_c, q_r, w

No q_c, q_v

No q_c, q_v, w

No q_c, w

No q_r, q_v

No q_r, q_v, w

No q_r, w

No q_v, w

Figure B.2: Sensitivity of flowers in the second model to each combination of coupling terms. The terms listed for each plot were removed from their respective model run.

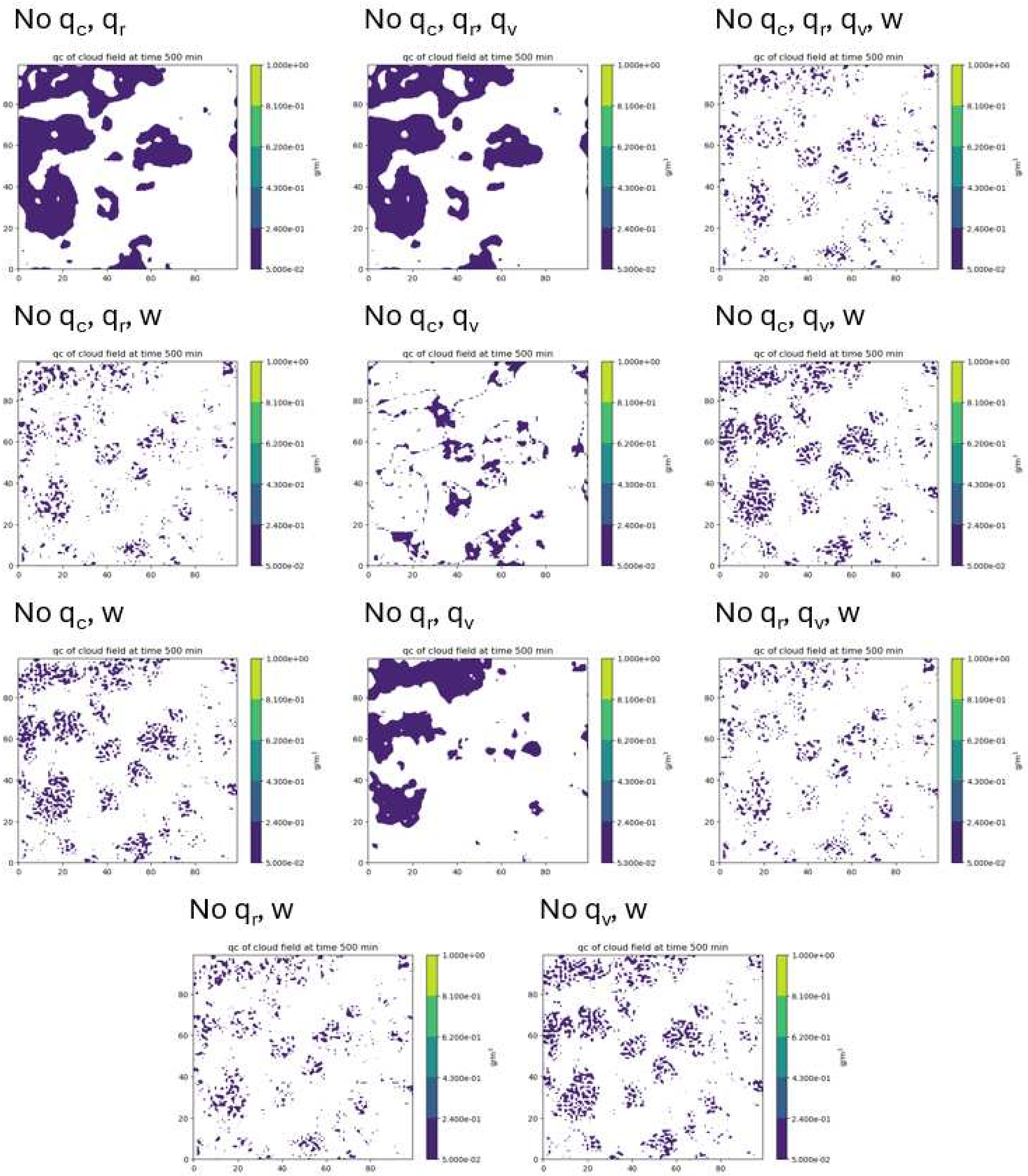

Figure B.3: Sensitivity of gravel in the second model to each combination of coupling terms. The terms listed for each plot were removed from their respective model run.

Appendix C

Supplementary Information for Chapter 4

C.1 Additional plots

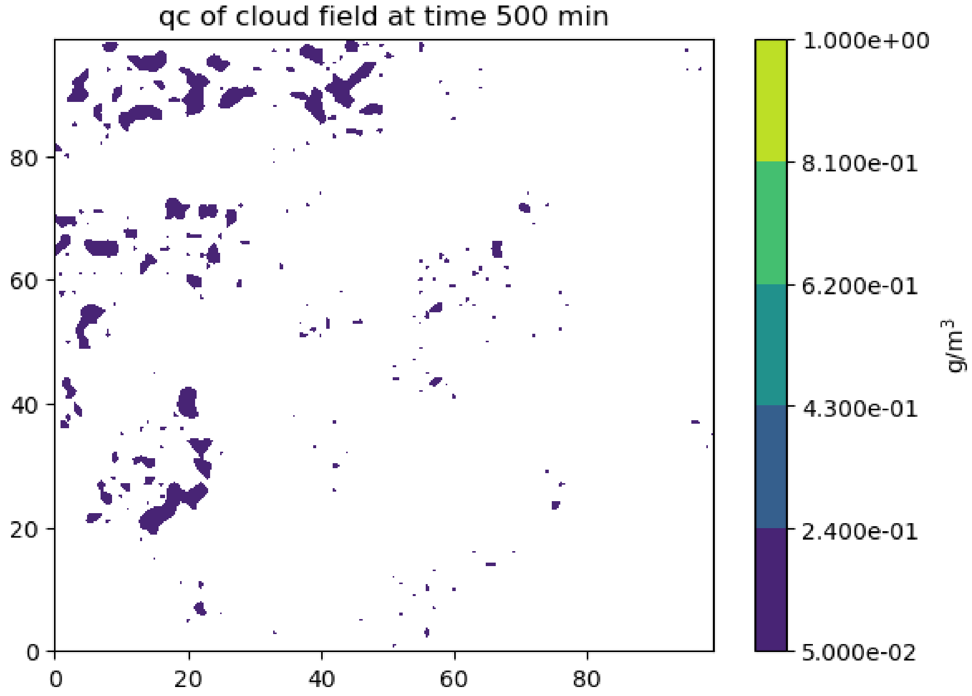

Figure C.1: Development of flowers using the second simple model with a 50% reduction in domain-mean vertical velocity for the entirety of the model run as opposed to a 10-hour period in the middle of the run as shown in figure 4.3.

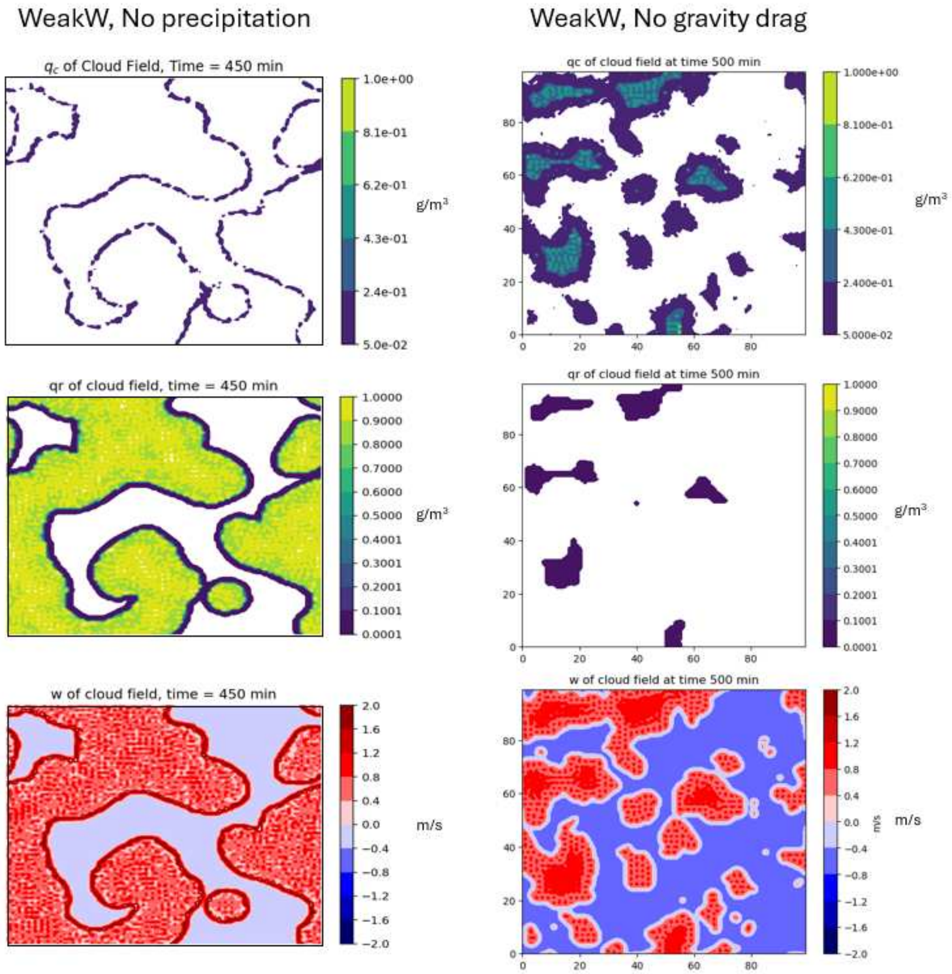

Figure C.2: WeakW output in the absence of rainwater removal (left) and gravitational drag of liquid water (right).

Bibliography

Alinaghi, P., Janssens, M., Choudhury, G., Goren, T., Siebesma, A. P., and Glassmeier, F. (2024a). Shallow cumulus cloud fields are optically thicker when they are more clustered. *Quarterly Journal of the Royal Meteorological Society*.

Alinaghi, P., Siebesma, A. P., Jansson, F., Janssens, M., and Glassmeier, F. (2024b). External drivers and mesoscale self-organization of shallow cold pools in the trade-wind regime. *Journal of Advances in Modeling Earth Systems*, 17.

Anshu and Dubey, B. (2023). Spatiotemporal dynamics of a multi-delayed predator-prey system with variable carrying capacity. *Chaos*, 33.

Benner, T. C. and Curry, J. A. (1998). Characteristics of small tropical cumulus clouds and their impact on the environment. *Journal of Geophysical Research*, 103:28753–28767.

Berryman, A. A. (1992). The origins and evolution of predator-prey theory. *Ecology*, 73(5):1530–1535.

Birouk, M. and Gokalp, I. (2006). Current status of droplet evaporation in turbulent flows. *Progress in Energy and Combustion Science*, 32:408–423.

Bony, S. and Dufresne, J.-L. (2005). Marine boundary layer clouds at the heart of tropical cloud feedback uncertainties in climate models. *Geophysical Research Letters*, 32.

Bony, S., Schulz, H., Vial, J., and Stevens, B. (2020). Sugar, gravel, fish, and flowers: Dependence of mesoscale patterns of trade-wind clouds on environmental conditions. *Geophysical Research Letters*, 48.

Bretherton, C. and Blossey, P. (2017). Understanding mesoscale aggregation of shallow cumulus convection using large-eddy simulation. *Journal of Advances in Modeling Earth Systems*, 9:2798–2821.

Bretherton, C. S. and Wyant, M. C. (1997). Moisture transport, lower-tropospheric stability, and decoupling of cloud-topped boundary layers. *Journal of the Atmospheric Sciences*, 54:148–167.

Burgers, J. (1948). A mathematical model illustrating the theory of turbulence. *Advances in Applied Mechanics*, 1:171–199.

Chekroun, M. D., Koren, I., and Liu, H. (2020). Efficient reduction for diagnosing hopf bifurcation in delay differential systems: Applications to cloud-rain models. *Chaos: An Interdisciplinary Journal of Nonlinear Science*, 30(5):053130.

Chen, J., Hagos, S., Feng, Z., Fast, J. D., and Xiao, H. (2023). The role of cloud-cloud interactions in the life cycle of shallow cumulus clouds. *Journal of the Atmospheric Sciences*, 80:671–686.

Chen, S., Yau, M.-K., Bartello, P., and Xue, L. (2018). Bridging the condensation-collision size gap: a direct numerical simulation of continuous droplet growth in turbulent clouds. *Atmospheric Chemistry and Physics*, 18:7251–7262.

Chiu, J. C., Yang, C. K., van Leeuwen, P. J., Feingold, G., Wood, R., Blanchard, Y., Mei, F., and Wang, J. (2021). Observational constraints on warm cloud microphysical processes using machine learning and optimization techniques. *Geophysical Research Letters*, 48.

Cooper, W., Lasher-Trapp, S. G., and Blyth, A. M. (2013). The influence of entrainment and mixing on the initial formation of rain in a warm cumulus cloud. *Journal of the Atmospheric Sciences*, 70:1727–1743.

Dauhut, T., Couvreux, F., Bouniol, D., Beucher, F., Volkmer, L., Portge, V., Schafer, M., Ayet, A., Brilouet, P.-E., Jacob, M., and Wirth, M. (2023). Flower trade-wind clouds are shallow mesoscale convective systems. *Quarterly Journal of the Royal Meteorological Society*, 149:325–347.

de Rooy, W. C., Bechtold, P., Frohlich, K., Hohenegger, C., Jonker, H., Mironov, D., Siebesma, A. P., Teixeira, J., and Yano, J.-I. (2013). Entrainment and detrainment in cumulus convection: an overview. *Quarterly Journal of the Royal Meteorological Society*, 139:1–19.

Feingold, G., Balsells, J., Glassmeier, F., Yamaguchi, T., Kazil, J., and McComiskey, A. (2017). Analysis of albedo versus cloud fraction relationships in liquid water clouds using heuristis models and large eddy simulation. *Journal of Geophysical Research: Atmospheres*, 122:7086–7102.

Feingold, G. and Koren, I. (2013). A model of coupled oscillators applied to the aerosol-cloud-precipitation system. *Nonlinear Processes in Geophysics*, 20:1011–1021.

Feingold, G., Koren, I., Wang, H., Xue, H., and Brewer, W. A. (2010). Precipitation-generated oscillations in open cellular cloud fields. *Nature*, 466:849–852.

Feingold, G., Yang, S., Hardesty, R., and Cotton, W. (1997). Feasibility of retrieving cloud condensation nucleus properties from doppler cloud radar, microwave radiometer, and lidar. *Journal of Atmospheric and Oceanic Technology*, 15:1188–1195.

Fitzjarrald, D. R. and Garstang, M. (1981). Vertical structure of the tropical boundary layer. *Monthly Weather Review*, 109:1512–1526.

Forster, P., Storelvmo, T., Armour, K., Collins, W., Dufresne, J.-L., Frame, D., Lunt, D., Mauritsen, T., Palmer, M., Watanabe, M., Wild, M., and Zhang, H. (2021). The earth's energy budget, climate feedbacks, and climate sensitivity. *Climate Change 2021: The Physical Science Basis. Contribution of Working Group I to the Sixth Assessment Report of the Intergovernmental Panel on Climate Change*, pages 1022–1023.

Garay, M. J., Davies, R., Averill, C., and Westphal, J. A. (2004). Actinoform clouds: Overlooked examples of cloud self-organization at the mesoscale. *Bulletin of the American Meteorological Society*, 85:1585–1594.

George, G., Stevens, B., Bony, S., Vogel, R., and Naumann, A. K. (2023). Widespread shallow mesoscale circulations observed in the trades. *Nature Geoscience*, 16:584–589.

Haynes, J. M. and Stephens, G. L. (2007). Tropical oceanic cloudiness and the incidence of precipitation: Early results from cloudsat. *Geophysical Research Letters*, 34.

Heiblum, R. H., Altaratz, O., Koren, I., Feingold, G., Kostinski, A. B., Khain, A. P., Ovchinnikov, M., Fredj, E., Dagan, G., Pinto, L., Yaish, R., and Chen, Q. (2016a). Characterization of cumulus cloud fields using trajectories in the center of gravity versus water mass phase space: 1. cloud tracking and phase space description. *Journal of Geophysical Research: Atmospheres*, 121:6336–6355.

Heiblum, R. H., Altaratz, O., Koren, I., Feingold, G., Kostinski, A. B., Khain, A. P., Ovchinnikov, M., Fredj, E., Dagan, G., Pinto, L., Yaish, R., and Chen, Q. (2016b). Characterization of cumulus cloud fields using trajectories in the center of gravity versus water mass phase space: 2. aerosol effects on warm convective clouds. *Journal of Geophysical Research: Atmospheres*, 121:6356–6373.

Helfer, K. and Nuijens, L. (2021). The morphology of simulated trade-wind convection and cold pools under wind shear. *Journal of Geophysical Research: Atmospheres*, 126.

Helfer, K., Nuijens, L., de Roode, S., and Siebesma, A. (2020). How wind shear affects trade-wind cumulus convection. *Journal of Advances in Modeling Earth Systems*, 12.

Heus, T., Jonker, H. J., den Akker, H. E. V., Griffith, E., Koutek, M., and Post, F. H. (2009). A statistical approach to the life cycle analysis of cumulus clouds selected in a virtual reality environment. *Journal of Geophysical Research*, 114.

Heus, T. and Jonker, H. J. J. (2008). Subsiding shells around shallow cumulus clouds. *Journal of the Atmospheric Sciences*, 65:1003–1018.

Hirt, M., Craig, G. C., Schafer, S. A. K., Savre, J., and Heinze, R. (2020). Cold-pool-driven convective initiation: using causal graph analysis to determine what convection-permitting models are missing. *Quarterly Journal of the Royal Meteorological Society*, 146:2205–2227.

Janssens, M., Arellano, J. V.-G. D., van Heerwaarden, C. C., de Roode, S. R., Siebesma, A. P., and Glassmeier, F. (2023). Nonprecipitating shallow cumulus convection is intrinsically unstable to length scale growth. *Journal of the Atmospheric Sciences*.

Jansson, F., Janssens, M., Gronqvist, J. H., Siebesma, A. P., Glassmeier, F., Attema, J., Azizi, V., Satoh, M., Sato, Y., Schulz, H., and Kolling, T. (2023). Cloud botany: Shallow cumulus clouds in an ensemble of idealized large-domain large-eddy simulations of the trades. *Journal of Advances in Modeling Earth Systems*, 15.

Kazil, J., Narenpitak, P., Yamaguchi, T., and Feingold, G. (2024). On climate change and trade cumulus organization. *Journal of Advances in Modeling Earth Systems*, 16.

Kazil, J., Yamaguchi, T., and Feingold, G. (2017). Mesoscale organization, entrainment, and the properties of a closed-cell stratocumulus cloud. *Journal of Advances in Modeling Earth Systems*, 9:2214–2229.

Kessler, E. (1969). *On the Distribution and Continuity of Water Substance in Atmospheric Circulations*. Meteorological Monographs. American Meteorological Society.

Khairoutdinov, M. and Kogan, Y. (2000). A new cloud physics parameterization in a large-eddy simulation model of marine stratocumulus. *Monthly Weather Review*, 128:229–243.

Khairoutdinov, M. F., Blossey, P. N., and Bretherton, C. S. (2002). Global system for atmospheric modeling: Model description and preliminary results. *Journal of Advances in Modeling Earth Systems*, 14.

Khairoutdinov, M. F. and Randall, D. A. (2003). Cloud resolving modeling fo the arm summer 1997 iop: Model formulation, results, uncertainties, and sensitivities. *Journal of the Atmospheric Sciences*, 60:607–625.

Kitchen, M. and Caughey, S. J. (1981). Tethered-balloon observations of the structure of small cumulus clouds. *Quarterly Journal of the Royal Meteorological Society*, 107:853–874.

Koren, I. and Feingold, G. (2011). Aerosol-cloud-precipitation system as a predator-prey problem. *Proceedings of the National Academy of Sciences*, 108:12227–12232.

Krueger, S. K., McLean, G. T., and Fu, Q. (1995). Numerical simulations of the stratus-to-cumulus transition in the subtropical marine boundary layer. part ii: Boundary-layer circulation. *Journal of the Atmospheric Sciences*, 52:2851–2868.

Kuettner, J. P. (1971). Cloud bands in the earth's atmosphere: Observations and theory. *Tellus*, 23:404–426.

Liu, J., Zhu, Y., Wang, M., Rosenfeld, D., and Cao, Y. (2022). Marine warm cloud fraction decreases monotonically with rain rate for fixed vertical and horizontal cloud sizes. *Geophysical Research Letters*, 50.

Locatelli, J. D. and Hobbs, P. V. (1974). Fall speeds and masses of solid precipitation particles. *Journal of Geophysical Research*, 79:2185–2197.

Lorenz, E. N. (1963). Deterministic nonperiodic flow. *Journal of the Atmospheric Sciences*, 20:130–141.

Lotka, A. J. (1910). Contribution to the theory of periodic reaction. *Journal of Physical Chemistry*, 14:271–274.

Lotka, A. J. (1925). *Elements of Physical Biology*. Williams & Wilkins Company.

Mascaut, F., Pujol, O., Brioude, J., Jensen, A., Lefranc, M., Evan, S., and Crumeyrolle, S. (2022). A competition-species model for water vapour-aerosol-cloud-rain interactions. *Atmospheric Research*, 284.

Mason, B. and Chien, C. (1962). Cloud-droplet growth by condensation in cumulus. *Quarterly Journal of the Royal Meteorological Society*, 88:136–142.

Narenpitak, P., Kazil, J., Yamaguchi, T., Quinn, P., and Feingold, G. (2021). From sugar to flowers: A transition of shallow cumulus organization during atomic. *Journal of Advances in Modeling Earth Systems*, 13.

NASA (2024). Nasa worldview.

Nicholls, S. (1989). The structure of radiatively driven convection in stratocumulus. *Quarterly Journal of the Royal Meteorological Society*, 115:487–511.

Pscheidt, I., Senf, F., Heinze, R., Deneke, H., and Tromel, S. (2019). How organized is deep convection over germany? *Quarterly Journal of the Royal Meteorological Society*, 145:2366–2384.

Pujol, O. and Jensen, A. (2019). Cloud-rain predator-prey interactions: Analyzing some properties of the koren-feingold model and introduction of a new species-competition bulk system with a hopf bifurcation. *Physica D*, 399:86–94.

Rasp, S., Schulz, H., Bony, S., and Stevens, B. (2020). Combining crowdsourcing and deep learning to explore the mesoscale organization of shallow convection. *Bulletin of the American Meteorological Society*, November 2020:1980–1995.

Rogers, R. R. and Yau, M. K. (1989). *A Short Course in Cloud Physics*. Butterworth-Heinemann, 3rd edition.

Rosemeier, J. and Spichtinger, P. (2020). Pattern formation in clouds via turing instabilities. *Mathematics of Climate and Weather Forecasting*, 6:75–96.

Saffin, L., Lock, A., Tomassini, L., Blyth, A., Boing, S., Denby, L., and Marsham, J. (2023). Kilometer-scale simulations of trade-wind cumulus capture processes of mesoscale organization. *Journal of Advances in Modeling Earth Systems*, 15.

Savazzi, A. C., Nuijens, L., de Rooy, W., Janssens, M., and Siebesma, A. P. (2024). Momentum transport in organized shallow cumulus convection. *Journal of the Atmospheric Sciences*, 81:279–296.

Savre, J. (2022). What controls local entrainment and detrainment rates in simulated shallow convection. *Journal of the Atmospheric Sciences*, 79:3065–3082.

Seifert, A. and Beheng, K. D. (2001). A double-moment parameterization for simulating autoconversion, accretion and selfcollection. *Atmospheric Research*, 59-60:265–281.

Seifert, A. and Heus, T. (2013). Large-eddy simulation of organized precipitating trade wind cumulus clouds. *Atmospheric Chemistry and Physica*, 13:5631–5645.

Seinfeld, J. H. and Pandis, S. N. (2016). *Atmospheric Chemistry and Physics: From Air Pollution to Climate Change*. John Wiley & Sons Inc., 3rd edition.

Smalley, K. M. and Rapp, A. D. (2020). The role of cloud size and environmental moisture in shallow cumulus precipitation. *Journal of Applied Meteorology and Climatology*, 59:535–550.

Spassova, T. and Nikolov, S. (2005). A hierarchy of nonlinear multiparametric models of cloud dynamics and microphysics. *Atmospheric Research*, 78:93–102.

Stephens, G. (1990). On the relationship between water vapor over the oceans and sea surface temperature. *Journal of Climate*, 3:634–645.

Stevens, B., Bony, S., Brogniez, H., Hentgen, L., Hohenegger, C., Kiemle, C., L'Ecuyer, T. S., Naumann, A. K., Schulz, H., Siebesma, P. A., Vial, J., Winker, D. M., and Zuidema, P. (2019). Sugar, gravel, fish and flowers: Mesoscale cloud patterns in the trade winds. *Quarterly Journal of the Royal Meteorological Society*, 146:141–152.

Strogatz, S. H. and Stewart, I. (1993). Coupled oscillators and biological synchronization. *Scientific American*, 269.

Stull, R. B. (1988). *An Introduction to Boundary Layer Meteorology*. Kluwer Academic Publishers.

Suzuki, K., Nakajima, T. Y., and Stephens, G. L. (2010). Particle growth and drop collection efficiency of warm clouds as inferred from joint cloudsat and modis observations. *Journal of the Atmospheric Sciences*, 67:3019–3032.

Suzuki, K., Stephens, G. L., van den Heever, S. C., and Nakajima, T. Y. (2011). Diagnosis of the warm rain process in cloud-resolving models using joint cloudsat and modis observations. *Journal of the Atmospheric Sciences*, 68:2655–2668.

Tao, W.-K. and Li, X. (2016). The relationship between latent heating, vertical velocity, and precipitation processes: The impact of aerosols on precipitation in organized deep convective systems. *Journal of Geophysical Research: Atmospheres*, 121:6299–6320.

Tompkins, A. M. and Semie, A. G. (2017). Organization of tropical convection in low vertical wind shears: Role of updraft entrainment. *Journal of Advances in Modeling Earth Systems*, 9:1046–1068.

Twomey, S. (1959). The nuclei of natural cloud formation part ii: The supersaturation in natural clouds and the variation of cloud droplet concentration. *Pure and Applied Geophysics*, 43:243–249.

Vogel, R., Albright, A. L., Vial, J., George, G., Stevens, B., and Bony, S. (2022). Strong cloud-circulation coupling explains weak trade cumulus feedback. *Nature*, 612:696–700.

Vogel, R. and Bony, S. (2020). Estimating the shallow convective mass flux from the subcloud-layer mass budget. *Journal of the Atmospheric Sciences*, 77:1559–1574.

Vogel, R., Konow, H., Schulz, H., and Zuidema, P. (2021). A climatology of trade-wind cumulus cold pools and their link to mesoscale cloud organization. *Atmospheric Chemistry and Physics*, 21:16609–16630.

Vogel, R., Nuijens, L., and Stevens, B. (2020). Influence of deepening and mesoscale organization of shallow convection on stratiform cloudiness in the downstream trades. *Quarterly Journal of the Royal Meteorological Society*, 146:174–185.

Wacker, U. (1992). Structural stability in cloud physics using parameterized microphysics. *Beitrage zur physik der atmosphaere*, 65:231–242.

Wacker, U. (1995). Competition of precipitation particles in a model with parameterized cloud physics. *Journal of the Atmospheric Sciences*, 52:2577–2589.

Wacker, U. and Herbert, F. (1998). On different moisture variables in the constitutive equation for condensation growth of cloud drops. *Geophysical Research Letters*, 25:4473–4476.

Wallace, J. M. and Hobbs, P. V. (2006). *Atmospheric Science: An Introductory Survey*. Elsevier.

Warner, J. (1955). The water content of cumuliform cloud. *Tellus*, 7:449–457.

Wood, R. and Bretherton, C. S. (2004). Boundary layer depth, entrainment, and decoupling in the cloud-capped subtropical and tropical mean boundary layer. *Journal of Climate*, 17:3576–3588.

Wood, R. and Bretherton, C. S. (2006). On the relationship between stratiform low cloud cover and lower-troposheric stability. *Journal of Climate*, 19:6425–6432.

Wood, R., Irons, S., and Jonas, P. (2002). How important is the spectral ripening effect in stratiform boundary layer clouds? studies using simple trajectory analysis. *Journal of the Atmospheric Sciences*, 59:2681–2693.

Wyant, M. C., Bretherton, C. S., Rand, H. A., and Stevens, D. E. (1997). Numerical simulations and a conceptual model of the stratocumulus to trade cumulus transition. *Journal of the Atmospheric Sciences*, 54:168–192.

Xue, H. and Feingold, G. (2006). Large-eddy simulations of trade wind cumuli: Investigation of aerosol indirect effects. *Journal of the Atmospheric Sciences*, 63:1605–1622.

Xue, Y. and Wang, L.-P. (2008). Growth of cloud droplets by turbulent collision-coalescence. *Journal of the Atmospheric Sciences*, 65:331–356.

Zuidema, P., Li, Z., Hill, R. J., Bariteau, L., Rilling, B., Fairall, C., Brewer, W. A., Albrecht, B., and Hare, J. (2012). On trade wind cumulus cold pools. *Journal of the Atmospheric Sciences*, 69:258–280.